

AD-A096 010

VIRGINIA POLYTECHNIC INST AND STATE UNIV BLACKSBURG --ETC F/G 11/2
THERMO-MECHANICAL AND THERMAL BEHAVIOR OF HIGH-TEMPERATURE STRU--ETC(U)
DEC 80 D P HASSELMAN

N00014-78-C-0431

NL

UNCLASSIFIED

1 of 3
AD-A096 010

2025

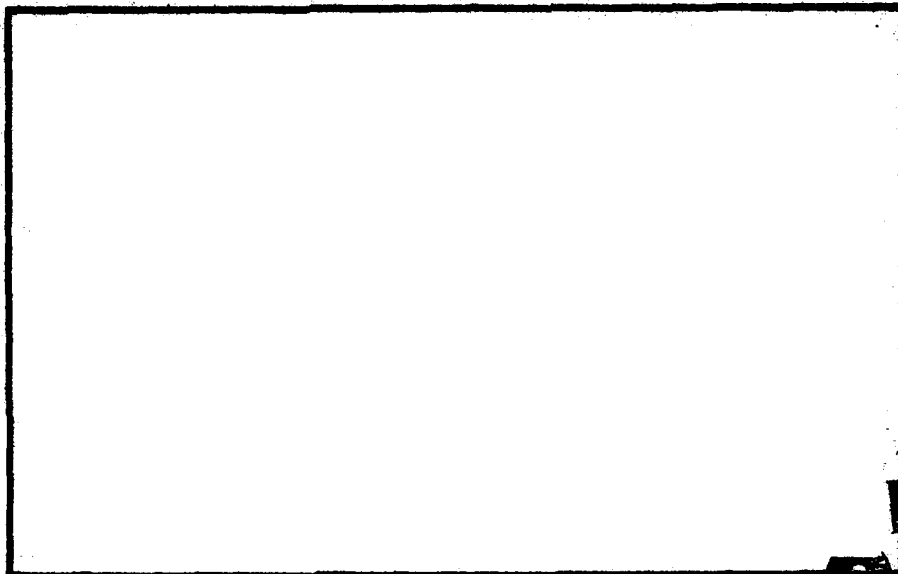
12 23

AD A 096010

LEVEL III

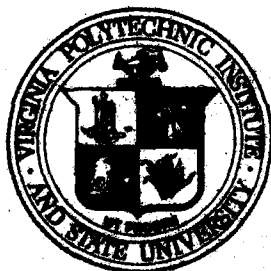
1081915

COLLEGE
ENGINEERING



DTIC
ELECTE
MAY 5 1961

VIRGINIA
POLYTECHNIC
INSTITUTE
AND
STATE
UNIVERSITY



DOC FILE COPY

X

81 1 23 056

BLACKSBURG
VIRGINIA

(12)

LEVEL II

THERMO-MECHANICAL AND THERMAL
BEHAVIOR OF HIGH-TEMPERATURE STRUCTURAL MATERIALS

Interim Report to
Office of Naval Research
Contract No.: N00014-78-C-0431
January 1, 1980 - December 31, 1980

by

D. P. H. Hasselman
Virginia Polytechnic Institute and State University
Blacksburg, Virginia 24061

and

L. D. Bentsen, N. Claussen, M. P. Kamat, K. Nihara
K. Satyamurthy, C. Shih, J. P. Singh, J. R. Thomas,
Y. Tree and G. Ziegler

DTIC
ELECTE
MAR 0 5 1981

E

Reproduction in whole or in part is permitted for any purpose
of the United States Government.

Unclassified

SECURITY CLASSIFICATION OF THIS PAGE (When Data Entered)

REPORT DOCUMENTATION PAGE		READ INSTRUCTIONS BEFORE COMPLETING FORM
1. REPORT NUMBER	2. GOVT ACCESSION NO.	3. RECIPIENT'S CATALOG NUMBER
	AD-A096	070
4. TITLE (and Subtitle)		5. TYPE OF REPORT & PERIOD COVERED
(6) Thermo-Mechanical and Thermal Behavior of High-Temperature Structural Materials.		Interim Report Jan. 1, 1980 - Dec. 31, 1980
7. AUTHOR(s)		6. PERFORMING ORG. REPORT NUMBER
(10) D. P. H. Hasselman		
9. PERFORMING ORGANIZATION NAME AND ADDRESS		8. CONTRACT OR GRANT NUMBER(s)
Virginia Polytechnic Institute and State University, Blacksburg, VA 24061		(15) N00014-78-C-04317
11. CONTROLLING OFFICE NAME AND ADDRESS		10. PROGRAM ELEMENT, PROJECT, TASK AREA & WORK UNIT NUMBERS
Office of Naval Research, Code 471 Arlington, VA 22217 (12) 209		(11) 31 Dec 80
14. MONITORING AGENCY NAME & ADDRESS (if different from Controlling Office)		12. REPORT DATE
(9) Interim Rept. 1 Jan-31 Dec 80		December 31, 1980
		13. NUMBER OF PAGES
		210
		15. SECURITY CLASS. (of this report)
		Unclassified
		15a. DECLASSIFICATION/DOWNGRADING SCHEDULE
16. DISTRIBUTION STATEMENT (of this Report)		
See Distribution Label. Do not release to NTIS		
17. DISTRIBUTION STATEMENT (of the abstract entered in Block 20, if different from Report)		
18. SUPPLEMENTARY NOTES		
19. KEY WORDS (Continue on reverse side if necessary and identify by block number)		
Absorption coefficient, composites (MgO-SiC, Al ₂ O ₃ -ZrO ₂ , Si ₃ N ₄ -ZrO ₂), alumina, crack propagation and interaction, fracture, glass, micro-cracking, quench testing, silicon nitride, thermal conductivity and thermal diffusivity, thermal radiation, thermal stress, thermal shock, toughening, zirconia.		
20. ABSTRACT (Continue on reverse side if necessary and identify by block number)		
This report contains studies, completed over the period from 1/1/80 to 12/31/80 as part of a research program on the thermo-mechanical and thermal behavior of high-temperature structural materials, in the form of individual chapters as follows: — 2nd page		

DD FORM 1473

JAN 73

EDITION OF 1 NOV 65 IS OBSOLETE

Unclassified

SECURITY CLASSIFICATION OF THIS PAGE (When Data Entered)

406822

2017

- ## Reviews and Books

- 14135

[illegible]

THERMO-MECHANICAL AND THERMAL
BEHAVIOR OF HIGH-TEMPERATURE STRUCTURAL MATERIALS

PREFACE

Technical ceramics because of their chemical inertness, high melting point, good wear resistance, excellent mechanical stability at high temperature and other unique properties, represent a class of materials eminently suited for many critical engineering applications. Unfortunately, because of their brittleness and unfavorable combination of pertinent material properties, technical ceramics generally are highly susceptible to catastrophic failure in non-uniform thermal environments, which give rise to thermal stresses of high magnitude.

Thermal stress failure analysis of structural materials represents a multi-disciplinary problem which involves the principles of heat transfer, mechanics and materials engineering. Over the last few decades much general understanding of the nature of thermal stress failure of brittle materials has been generated. However, due to the multi-disciplinary nature of the problem, the ability to predict thermal stress failure quantitatively for design or other purposes has lagged behind the progress made in other engineering fields. The objective of the present program is to improve the qualitative and quantitative understanding of the nature of thermal stress failure of brittle structural materials, including the experimental as well as theoretical variables. In order to achieve this objective, the participating investigators and scope of the program are organized such that full advantage is taken of the combined inputs from a number of engineering disciplines. In a similar spirit a number of studies were conducted in cooperation with investigators at other institutions.

The effort of this program consists of four main themes, including: experimental thermal shock testing, measurement of thermophysical properties relevant to thermal stress failure, the analysis of thermal stress failure and the dissemination of information on thermal stresses in the form of review articles, conferences, etc.

Studies completed within the period covered by this report are presented as individual chapters in the main body of this report. The title of these chapters within their main theme together with a brief comment are as follows:

A. Experimental Thermal Shock Testing

Chapter I: "Effect of Bath and Specimen Temperature on the Thermal Stress Resistance of Brittle Ceramics Subjected to Thermal Quenching"

This study shows that the heat transfer coefficient of fluid quenching media can be highly variable. Such variability must be taken into account in the quantitative interpretation of experimental data for the relative thermal stress resistance of different materials.

Chapter II: "Improvement of Thermal Shock Resistance of Brittle Structural Ceramics by a Dispersed Phase of Zirconia"

This study shows that the thermal shock behavior of structural ceramics such as alumina and silicon nitride can be improved significantly as the result of toughening by the zirconia dispersed phase.

B. Measurement of Thermophysical Properties Relevant to Thermal Stress Failure

Chapter III: "Effect of Phase Composition and Microstructure on the Thermal Diffusivity of Silicon Nitride"

The results of this study indicate that the heat transfer properties of hot-pressed and reaction-sintered silicon nitride are strongly affected by the $\alpha/\alpha+\beta$ ratio, grain boundary phase, structure and size of pore as well as grain morphology.

Chapter IV: "Orientation Effects on the Thermal Diffusivity of Hot-Pressed Silicon Nitride"

The thermal diffusivity of silicon nitride was found to be greater in perpendicular than parallel to the hot-pressing direction. This effect results from the preferred crystallographic orientation of the β - Si_3N_4 grains.

Chapter V: "Observations on the Sub-Critical Growth and Healing of Microcracks in Brittle Ceramics"

The stability of microcracks in brittle structural materials was monitored by measurements of the thermal diffusivity. The experimental observations of crack-growth and healing provided evidence that the microcrack configurations depend strongly on temperature levels as well as time.

C. Analysis of Thermal Stresses

Chapter VI: "Thermal Stresses in Partially Absorbing Flat Plate Symmetrically Heated by Thermal Radiation and Cooled by Convection"

Chapter VII: "Analysis of Thermal Stress Resistance of Partially Absorbing Ceramic Plate Subjected to Asymmetric Radiation, II, Convective Cooling at Front Surface"

The above two studies are in the general area of thermal stresses generated by a spatially non-uniform internal heat generation, relevant to IR-windows, solar energy collectors and nuclear fusion reactors. The results of these studies establish the role of the material properties and heat transfer variables which affect thermal stress resistance under the particular heating and cooling conditions considered.

Chapter VIII: "Effect of Nature of Concavity of Temperature Distribution on Position and Sign of Maximum Thermal Stress"

In a previously reported study of the thermal stresses in a semi-absorbing ceramic plate, heated at the front by radiation and cooled at the back by convection, it was found that the maximum tensile stresses occurred in the front surface, which is at the highest temperature. This finding contrasts with the usual result found for many other instances of thermal stresses, in which generally, the regions at highest temperature are in a state of compression. As demonstrated in this chapter, the occurrence of the maximum tensile stresses in the hottest region of the plate is due to the concave downward nature of the curvature of the temperature distribution within the plate due to the internal heat generation. In the case of heat transfer at the surface as is generally the case in the vast majority of instances of transient heat transfer, the temperature distribution is concave upward, which results in a compressive stress state at the position of highest temperature.

D. Dissemination of Information on Thermal Stresses

Chapter IX: "Effect of Crack Interaction on the Fracture Initiation and Crack Propagation in Brittle Ceramics Subjected to Severe Thermal Shock"

It is shown that the interaction between cracks generally is beneficial to thermal stress resistance, with the exception of co-planar cracks which can coalesce to result in complete structural disintegration.

Chapter X: "Stresses Due to Thermal Trapping in Semi-Absorbing Materials Subjected to Intense Radiation"

This study reviews the principal theoretical results of the thermal stresses in semi-absorbing ceramics subjected to thermal radiation.

Chapter XI: "Effect of Spatial Variation of Thermal Conductivity on Magnitude of Tensile Thermal Stresses in Brittle Materials Subjected to Convective Heating"

This article reviews the results reported previously, which shows that a spatial variation of thermal conductivity can significantly lower the magnitude of the tensile thermal stresses in convective heating.

Within the general theme of the dissemination of information on thermal stresses, a conference was organized on the topic, "Thermal Stresses in Materials and Structures in Severe Thermal Environments," held at Virginia Polytechnic Institute and State University, March 19-21, 1980. The proceedings of this conference which contain a total of forty-three papers on thermal stresses in materials and structures are available from Plenum Press.

For the convenience of the reader, Table 1 lists the status of publications presented in earlier reports. For most of these studies, reprints are available and will be sent on request.

Table 1. Publication Status of Technical Reports Prepared during Previous Reporting Periods (4/1/78 - 12/15/79)

1. D. P. H. Hasselman and W. A. Zdaniewski, "Thermal Stress Resistance Parameters of Brittle Materials Subjected to Thermal Stress Fatigue," J. Am. Ceram. Soc., 61 (7-8) 375 (1978).
2. D. P. H. Hasselman, "Effect of Cracks on Thermal Conductivity," J. Comp. Mat., 12, 403-07 (1978).
3. W. Zdaniewski, H. Knoch, J. Heinrich and D. P. H. Hasselman, "Thermal Diffusivity of Reaction-Sintered Silicon Nitride," Ceram. Bull., 58, 539 (1979).
4. D. P. H. Hasselman, "Figures-of-Merit for the Thermal Stress Resistance of High-Temperature Brittle Materials," Ceramurgia International, 4, 147 (1979).
5. K. Chyung, G. E. Youngblood and D. P. H. Hasselman, "Effect of Crystallization on the Thermal Diffusivity of a Cordierite Glass-Ceramic," J. Amer. Ceram. Soc., 61, 530 (1978).
6. D. P. H. Hasselman, "Role of Physical Properties in the Resistance of Brittle Ceramics to Fracture in Thermal Buckling," J. Am. Ceram. Soc., 62, 125 (1979).
7. D. P. H. Hasselman and J. P. Singh, "Analysis of Thermal Stress Resistance of Micro-cracked Brittle Materials," Ceramic Bull. 58, 856 (1979).
8. G. E. Youngblood, L. Bentsen, J. W. McCauley and D. P. H. Hasselman, "Thermal Diffusivity of Ba-Mica/Alumina Composites," J. Amer. Ceram. Soc., 58, 620 (1979).
9. D. P. H. Hasselman and Y. Tree, "On the Thermal Fracture of Ice," J. Mat. Sc., 14, 1499 (1979).
10. D. P. H. Hasselman, J. C. Swearingen, E. K. Beauchamp and W. A. Zdaniewski, "Effect of Alumina Dispersions on the Thermal Conductivity/Diffusivity and Thermal Stress Resistance of a Borosilicate Glass," J. Mat. Sc., 15, 518-20 (1980).
11. D. P. H. Hasselman, J. R. Thomas, Jr., M. P. Kamat and K. Satyamurthy, "Thermal Stress Analysis of Partially Absorbing Brittle Ceramics Subjected to Radiation Heating," J. Am. Ceram. Soc., 63, 21-25 (1980).
12. J. P. Singh, J. R. Thomas, Jr., and D. P. H. Hasselman, "Analysis of Effect of Heat Transfer Variables on Thermal Stress Resistance of Brittle Ceramics Measured by Quenching Experiments," J. Am. Ceram. Soc., 63, 140-44 (1980).

Table 1 (Cont'd)

13. K. Satyamurthy, M. P. Kamat, J. P. Singh and D. P. H. Hasselman, "Effect of Spatially Varying Thermal Conductivity on Magnitude of Thermal Stress in Brittle Ceramics Subjected to Convective Heating," J. Am. Ceram. Soc., 63, 363 (1980).
14. G. Ziegler and D. P. H. Hasselman, "Effect of Data Scatter on Apparent Thermal Stress Failure Mode of Brittle Ceramics," Ceramurgia, 5, 126 (1979).
15. K. Satyamurthy, J. P. Singh, M. P. Kamat and D. P. H. Hasselman, "Effect of Spatially Varying Porosity on Magnitude of Thermal Stress During Steady-State Heat Flow," J. Amer. Ceram. Soc., 62, 432 (1979).
16. Bob R. Powell, Jr., G. E. Youngblood, D. P. H. Hasselman and Larry D. Bentsen, "Effect of Thermal Expansion Mismatch on the Thermal Diffusivity of Glass-Ni Composites," J. Amer. Ceram. Soc., (in press).
17. D. P. H. Hasselman, P. F. Becher and K. S. Mazdidasni, "Analysis of the Resistance of High-E, Low-E Brittle Composites to Failure by Thermal Shock," Materials Technology, 11, 82 (1980).
18. K. Satyamurthy, J. P. Singh, M. P. Kamat and D. P. H. Hasselman, "Thermal Stress Analysis of Brittle Ceramics with Density Gradients Under Conditions of Transient Convective Heat Transfer," Proc. Brit. Ceram. Soc., 80, 10 (1980).
19. J. R. Thomas, Jr., J. P. Singh and D. P. H. Hasselman, "Analysis of Thermal Stress Resistance of Partially Absorbing Ceramic Plate Subjected to Asymmetric Radiation, I: Convective Cooling at Rear Surface," J. Am. Ceram. Soc., (in press).
20. D. P. H. Hasselman, "Effect of Micro-Cracking on Thermal Conductivity: Analysis and Experiment," Proc. 16th Int. Conf. Thermal Conductivity (in press).
21. J. R. Thomas, J. P. Singh and D. P. H. Hasselman, "Role of Thermal Expansion in the Thermal Stress Resistance of Semi-Absorbing Brittle Materials Subjected to Severe Thermal Radiation," Proc. 7th Int. Thermal Expansion Symposium (in press).
22. J. P. Singh, D. P. H. Hasselman, W. M. Su, J. A. Rubin and R. Palicka, "Observations on the Nature of Micro-Cracking in Brittle Composites," J. Mat. Sc. (in press).

CHAPTER I

EFFECT OF BATH AND SPECIMEN TEMPERATURE
ON THE THERMAL STRESS RESISTANCE OF BRITTLE
CERAMICS SUBJECTED TO THERMAL QUENCHING

by

J. P. Singh, Y. Tree and D. P. H. Hasselman

Department of Materials Engineering
Virginia Polytechnic Institute and State University
Blacksburg, VA 24061 USA

ABSTRACT

The effect of specimen and bath temperature on the failure of brittle ceramics in a thermal quench experiment was studied by quenching glass and alumina rods in water and silicone oil baths at different temperatures. The results were discussed in terms of the variation of heat transfer coefficient of the quenching media and the change in material properties as a function of temperature. It was found that the usual assumption of constant heat transfer coefficient and material properties may lead to considerable errors in the quantitative interpretation of the results of thermal quench experiments. Effective values for the film coefficient of heat transfer for water and oil baths were estimated as a function of film temperature from thermal quench data. Recommendations were made for the selection of quenching media and for the procedure to be followed in reporting the results.

1. INTRODUCTION

Because of their favorable properties at high temperature as well as corrosive and erosive environments, ceramic materials are finding ever wider applications in industrial and many other fields. Because of their inherent brittleness and combination of other pertinent properties, ceramic materials, however, exhibit poor resistance to catastrophic failure under thermal conditions which generate thermal stresses. Therefore, for the purpose of reliable engineering design, it is important that the variables which control thermal stress failure of brittle ceramics are well understood. For a given thermal environment, the selection of materials with optimum thermal stress resistance can be based on "thermal stress resistance parameters" obtained from theory¹⁻⁶ or on comparative testing.

One such method of testing thermal stress resistance of ceramic materials consists of quenching appropriate specimens from high temperature into a fluid medium at lower temperature.⁷⁻⁹ Typical specimens are rods with circular or square cross-section. Quenching media can include water, oils or fluidized beds. Although, this test method enjoys considerable popularity because of its relative simplicity, the experimental results obtained frequently do not agree well with predictions based on theory.⁸⁻¹⁰ In part, such discrepancies possibly can be attributed to differences in the susceptibility of ceramic materials to subcritical crack growth which was shown to be significant in the water quenching of a glass.¹¹

Other possible variables to which a discrepancy between theory and experiment can be attributed, can be ascertained by the theoretical expression for the critical temperature difference (ΔT_c) required to

induce thermal stress failure in a ceramic specimen subjected to a thermal quench:

$$\Delta T_c = A S_t(1-\nu)/\alpha E + B S_t(1-\nu)K/\alpha Eah \quad (1)$$

where A and B are constants which depend on the geometry of the specimen, a is the characteristic dimension (i.e., radius of a circular cylinder), S_t is the tensile strength, E is Young's modulus, ν is Poisson's ratio, α is the coefficient of thermal expansion, K is the thermal conductivity and h is the heat transfer coefficient.

Eq. 1 indicates that ΔT_c depends on a number of material properties, the dimensions of the specimen and the heat transfer coefficient, h. The properties such as the coefficient of thermal expansion, Young's modulus, Poisson's ratio and thermal conductivity as well as their temperature dependence are readily measured. An assessment of the tensile strength is more difficult due to the statistical nature of brittle fracture. This latter phenomenon requires the need of establishing fracture probabilities based on stress distributions, specimen dimensions, etc., by such theories advanced by Weibull¹² or others. The need for such an approach was established in a previous study¹³ of the thermal fatigue of a glass. The constants A and B are readily determined by analytical or numerical methods.¹⁴⁻¹⁶ Specimen dimensions can be obtained to high precision. This leaves the heat transfer coefficient as the last remaining significant variable, which could be responsible for the discrepancy between theory and experiment. Generally, in the comparison and interpretation of quenching data, the heat transfer characteristics of the fluid medium are assumed to be invariant.

To establish the validity of this latter assumption, it should be noted that the transfer of heat between a solid and fluid is governed by a number of variables. Firstly, the heat transfer coefficient depends on the fluid properties such as the coefficient of volume thermal expansion, the density, the specific heat, the thermal conductivity as well as the viscosity. For purposes of the objectives of this study, it is important to note that these fluid properties especially the viscosity can show a strong temperature dependence. Secondly, the rate of heat transfer depends on the geometry and dimensions of the solid and the difference in temperature between the solid surface and fluid.¹⁷ Thirdly, for a specimen falling through the fluid at its terminal velocity,^{*} the rate of heat transfer also is a function of the relative difference in density of the fluid and solid.⁵ For a water bath¹⁷, the heat transfer is also affected very strongly by the effect of nucleate boiling which enhances the heat transfer coefficient and the effect of film formation at very high temperature levels which tends to suppress the transfer of heat.

Calculations of heat transfer coefficients generally are based on the properties of the fluid corresponding to the "film" temperature taken as the average of the temperature of the fluid and the surface of the solid. It should be noted then that ceramic specimens with differences in values of the critical quenching temperature (ΔT_c) will show differences

* Terminal velocity is the constant velocity attained by the specimen during its fall through the fluid bath when the downward force of its weight is balanced by the upward buoyancy and shear forces.

in the film temperature even for identical bath temperatures. In view of the temperature dependence of the fluid properties, especially the viscosity, differences in values of ΔT_c will lead to differences in the values of the heat transfer coefficient. At least in part, then, the aforementioned discrepancies between predicted and measured thermal stress resistance in quenching experiments, is because the heat transfer coefficient is a function of temperature rather than a constant as usually assumed.

The validity of this hypothesis can be verified by measuring ΔT_c for a range of film temperatures which can be achieved by varying the bath temperature. For a given material and bath temperature, the film temperature can be varied by changing the size of the specimen. The purpose of the present paper is to report the results of such a study.

2. EXPERIMENTAL

2.1. Materials and Quenching Media

Specimens consisted of circular rods 6.25 cm long and diam. of 0.53 cm of a soda-lime-silica glass** also used in previous studies^{11,13} and a polycrystalline aluminum oxide*** with a range of diameters. The values for the material properties of the glass are presented in Table 1. Similarly Table 2 lists the flexural strength of the aluminum oxide as a function of diameter size and other relevant properties.

The quenching media consisted of water and two silicone oils[†] with nominal viscosities of 5 and 100 centistokes at 25°C. The alumina specimens were tested in both the water and silicone oils. The glass rods were tested in the silicone oils only, in view of the considerable stress corrosion

** R-6, Owens Corning Fiberglass Corp., Toledo, Ohio

*** 998 Alumina, McDanel Refractory Porcelain Co., Beaver Falls, PA.

† Type 200, Dow-Corning Corp., Midland, Michigan.

TABLE 1. PROPERTIES OF $\text{Na}_2\text{O}-\text{CaO}-\text{SiO}_2$ GLASS¹¹

Flexural Strength at Liquid Nitrogen Temperature (MPa)	194
Young's Modulus of Elasticity (GPa)	69
Coefficient of Thermal Expansion ($^{\circ}\text{C}^{-1}$)	9.3×10^{-6}
Poisson's Ratio	0.25
Thermal Conductivity ($\text{Cal.cm}^{-1}\text{C}^{-1}\text{.S}^{-1}$)	2.5×10^{-3}

TABLE 2. PROPERTIES OF POLYCRYSTALLINE ALUMINA^{††}

Flexural Strength (MPa) Diam (cm)		Strength Relative to Diameter of 0.318 cm
0.318	327 (± 25)	1.0
0.475	311 (± 64)	0.95
0.635	271 (± 51)	0.83
0.953	251 (± 20)	0.77
Young's modulus of elasticity (GPa)		393
Coefficient of Thermal expansion ($^{\circ}\text{C}^{-1}$)		7.4×10^{-6}
Poisson's Ratio		0.265
Thermal Conductivity ($\text{Cal.cm.}^{-1}\text{C.}^{-1}\text{S.}^{-1}$)		
200 $^{\circ}\text{C}$		0.0437
300 $^{\circ}\text{C}$		0.0312
350 $^{\circ}\text{C}$		0.0291

^{††} The data on flexural strength and the thermal conductivity were obtained in our laboratory and the other material properties were supplied by the manufacturer.

effects encountered in water.^{11,13}

2.2 Quenching Procedure

The quenching media were contained in a stainless steel beaker with diameter of 18 cm by 20 cm deep. The steel beaker was held in a thermostatically controlled glass tank 30 cm in diam. by 30 cm deep. Prior to quenching, the ends of the glass rods were wrapped with glass insulating tape to prevent fracture due to unknown stresses at the rod ends. Because of the very high density of cracks in the alumina, this procedure was not required for these specimens.

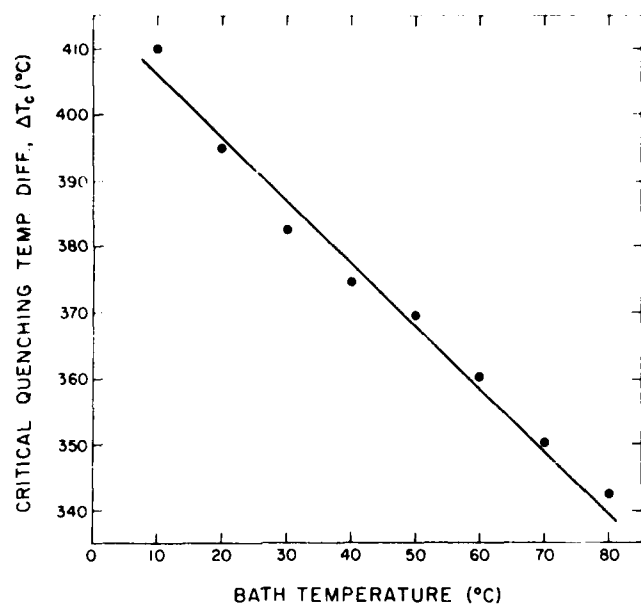
Sets of five specimens were heated slowly to a pre-selected temperature in a small electrically heated laboratory furnace and held for 10-15 minutes to assure thermal equilibrium, after which they were dropped into the quenching bath. This procedure was repeated for a range of quenching temperature difference (ΔT), defined as the difference in initial temperature of the specimen and the bath temperature. For the glass, the critical quenching temperature difference (ΔT_c) was defined as the value of ΔT at which three or more specimens had visible cracks. For the alumina specimens in which the cracks were not easily detectable, the critical temperature difference was obtained by measurements of the strength in 4-point bending with loading and support spans of 1.6 and 5 cm, respectively, and a crosshead speed of $0.05 \text{ cm. min}^{-1}$. Prior to the strength test, all specimens quenched in water were dried at $\sim 110^\circ\text{C}$ for 2-3 hours. The critical temperature difference was reported in terms of a temperature range. The lower limit of this range corresponded to the value of ΔT at which one specimen in five exhibited a significant strength loss. The upper limit corresponded to the value of ΔT at which four or more specimens exhibited a strength loss.

3. RESULTS AND DISCUSSION

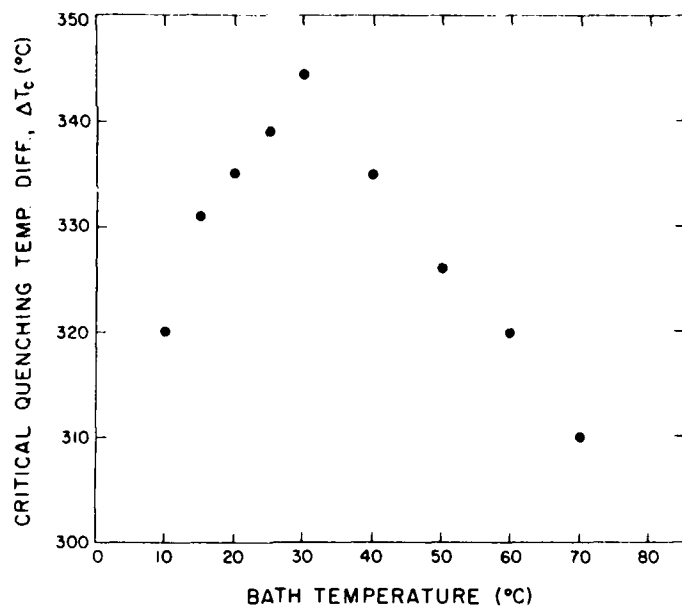
Figs. 1a and 1b show the value of ΔT_c as a function of bath temperature for the glass specimens quenched into the silicone oils with viscosity of 100 and 5 cst, respectively (at 25°C).

The decrease in ΔT_c with increasing bath temperature for the oil with viscosity of 100 cst above 30°C is thought to be due primarily to the decrease in viscosity with increasing temperature. Such a decrease in viscosity increases the heat transfer coefficient which in turn decreases ΔT_c . On comparison of figs. 1a and 1b, this conclusion is supported by the fact that for a given bath temperature the oil with the higher viscosity also yields the higher value of ΔT_c . At least for the 100 cst oil, the variation of ΔT_c with temperature cannot be attributed to the temperature dependence of the relevant material properties of the glass, since the initial specimen temperature (i.e., bath temperature + ΔT_c) is constant over the total range of bath temperature.

Of interest in fig. 1b is the decrease in ΔT_c with decreasing bath temperature below 30°C. This behavior is directly opposite to the effect noted for temperatures in excess of 30°C. It is thought that this apparent anomaly can be attributed to at least two effects. Firstly, a calculation of the heat transfer coefficient from the fluid properties near room temperature indicates that the temperature dependence of the heat transfer coefficient decreases with decreasing fluid temperature. For this reason, the effect of bath temperature on ΔT_c is expected to be less pronounced at the lower than at the higher bath temperatures. Secondly, it should be noted that with decreasing bath temperature the initial specimen temperature also decreases. This implies that the temperature



(a)



(b)

Fig. 1. Effect of bath temperature on ΔT_c for glass rods quenched in silicone oil:
(a) 100 centistokes (b) 5 centistokes.

dependence of the properties of the glass should be taken into account. In this respect, the rather high temperature dependence¹⁸ of Young's modulus and strength of a soda-lime-silica glass over this range of initial specimen temperature, tends to reduce ΔT_c with decreasing bath temperature. For a range of bath temperature of 10 to 30°C, the strength increases due to increasing initial specimen temperature prior to quenching beyond which the strength remains constant due to approximately constant initial specimen temperature. The anomaly in ΔT_c for the low bath temperature shown in fig. 1b, results from the combined effects of the temperature dependence of the heat transfer coefficient, Young's modulus and failure stress, with the temperature dependence of these latter two properties, contributing the major effect. In view of the relatively low temperature dependence of the coefficient of thermal expansion and the thermal conductivity, these two properties are thought to have little influence on the anomaly.

Support for this latter conclusion is given by the experimental data shown in fig. 2 for ΔT_c for the alumina rods with diam. of 0.63 cm quenched in the same silicon oil (5 cts) as the glass data shown in fig. 1b. For these alumina specimens the anomaly at the low value of bath temperature is absent. The value of ΔT_c decreases monotonically with increasing bath temperature probably due primarily to the decrease in viscosity and corresponding increase in heat transfer coefficient with increasing bath temperature. At the initial specimen temperature of 450°C the aluminum oxide is not expected to exhibit a significant change in fracture stress during the 15 min. anneal. This suggests that indeed the anomaly shown in fig. 1b is due to the temperature dependence of the strength and Young's modulus of the glass over the range of initial

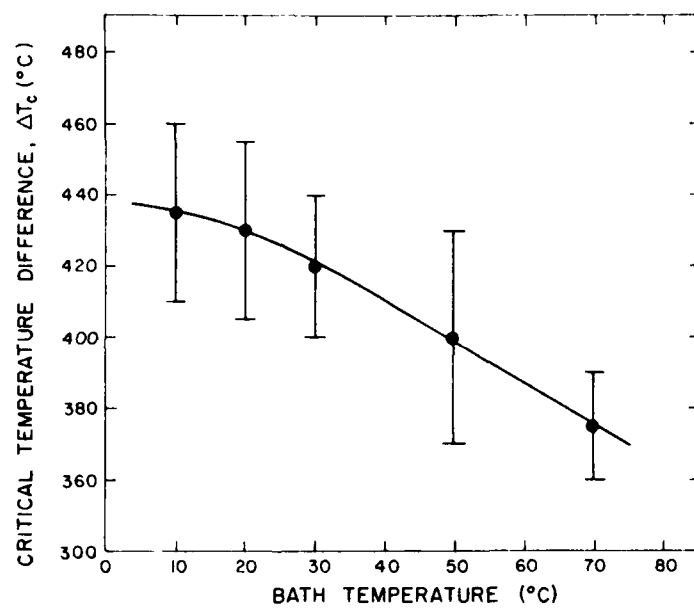


Fig. 2. Effect of bath temperature on ΔT_c for alumina rods ($d = 0.63$ cm.) quenched in silicone oil (5 centistokes).

specimen temperatures involved.

Figure 3 shows the effective heat transfer coefficient for the two silicone oils as a function of the film temperature calculated by means of eq. 1 from the experimental data for ΔT_c and the relevant material properties. In these calculations the strength at liquid nitrogen temperature (-196°C) was taken to be 194 MPa as measured by Badalian et al.¹¹ and its temperature dependence was assumed to be similar to that in reference 18. The strong temperature dependence is evident. Clearly these data are relevant only to the present quenching experiments and probably are not appropriate to other heat transfer conditions. Nevertheless, they may serve as a guide for the design of quenching experiments of other materials.

For water as the quenching medium, the experimental data for ΔT_c differed significantly from those obtained for silicone oil. Figure 4 shows the dependence of ΔT_c on the water bath temperature for the alumina rods with diameter of 0.318 cm. In contrast to the data obtained for the silicone oil, ΔT_c for the water bath shows an upward curvature with a minimum near 60°C . At the water temperature of 90°C , only a small fraction of the specimens could be fractured by the thermal stress generated at quenching temperature differences from 225 to 425°C . Figure 5 shows the distribution of the percentage of specimens fractured during the quench as a function of ΔT . No specimens could be fractured for values of $\Delta T > 425^\circ\text{C}$. For these reasons, for the bath temperature of 90°C , a value for ΔT_c could not be defined. Comparison of the data in Figs. 2 and 4 indicates that ΔT_c for the silicone oil exceeds ΔT_c for the water bath, due to large differences in heat transfer coefficients as will be shown later.

Figure 6a shows the size dependence of ΔT_c for the alumina specimens

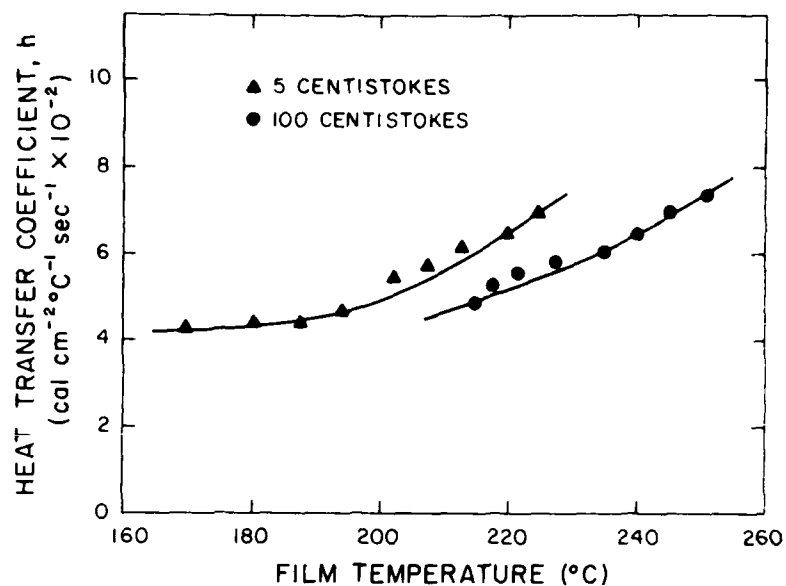


Fig. 3. Effective heat transfer coefficient for silicone oil baths inferred from the thermal fracture data of figures 1a and 1b.

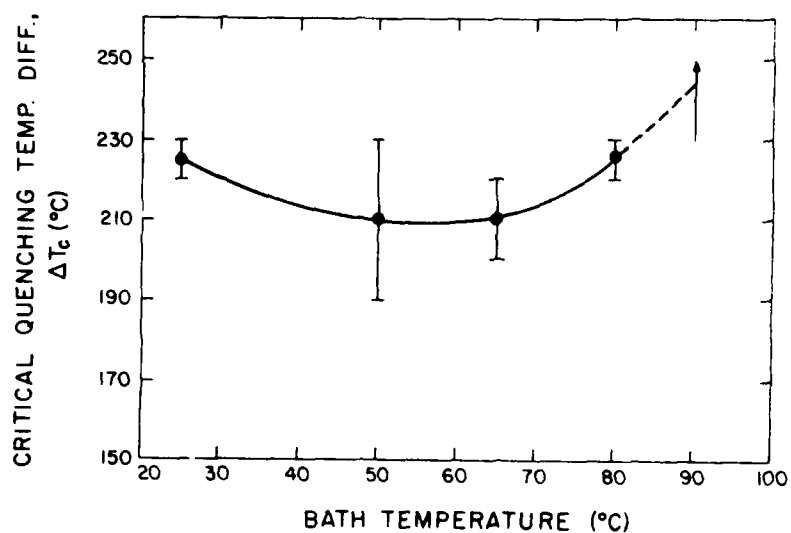


Fig. 4. Effect of bath temperature on ΔT_c for alumina rods ($d = 0.318$ cm.) quenched in water.

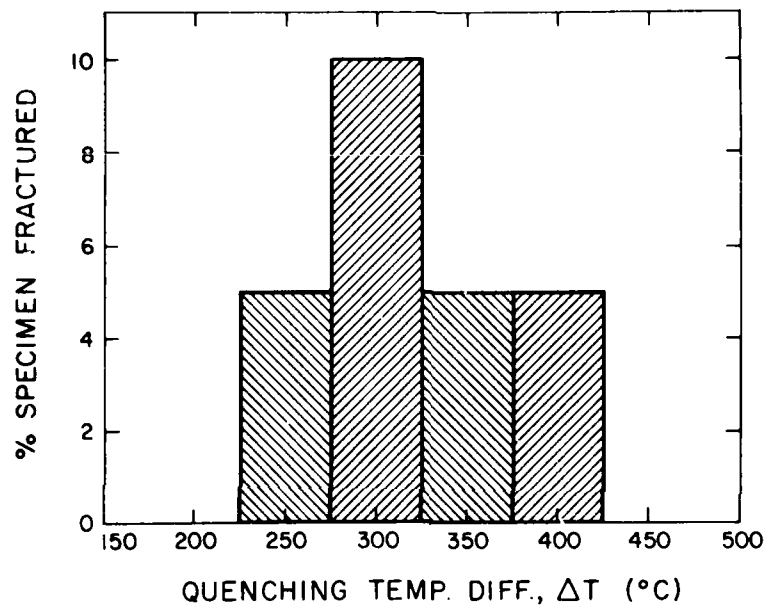


Fig. 5. Probability of failure of alumina rods ($d = 0.318$ cm.) quenched in water at 90°C .

quenched into the water bath at 25 and 90°C. For purpose of interpretation of the data, it is convenient to eliminate the effect of rod diameter on the flexural strength. This was accomplished as shown in fig. 6b by dividing the observed values of ΔT_c by the ratio of the flexural strength relative to the strength for the rod diameter of 0.318 cm, listed in Table 2. For this reason, ΔT_c in fig. 6b is referred to as "normalized" critical quenching temperature difference, $\Delta T_c'$. Of interest to note is that $\Delta T_c'$ decreases with increasing value of $1/d$, in contrast to an increase predicted by eq. 1. Since the derivation of eq. 1 was based on theory, this discrepancy cannot be attributed to a lack of fundamental understanding of thermo-mechanical principles.

At least a qualitative explanation for the data shown in figs. 4 and 6a can be based on the general temperature dependence of the heat transfer coefficient for a hot surface in water. This is shown schematically in fig. 7 as a function of the difference in temperature of the hot surface and the water temperature. At low temperature differences, the heat transfer coefficient increases with increasing temperature as the direct result of the nature of convective heat transfer coupled with nucleate boiling.¹⁷ At the higher temperature differences, the rate of heat transfer is limited by the formation of steam-film on the hot surface. Because of the existence of such a film, the value of the heat transfer coefficient will go through a maximum to be followed by a decrease with further increases in temperature difference. At sufficiently high temperatures where radiation from the hot surface becomes significant, an increase in "effective" heat transfer coefficient can be ob-

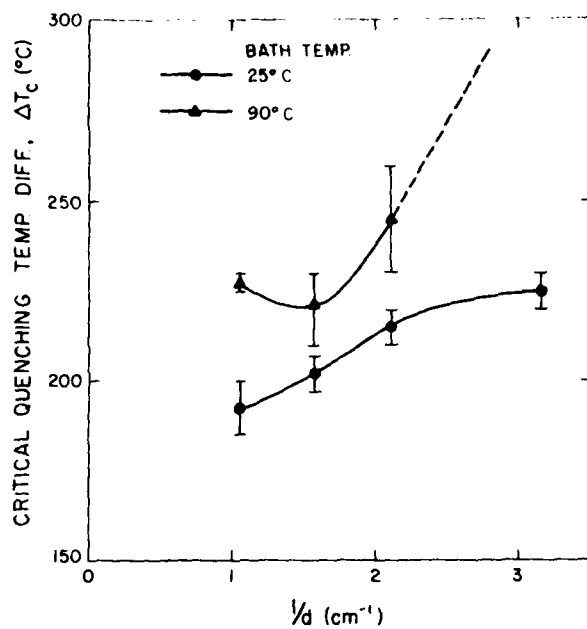


Fig. 6a. Effect of specimen size on ΔT_c for alumina rods quenched in water at 25 and 90°C.

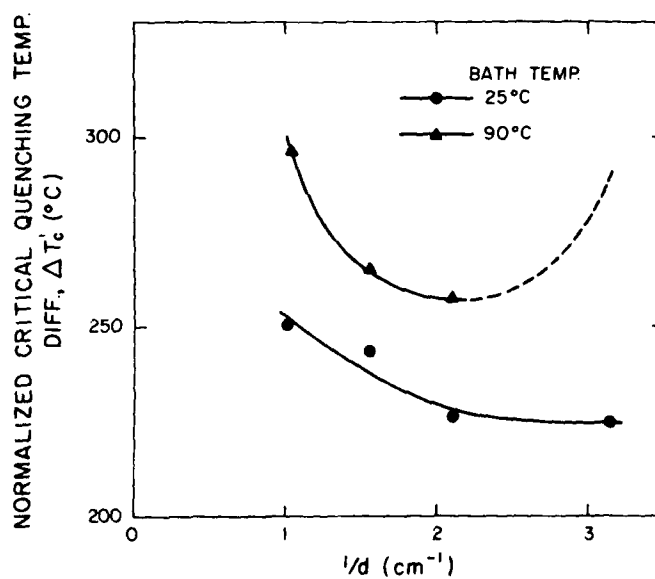


Fig. 6b. Normalized $\Delta T_c'$ for alumina rods quenched in water at 25 and 90°C.

served. Increases in water bath temperature towards the boiling for a given hot surface temperature will enhance the formation of the steam film accompanied by a corresponding decrease in heat transfer coefficient.

Examination of fig. 4 in view of the results of fig. 7 suggests that the minimum in the curve for ΔT_c vs water-bath temperature corresponds to the maximum in the curve of heat transfer coefficient as a function temperature difference. The data in fig. 6a for 25°C can be explained in terms of the rapid rise in heat transfer coefficient with temperature difference in the range of nucleate boiling. An increase in ΔT_c automatically increases the heat transfer coefficient which in turn limits the increase in ΔT_c which can be achieved. In fact, the plot in fig. 6b suggests that the relative rate of increase in heat transfer coefficient exceeds the rate at which ΔT_c should increase with decreasing specimen size. In spite of these effects, ΔT_c increases with decreasing specimen size because of the corresponding increase in strength with decreasing specimen size. A similar explanation can be given for the data for the bath temperature of 90°C, if it is assumed that the heat transfer coefficient corresponds to the low values near the minimum between the regions of steam-film formation and radiation indicated in fig. 7.

Support for the above explanations is found in the form of the "effective" heat transfer coefficient for the water bath calculated from the observed values of ΔT_c (figs. 4 and 6a) with exception of those for 90°C for the 0.318 cm diam. rods, and the property data for the alumina given in Table 2. These calculated values are shown in fig. 8 as a function of film temperature defined earlier. These calculated data

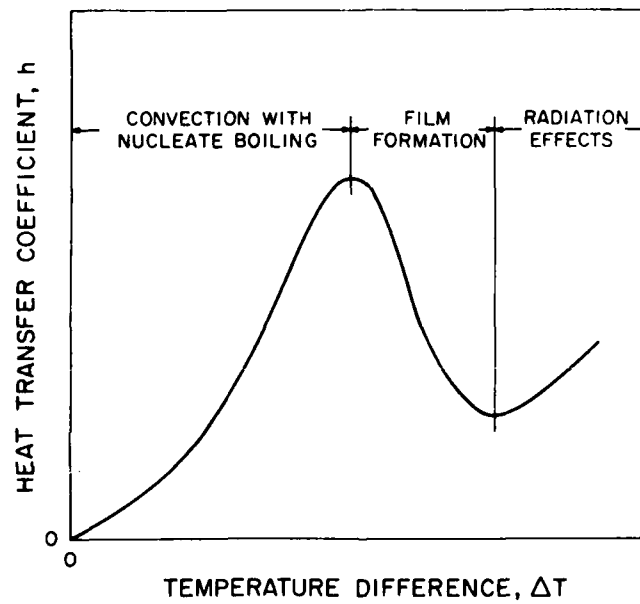


Fig. 7. Schematic for the variation of the heat transfer coefficient of water as affected by the solid surface temperature.

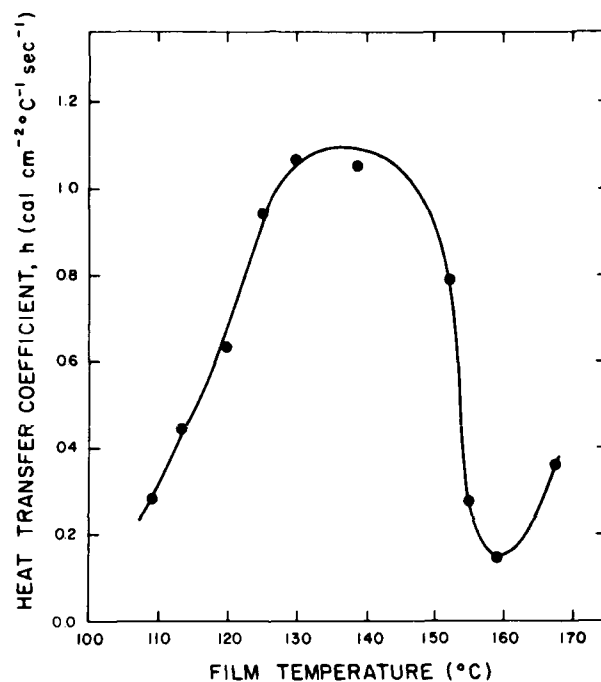


Fig. 8. Effective transfer coefficient for water inferred from the experimental ΔT_c values in figs. 4 and 6a.

show the same general trends as those shown schematically in fig. 7. It should be noted that these calculated data vary over an order of magnitude. Again, it is cautioned that these data are valid only for the particular testing conditions and materials of the present study. Unless verified, their use for other test conditions could lead to misleading results.

The data for the effective heat transfer coefficient for the water bath shown in fig. 8 permit a reasonable explanation for the absence of thermal stress failure in the majority of specimens with diameter of 0.318 cm quenched into water at 90°C. Because of their small size, as indicated by eq. 1, these specimens require high values of ΔT to induce thermal stress failure. Such high values of ΔT imply high film temperature with corresponding low values of the heat transfer coefficients. The few specimens in which failure could be induced represented the weakest specimens of the strength distribution for this size of specimen. It is likely that if the strength values for these specimen had been only slightly higher, failure would not have occurred for any of the specimens. On the other hand, slight reduction in the strength would have lowered ΔT_c with a corresponding large increase in heat transfer coefficient that all specimen would have failed.

Manson and Smith¹⁵ found for disc specimens peripherally quenched in water, that the thermal stresses were nearly constant with ΔT , exhibiting only a slight concavity with a maximum near $\Delta T_c \approx 120^\circ\text{C}$. At least qualitatively this suggests that the heat transfer coefficients for those experiments corresponded to the range of film temperature shown in fig. 8 which includes the maximum and the regime over which h decreases rapidly with increasing film temperature.

Becher et al.¹⁹ calculated the effective heat transfer coefficient from ΔT_c for a number of ceramic materials. A plot of these values against ΔT resulted in a curve similar to the one shown in fig. 8. However, if the values of h calculated from the present data were plotted in a similar manner, the h values for 90°C bath temperature would fall to the left of the data for the lower bath temperatures. This, then, no longer would result in the expected inverted V-shaped curve. For this reason, it appears preferable to use the concept of film temperature (or perhaps initial specimen temperature) in order to properly reflect changes in heat transfer coefficient due to differences in bath temperature.

Davidge et al.⁷ found that on increasing the water bath from 20 to 95°C resulted in a decrease in ΔT_c from 168 to 88°C for an alumina and from 95 to 45°C for a polycrystalline magnesium oxide. These observations appear to contradict the present findings. However, as judged by the relatively low values of ΔT_c for the samples of Davidge et al. (presumably due to low values of tensile strength), the corresponding film temperatures for bath temperatures of 20 as well as 95°C, fall in the region of nucleate boiling. In this region, the heat transfer coefficient increases rapidly with increasing film temperature so that a decrease in ΔT_c on increasing water bath temperature is reasonable. For the alumina of this study, however, ΔT_c is sufficiently high so that the heat transfer coefficient decreases with increasing value of ΔT . Consequently, ΔT_c increases with increasing bath temperature.

4. GENERAL

The data presented in this paper are illustrative of the difficulties encountered in establishing the relative thermal stress resistance of ceramic materials by the quenching method. The interpretation of experimental data obtained by this method requires a-priori quantitative data for the heat transfer characteristics of the fluid media used. Such data are not easily obtained. Furthermore, since the specimen continuously changes temperature, the heat transfer coefficient is expected to vary during the duration of the quench. Under these conditions a calculation of the thermal stresses, which takes into account time-dependent film temperatures and corresponding heat transfer coefficients, may have to rely on numerical methods. Spatial variations of the heat transfer coefficients around the specimens introduced an additional complexity.

For the above reasons, the heat transfer data shown in figs. 3 and 8 can only be described as "effective" since they were inferred from the experimental data. Although these data show the anticipated dependence on film temperature, their general applicability to other materials must be treated with caution. This is true, in particular, for the water bath, in which the heat transfer coefficient is affected by nucleate boiling and steam formation is expected to be a function of the surface condition (roughness, etc.) of the specimen. It is even conceivable that differences in thermal stress resistance of different materials (i.e. values of ΔT_c) can be found entirely due to differences in surface condition which modifies the heat transfer characteristics.

Even for materials with surface conditions which yield identical heat transfer coefficients for a given film temperature, the assessment of the relative thermal stress resistance based on data for ΔT_c is not simple. Consider two different materials with relatively low thermal stress resistance so that at ΔT_c , the corresponding film temperature for a water quench is in the nucleate boiling range. The material with the higher thermal stress resistance will require a higher value of ΔT_c . This however will involve a higher film temperature and corresponding higher value of the heat transfer coefficient. This, in turn, will suppress the value of ΔT_c . For this reason, differences in relative thermal stress resistance of two materials subjected to a water quench involving nucleate boiling may be difficult to assess.

The opposite effect occurs for two materials for which ΔT_c corresponds to values of film temperatures which involve steam-film formation. In this range even small differences in ΔT will involve large differences in heat transfer coefficient and corresponding large differences in ΔT_c . This situation, for instance could arise on comparisons of a polycrystalline aluminum oxide and a highly thermal shock resistant material such as high-strength hot-pressed silicon nitride. It seems reasonable to point out that water despite its convenience, appears less useful for measurement of thermal stress resistance by the quenching method.

Silicone oils, on the other hand, appear more suitable in view of their monotonic increase of the heat transfer coefficient with increasing film temperature. For these oils the relatively low value of effective heat transfer coefficient may prevent the use of very small specimen which

could be inconvenient especially for newly developed materials for which larger specimens may not be available. It is anticipated, however, that oils can be found or developed with heat transfer characteristics higher than those used in the present study.

A final recommendation is in order for purposes of facilitating quantitative comparison of results of different investigators. In reporting such results, the conditions of the quenching tests should be stated. This includes the bath temperature as well as the range of quenching temperature differences, in order to estimate the appropriate film temperature. In view of the rapid variation of the heat transfer coefficient with film temperature, especially for water, the actual temperature of the bath should be stated. Baths at nominal room temperature does not appear adequate, in view of large regional as well as seasonal variations of this quantity.

ACKNOWLEDGMENT

This study was carried as part of a research program funded by the Office of Naval Research under contract : N00014-78-C-0431.

Figure Captions:

- Fig. 1. Effect of bath temperature on ΔT_c for glass rods quenched in silicone oil: (a) 100 centistokes (b) 5 centistokes.
- Fig. 2. Effect of bath temperature on ΔT_c for alumina rods ($d = 0.63$ cm.) quenched in silicone oil (5 centistokes)
- Fig. 3. Effective heat transfer coefficient for silicone oil baths inferred from the thermal fracture data of figures 1a and 1b
- Fig. 4. Effect of bath temperature on ΔT_c for alumina rods ($d = 0.318$ cm.) quenched in water.
- Fig. 5. Probability of failure of alumina rods ($d = 0.318$ cm.) quenched in water at 90°C
- Fig. 6a. Effect of specimen size on ΔT_c for alumina rods quenched in water at 25 and 90°C
- Fig. 6b. Normalized $\Delta T_c'$ for alumina rods quenched in water at 25 and 90°C .
- Fig. 7. Schematic for the variation of the heat transfer coefficient of water as affected by the solid surface temperature
- Fig. 8. Effective heat transfer coefficient for water inferred from the experimental ΔT_c values in figs. 4 and 6a.

REFERENCES

1. B. A. Boley and J. H. Weiner, "Theory of Thermal Stresses" (Wiley and Sons, New York, 1960).
2. D. P. H. Hasselman, J. Am. Ceram. Soc. 52 (1969) 600.
3. W. D. Kingery, J. Am. Ceram. Soc. 38 (1955) 3.
4. D. P. H. Hasselman, Ceramurgia, 4 (1979) 147.
5. J. P. Singh, J. R. Thomas, Jr., and D. P. H. Hasselman, J. Am. Ceram. Soc. 63 (1980) 140.
6. D. P. H. Hasselman, J. R. Thomas, Jr., M. P. Kamat, and K. Satyamurthy J. Am. Ceram. Soc. 63 (1980) 21.
7. R. W. Davidge and G. Tappin, Trans. Brit. Ceram. Soc. 66 (1967) 405.
8. D. P. H. Hasselman, J. Am. Ceram. Soc. 53 (1970) 490.
9. E. Glenny and M. G. Royston, Trans. Brit. Ceram. Soc. 57 (1958) 645.
10. K. Anzai and H. Hashimoto, J. Mat. Sc. 12 (1977) 235.
11. R. Badaliance, D. A. Krohn and D. P. H. Hasselman, J. Am. Ceram. Soc. 57 (1974) 432.
12. W. Weibull, J. Appl. Mech. 18 (1951) 293.
13. D. P. H. Hasselman, R. Badaliance, K. R. McKinney and C. H. Kim, J. Mat. Sc. 11 (1976) 458.
14. J. C. Jaeger, Philos. Mag. 36 (1945) 418.
15. S. S. Manson and R. W. Smith, Trans. ASME. 78 (1956) 533.
16. K. Satyamurthy, J. P. Singh, D. P. H. Hasselman and M. P. Kamat, J. Am. Ceram. Soc. (in press)
17. F. Kreith, "Principles of Heat Transfer," (Intext Educational Publishers, New York, 1973).
18. E. B. Shand, "Glass Engineering Handbook" (McGraw-Hill Book Co., Inc., New York, 1958).
19. P. F. Becher, D. Lewis III, K. R. Carman and A. C. Gonzalez, J. Am. Ceram. Soc. 59 (1980) 542.

CHAPTER II

IMPROVEMENT OF THERMAL SHOCK RESISTANCE OF BRITTLE STRUCTURAL CERAMICS BY A DISPERSED PHASE OF ZIRCONIA

N. Claussen* and D. P. H. Hasselman**

*Max-Planck Institute, Stuttgart, West Germany

**Virginia Polytechnic Institute and State University,
VA, USA

ABSTRACT

This paper discusses the effect of unstabilized zirconia dispersions on the thermal shock resistance of brittle structural ceramics.

A general discussion is given of the preferred direction of modification of the pertinent material properties which affect thermal shock resistance. The nature of the crystallographic phase transformation in the zirconia and its effect on these properties is presented. The zirconia dispersed phase can lead to significant improvements in fracture toughness by transformation - or microcrack toughening. The volume change during the zirconia phase transformation also lowers the effective coefficient of thermal expansion. Surface compressive stresses which result from the phase transformation during surface grinding also are beneficial in improving thermal shock resistance. The zirconia phase also can change the unstable (catastrophic) mode of failure to the more preferred stable one with decrease in fracture stress.

These effects are illustrated by experimental data for composites, consisting of zirconia dispersions in aluminum oxide, silicon nitride and zircon matrices.

INTRODUCTION

The advantageous properties of ceramic materials such as their excellent high-temperature strength, creep and corrosion resistance, make them ideal candidates for the replacement of such

materials as metal super-alloys for turbine engines and many other engineering applications involving extreme temperatures. Unfortunately, ceramic materials display one unfavorable characteristic, namely an extreme brittleness or notch-sensitivity. This high degree of brittleness renders such materials highly susceptible to catastrophic failure under conditions of thermal shock. Because of the absence of any kind of plasticity, the non-uniform thermal expansions which result from the non-uniform temperatures, cannot be accommodated by non-linear deformation. The low value of fracture toughness of brittle ceramics also contributes to extensive crack propagation following thermal stress failure. This frequently renders any structure or component made from brittle ceramics completely incapable of continued satisfactory performance following the fracture due to thermal stresses.

In order to fully capitalize on the very favorable properties of structural ceramic materials, it is imperative that their thermal shock resistance be improved significantly. In this respect it should be noted that ceramic composites exhibit greater thermal shock resistance than single-phase ceramic materials (1,2,3). More recent results have shown that the introduction of an unstabilized ZrO_2 dispersed phase in a brittle matrix can lead to a significant enhancement of many mechanical properties, such as strength and fracture toughness, of importance to the resistance to thermal stress fracture. This effect is attributed to the unique tetragonal-to-monoclinic phase transformation encountered in zirconia (4-9).

The purpose of this paper is to summarize the role of this phase transformation in enhancing the thermal shock resistance of brittle ceramic materials.

FUNDAMENTALS

In order to establish the role of the zirconia dispersions, a brief overview will be given of the pertinent material properties which govern the thermal stress failure of brittle materials.

a. Initiation of Thermal Stress Failure

For structures or components in which thermal stress failure cannot be tolerated, the material properties for a given design must be selected such that the maximum thermal stresses do not exceed the failure stress of the materials. Generally, brittle materials exhibit values of the tensile strength well below the compressive strength. For this reason, thermal stress failure of brittle materials usually occurs in tension.

The usual procedure followed in ceramic technology for establishing the role of the pertinent material properties which affect

thermal stress failure of a brittle material subjected to a given thermal environment, is to derive an expression for the maximum tensile thermal stresses developed. By equating this value of stress to the tensile strength, an expression is then obtained for the maximum thermal environment (i.e., temperature difference, heat flux, etc.) to which the material can be subjected without incurring thermal stress failure. As an example, the maximum temperature difference to which the ceramic structure can be subjected, can be expressed:

$$\Delta T_{\max} = \frac{A\sigma_f(1-\nu)K}{\alpha E} \quad (1)$$

where A is a constant depending on the geometry of the structure, σ_f is the tensile fracture stress, ν is Poisson's ratio, K is the thermal conductivity, α is the coefficient of thermal expansion and E is Young's modulus.

In fracture-mechanical terms, the tensile strength can be expressed:

$$\sigma_f = YK_{Ic}/a_o^{1/2} \quad (2)$$

where Y is a constant related to the geometry of the failure-initiating crack, K_{Ic} is for critical stress intensity factor (fracture toughness) the mode I crack-opening and a_o is a measure of the crack size or depth.

Substitution of eq. 2 into eq. 1 yields:

$$\Delta T_{\max} = \frac{AYK_{Ic}(1-\nu)K}{\alpha E a_o^{1/2}} \quad (3)$$

If in the region of the failure initiating flaw, a compressive stress (σ_c) exists, ΔT_{\max} can be expressed by:

$$\Delta T_{\max} = \frac{AYK_{Ic}(1-\nu)K}{\alpha E a_o^{1/2}} + \frac{A\sigma_c(1-\nu)K}{\alpha E} \quad (4)$$

b. Crack Propagation in Thermal Stress Fields

In high-temperature technology, frequently the situation is encountered that even in materials with the highest thermal stress resistance, thermal stress failure cannot be avoided. In this case, thermal stress resistance is not measured in terms of the maximum thermal condition to which the materials can be subjected without failure. Instead, thermal shock resistance is measured by the ability of the material to render continued satisfactory

service in spite of having undergone thermal stress failure. One such popular measure for this criterion is the strength retained following thermal stress failure. The retained strength is a measure of the size of the arrested cracks which resulted from the failure process.

A simple fracture-mechanical analysis of the nature of dynamic crack propagation in a thermal stress field has shown that the size of the crack (a_f) after propagating and arrest is inversely proportional to a ratio, which involves the energy (Y_f) required to create unit area of new crack surface, Young's modulus (E), the initial fracture stress (σ_f) and the number of cracks (N), written as:

$$a_f = f(Y_f E / \sigma_f^2 N) \quad (5)$$

From eq. 2, the strength (σ_a) retained after thermal stress failure is:

$$\sigma_a = Y K_{Ic} / a_f^{1/2} \quad (6)$$

From eqs. 2, 5 and 6, it can be concluded that for a given number of cracks, the strength retained after failure is an inverse function of the initial strength or:

$$\sigma_a = f(\sigma_f^{-1}) \quad (7)$$

In terms of the objectives of this paper, eqs. 1, 3 and 7, indicate the problem faced by the materials technologist in selecting or developing brittle materials subjected to high values of thermal stress. As shown by eq. 3, for a given value of K_{Ic} , thermal stress resistance as measured by ΔT_{max} can be increased by decreasing the flaw size. This, in effect, increases the initial tensile strength. Unfortunately, however, as indicated by eq. 7, if this increase in strength is not sufficient and failure still occurs, the only effect would be to increase the size of the cracks after fracture and to decrease the resulting load-bearing ability of the material. In fact, for ultra-high-strength structural ceramic materials, thermal stress failure can be quite explosive, rendering the structure or component completely useless for further service. In fact, the preferred approach would be to increase the original crack size. This has the further advantage, that if the flaw size becomes large enough, crack propagation will occur in a stable manner. At the same time high strength can be retained both before and after failure, by increasing the fracture toughness as much as possible. In addition, reductions in the coefficient of thermal expansion and Young's modulus, if possible, results in further improved thermal stress resistance.

These conclusions are summarized in Fig. 1, which shows the typical strength behavior following thermal shock of increasing

severity. The discontinuity of strength at ΔT_c is the result of the dynamic crack propagation. For stable crack propagation, no such instantaneous strength loss occurs with strength decreasing monotonically for values of $\Delta T > \Delta T_c$. Included in Fig. 1, are the ratios of the pertinent material variables which need to be modified to increase thermal stress resistance. Further improvements in thermal stress resistance as indicated by eq. 4 can also be achieved by creating a compressive stress, which opposes the tensile thermal stress, in the region of the material where the failure originates.

Experimental data have indicated that incorporating a zirconia dispersed phase in a brittle matrix material can lead to significant improvements in thermal stress resistance by increasing the fracture toughness, lowering the coefficient of thermal expansion, introducing compressive stresses and by changing the failure mode to the preferred stable mode of crack propagation as demonstrated in the following sections.

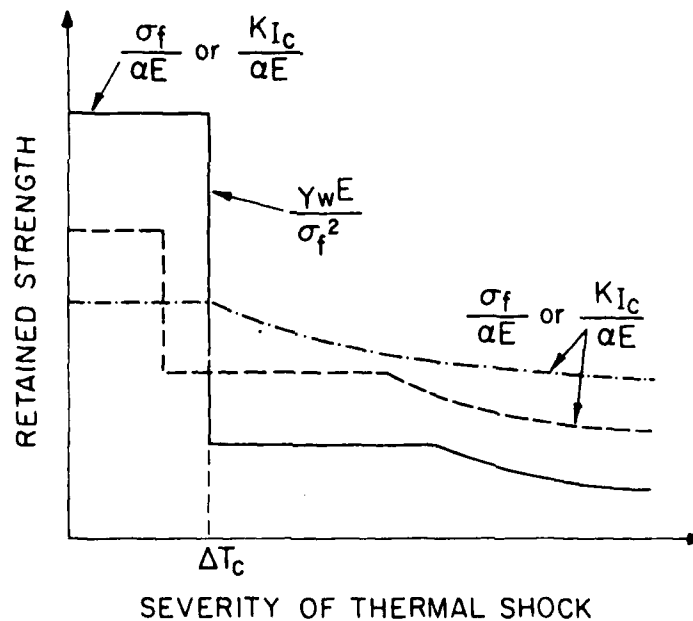


Fig. 1. Variation of strength of typical brittle ceramic subjected to thermal quench of increasing severity and appropriate ratios of material properties relevant to thermal stress resistance. Solid curve: high-strength ceramic; dotted curve: low strength ceramic.

NATURE OF ZIRCONIA PHASE TRANSFORMATION

In order to understand the role of the zirconia dispersions in improving thermal stress resistance, the nature of the tetragonal-monoclinic phase transformation should be examined.

Figure 2 shows a diagram of a zirconia particle incorporated in a matrix before (t = tetragonal) and after (m = monoclinic) its transformation. The lower half of Fig. 2 shows the thermal expansion behavior of a brittle matrix containing zirconia inclusions. On cooling from high temperatures, the inclusions go through the transformation at a temperature T_R , which involves a 3-5% volume expansion. The tangential stresses in the matrix, caused by this expansion, can lead to microcrack formation when the particle diameter exceeds a critical value d_{RC} (12). On reheating the particles can retransform to the tetragonal phase at a temperature T_H . Generally $T_H > T_R$ so that the expansion behavior shows a hysteresis. The height of the hysteresis curve is a function of the volume fraction of zirconia. The temperatures T_R and T_H are a function of

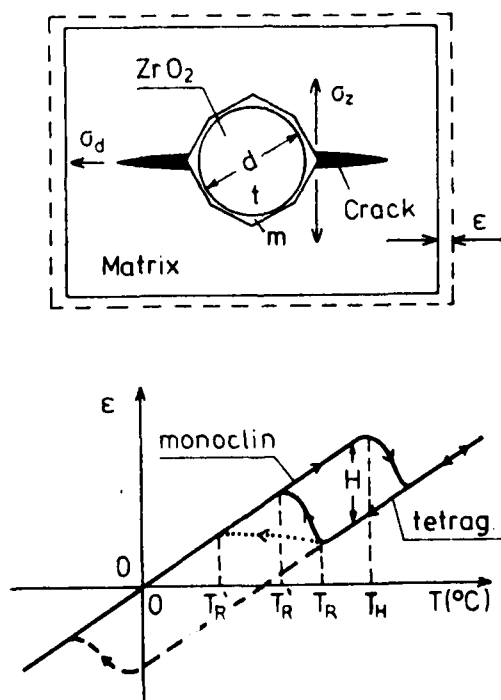


Fig. 2. Zirconia particle contained within ceramic matrix, before (t) and after (m) the tetragonal-monoclinic phase transformation and associated thermal expansion behavior of the composite.

the zirconia particle size and the constraint provided by the matrix. T_R and T_H generally decrease with decreasing particle size. Thus, by controlling the particle size, the nature of the micro-cracking in the matrix as well as the temperature range over which the transformation occurs can be controlled.

EFFECT OF PHASE TRANSFORMATION IN ZIRCONIA ON MATERIAL PROPERTIES AND STATE OF STRESS

The tetragonal-to-monoclinic phase transformation in the zirconia dispersions has a profound effect on a number of material properties which control thermal stress resistance as follows:

1. Fracture toughness (K_{Ic}) can be modified by two methods referred to as micro-crack toughening and transformation toughening. At sufficiently large zirconia particle size, the hoop stresses can cause extensive micro-cracking in the matrix. During failure, these micro-cracks promote crack bifurcation and an enhanced dissipation of energy, thereby effectively increasing the fracture toughness. Figure 3 indicates the increase in fracture toughness which can be achieved in this manner for four different ceramic matrix materials.

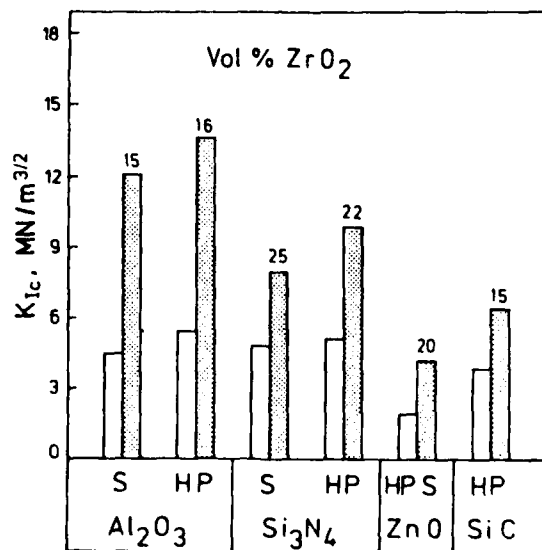


Fig. 3. Fracture toughness at room temperature of ceramic matrix materials without (white bars) and with (grey bars) various volume percentages of a dispersed zirconia phase indicated by the number above the grey bars.

Transformation toughening can occur by zirconia dispersions of sufficiently small size, which as the result of the matrix constraint retain their tetragonal crystal structure at room temperature. However, during fracture, the high stresses in the immediate region of the crack tip cause a temporary removal of the constraint. This permits the phase transformation to take place. The particles now, however, have a larger volume, so that a passage of the stress field of the crack, a major modification in the matrix stress field is encountered, thereby effectively increasing the fracture toughness significantly.

2. Compressive stresses. The zirconia phase transformation can cause the creation of compressive stresses which can oppose the tensile thermal stresses. This effect can be achieved by two mechanisms (16,17). Steady-state compressive stresses can be created by the stress-induced phase transformation. One very effective method by which this can be achieved is to cut or grind the surface. The volume expansion associated with the transformation leads to the formation of high compressive stresses in the immediate surface regions. Figure 4 shows the increase in bend strength and fracture toughness which can be achieved by this method. Figure 4

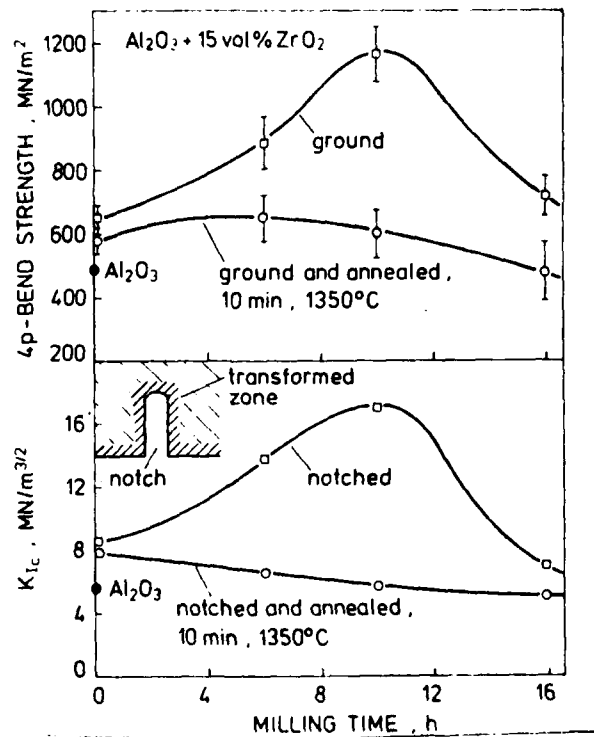


Fig. 4. Effect of anneal and milling time on flexural strength and fracture toughness of hot-pressed alumina with 15 vol.% ZrO₂, in which tetragonal-to-monoclinic phase transformation was induced by surface grinding and cutting.

also contains data for the effect of micro-crack toughening on strength and fracture toughness, labelled "ground and annealed." Annealing causes a relaxation of the surface stresses so that any remaining improvements in strength and toughness must be attributed to effects other than surface compression. In fact, at the very short (milling) time for mixing the alumina and zirconia powders, the observed increase in toughness is due to micro-crack toughening, because the zirconia particle size is still quite large. The decrease in fracture toughness with increased milling time is due to the accompanying decrease in particle size.

Thermal stresses arise from temperature non-uniformities. Because of this non-uniformity of temperature, the temperature dependence of the phase transformation permits the introduction of transient compressive thermal stresses which oppose the tensile thermal stresses. During cooling, for, instance, the maximum thermal stresses occur in the surface, where also the transformation will occur first. The volume expansion associated with this transformation created a compressive stress in the surface which opposes the tensile thermal stress due to the greater degree of cooling. It should be noted here that this mechanism for improving thermal stress resistance, is effective only for cooling from temperature immediately above or within the range of transformation temperature. A similar statement must be made for compressive stresses created by surface grinding. Such stresses are useful only when the tensile thermal stresses exist in the surface alone as in the case for transient cooling.

3. Coefficient of thermal expansion. As indicated in Fig. 2, the volume expansion which accompanies the phase transformation on cooling, in effect, reduces the effective coefficient of thermal expansion. Since the range of transformation temperature is a function of the particle size incorporating a bi-modal particle size distribution results in a widening of this temperature range. In fact, a coefficient of thermal expansion near zero can be created between about 80°C and room temperature. This effect is indicated schematically in Fig. 5.

4. Stable crack propagation. When a high density of micro-cracks of sufficient size is introduced in a matrix such that its elastic behavior is affected, crack propagation in a thermal stress field will become stable. Strength loss with increasing severity of thermal shock will be monotonic rather than discontinuous for unstable crack propagation as shown in Fig. 1. Crack sizes resulting from stable crack propagation generally are smaller than those which result from unstable crack propagation. For this reason, although perhaps initially rather weak, materials which fail in a stable manner under conditions of thermal shock will exhibit superior strength behavior following the thermal shock. This fact is used to advantage in refractory structures in which thermal stress failure generally cannot be avoided, but in which the structural materials nevertheless must render satisfactory

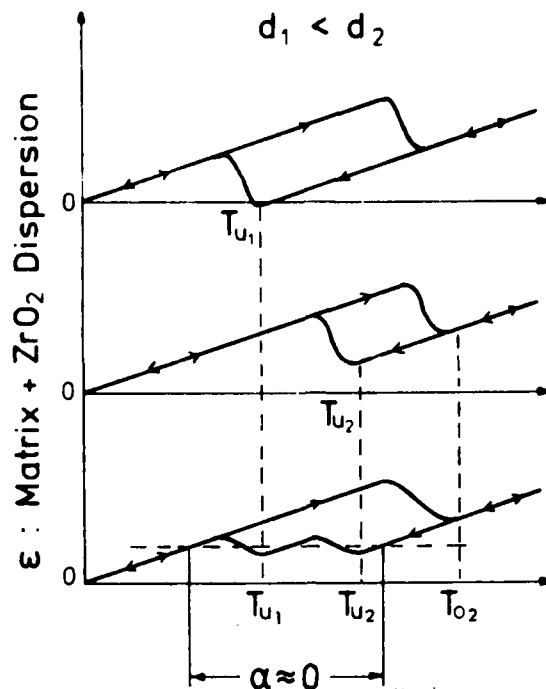


Fig. 5. Thermal expansion behavior of ceramic matrix with zirconia inclusions with bi-modal particle size distribution.

service in spite of being in a partially fractured condition.

The introduction of a zirconia dispersed phase can also be used successfully to change the undesirable unstable failure mode of a brittle matrix to the more preferred stable one. This, however, will require relatively large particle sizes and high volume fractions to assure a significant decrease in Young's modulus, a prerequisite for stable crack propagation. As an example, 20 vol.% ZrO_2 particles with a diameter of approximately $10 \mu m$ in an alumina matrix caused a decrease in Young's modulus and bend strength from about $400 GN.m^{-2}$ and $500 MN.m^{-2}$ to about $150 GN.m^{-2}$ and $170 MN.m^{-2}$. Of interest to note is, that the microcracking in the matrix had little or no effect on the strain-at-fracture, frequently used as a measure for thermal stress resistance. In fact, extensively microcracked materials can exhibit strains-at-fracture an order of magnitude above that for crack-free materials.

THERMAL SHOCK DATA

Experimental data were obtained to illustrate many of the above phenomena (18,19,20). For all materials studied, specimens

were subjected to thermal shock by quenching from higher temperature into a water bath at room temperature followed by a strength determination in 4-point bending.

Figure 6 shows the strength behavior of an alumina matrix with about 20 vol.% ZrO_2 dispersions of various sizes. The 100% alumina with initial strength of approximately 500 MN.m^{-2} exhibited a critical quenching temperature difference of approximately 200°C . The introduction of the zirconia particles with a diameter of approximately $1 \mu\text{m}$, as the result of transformation toughening, raised the strength to about 650 MN.m^{-2} and ΔT_c to about 300°C , a substantial improvement. Note that for the latter two materials as indicated by the instantaneous strength loss at ΔT_c fracture occurred by unstable crack propagation. This unstable mode of failure can be changed to the stable one by incorporation of particles with sizes of 5 and $10 \mu\text{m}$. Note that the incorporation of these larger particles not only has improved ΔT_c , but also that the strength for the composites for both particle sizes, at high values of ΔT exceeds the corresponding values for the 100% alumina as well as the alumina with the $1 \mu\text{m}$ dispersions.

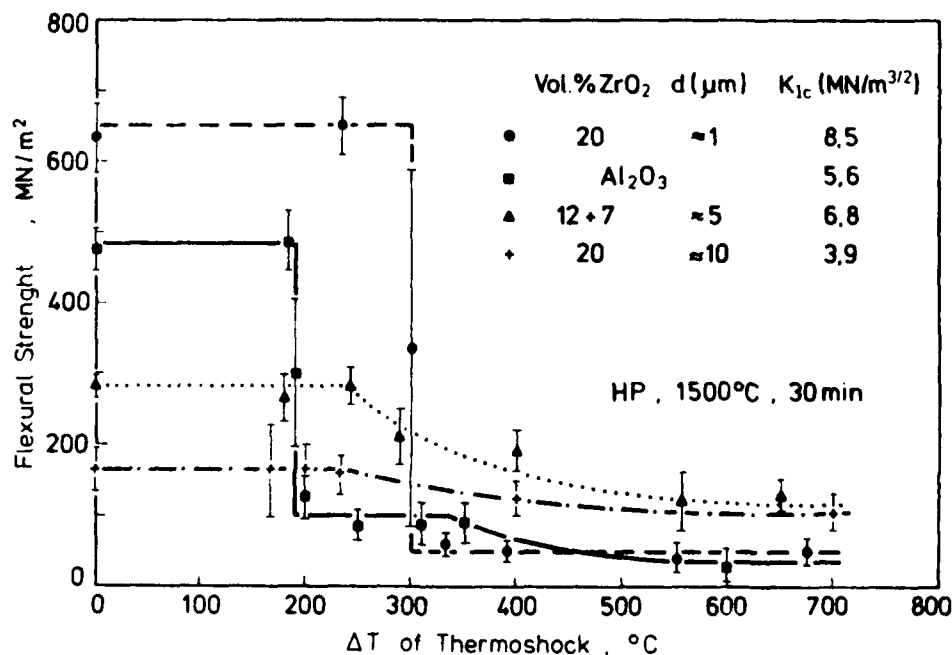


Fig. 6. Effect of quenching temperature difference on strength of composites of alumina with zirconia dispersions of different sizes, quenched into water at 20°C .

As an illustration of the decrease in the coefficient of thermal expansion or the existence of a transient compressive surface compressive stress, Fig. 7 compares the strength behavior of silicon nitride (lightly dotted curve) and silicon nitride with 20 vol.% ZrO_2 , subjected to a similar quench as the alumina of Fig. 6. The particle size of the zirconia was such that the temperature for the phase transformation ranged from about 600 to 850°C. Since the specimens were at room temperature prior to reheating below 850°C the zirconia is in the low temperature monoclinic modification. Therefore, in quenching from below this temperature, no advantage is obtained from the phase transformation. In Fig. 7 this is indicated by the data points in the form of the crosses. However, on heating to above 850°C, the high-temperature tetragonal phase is obtained, which upon quenching reverts back to the monoclinic form so that thermal stress failure is avoided as indicated in Fig. 7. Fracture by quenching from 600-850°C can be avoided only if the specimens are

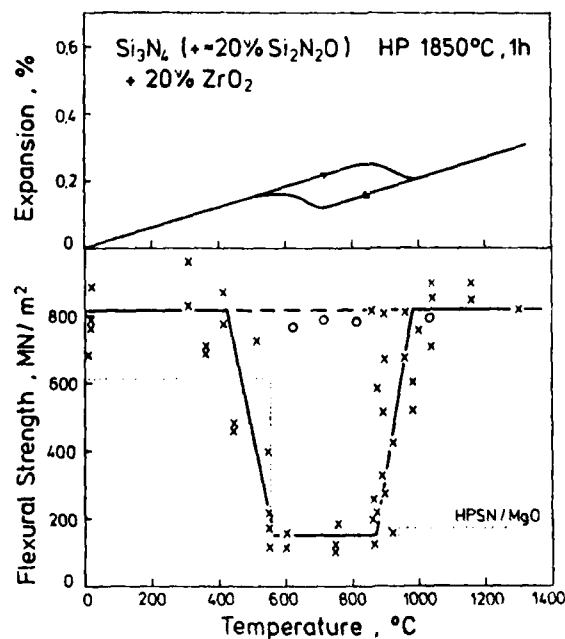


Fig. 7. Thermal expansion and retained strength after thermal quench of silicon nitride with zirconia dispersions. For meaning of different data points the reader is referred to the text. Dotted lines indicate strength behavior of silicon nitride without zirconia dispersions.

first heated to higher temperature to achieve the tetragonal crystal structure, followed by slow cooling to the desired temperature from which the specimens are to be quenched. In Fig. 7 the feasibility of this procedure is shown by the data points indicated by circles.

Figure 8 shows the effect of the ZrO_2 dispersions on the thermal shock behavior of zirconium silicate. For the 100% zirconium silicate, the strength loss behavior is typical of unstable crack propagation shown in Fig. 1. The effect of the 10 wt.% zirconia dispersions is to modify the fracture mode to the stable one, as indicated by the monotonic decrease in strength for $\Delta T \geq \Delta T_c$. This effect must be attributed to an increase in the size of the failure initiating flaws. Of interest to note is that this increase in the flaw size did not result in a decrease in the strength. This implies that the decrease in flaw size must have been accompanied by a simultaneous increase in fracture toughness, due to microcrack toughening. It is clear from the data of Fig. 8 that the zirconium silicate with zirconia dispersions is much preferred over the 100% zirconium silicate as a material for high-temperature structures susceptible to thermal stress failure.

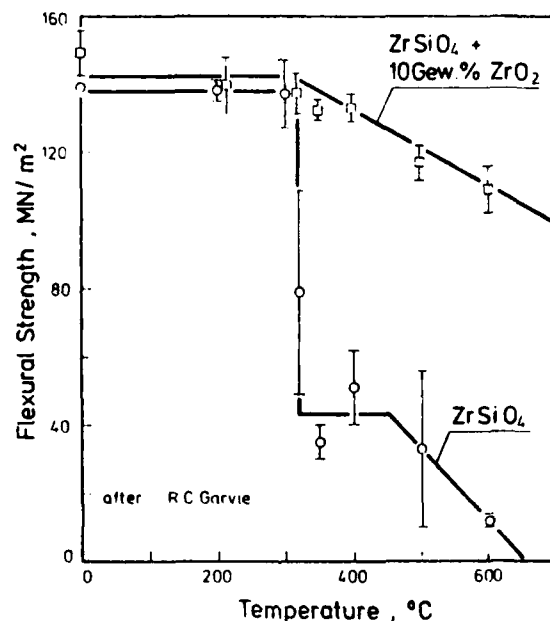


Fig. 8. Effect of quenching temperature difference on strength of zirconium silicate with and without zirconia dispersions, quenched into water at 20°C .

CONCLUSION

The discussion and experimental data presented in this paper indicate that the incorporation of a zirconia dispersed phase, can lead to substantial improvements in the thermal stress resistance of brittle structural materials.

ACKNOWLEDGMENTS

The preparation of this manuscript was supported by the Max-Planck Institute and the Office of Naval Research under contract No.: N00014-78-C-0413. The authors are indebted to J. P. Singh for review of the manuscript.

REFERENCES

1. Alan Arias, "Thermal Shock Resistance of Zirconia with 15 Mole % Titanium," J. Amer. Ceram. Soc., 49 (1966) 334.
2. K. Chyung, "Fracture Energy and Thermal Shock Resistance of Mica Glass-Ceramics," Fracture Mechanics of Ceramics, edited by R. C. Bradt, D. P. H. Hasselman and F. F. Lange, Plenum Press, New York (1974).
3. R. C. Rossi, "Thermal Shock Resistance Ceramics with Second-Phase Dispersion," Amer. Ceram. Soc. Bull., 48 (1969) 736.
4. N. Claussen, "Fracture Toughness of Al_2O_3 with an Unstabilized Dispersed Phase," J. Amer. Ceram. Soc., 59 (1976) 49.
5. R. C. Garvie, R. H. Hannink, and R. T. Pascoe, "Ceramic Steel," Nature, 258 (1973) 703.
6. D. L. Porter, and A. H. Heuer, "Mechanism of Toughening Partially-Stabilized Zirconia (PSZ)," J. Amer. Ceram. Soc., 60 (1977) 183.
7. N. Claussen, J. Steeb, and R. F. Pabst, "Effect of Induced Microcracking on the Fracture Toughness of Ceramics," Amer. Cer. Soc., Bull., 56 (1977) 559.
8. D. L. Porter, A. G. Evans, and A. H. Heuer, "Transformation-Toughening in Partially-Stabilized Zirconia (PSZ)," Acta. Met., 27 (1979) 1649.
9. N. Claussen, "Stress-Induced Transformation of Metastable Tetragonal ZrO_2 Particles in Ceramic Matrices," J. Amer. Ceram. Soc., 61 (1978) 85.
10. D. P. H. Hasselman, "Figures-of-Merit for the Thermal Stress Resistance of High-Temperature Brittle Materials," Ceramurgia, 4 (1979) 147.
11. D. P. H. Hasselman, "Unified Theory of Thermal Shock Fracture Initiation and Crack Propagation of Brittle Ceramics," J. Amer. Ceram. Soc., 52 (1969) 600.
12. N. Claussen and J. Jahn, "Transformation of ZrO_2 particles in a Ceramic Matrix," Ber. Dt. Keram. Ges., 55 (1978) 487.
13. E. C. Subbarao, H. S. Maiti and K. K. Srivastava, "Martensitic Transformation in Zirconia," Phys. Stat. Sol., (a) 21 (1974) 9-40.
14. F. F. Lange in Fracture Mechanics of Ceramics, Vol. 2, R. C. Bradt, D. P. H. Hasselman and F. F. Lange, Plenum Publ. Corp., New York (1974).
15. R. C. Garvie, "The Occurrence of Metastable Tetragonal Zirconia as a Crystallite Size Effect," J. Phys. Chem., 69 (1965) 1238.

16. N. Claussen and R. Wagner, 1979, "Influence of Surface Condition on Strength of Al_2O_3 Containing Tetragonal ZrO_2 ," Amer. Ceram. Soc. Bull., 58 (1978) 883.
17. R. T. Pascoe and R. C. Garvie, in R. M. Fulrath and J. A. Pask (Eds.), Ceramic Microstructures, '76, Westview Press, Boulder, Colorado (1977).
18. N. Claussen and J. Jahn, "Mechanical Properties of Sintered and Hot-Pressed Si_3N_4 - ZrO_2 Composites," J. Am. Ceram. Soc., 61 (1978) 94.
19. R. C. Garvie, personal communication.
20. N. Claussen and G. Petzow, "Strengthening and Toughening Compacts in Ceramics," Proc. 4th CIMTEC, St. Vincent, Italy (1979).

CHAPTER III

EFFECT OF PHASE COMPOSITION AND MICROSTRUCTURE
ON THE THERMAL DIFFUSIVITY OF SILICON NITRIDE

by

G. Ziegler^{*}

and

D. P. H. Hasselman^{**}

^{*}Institut für Werkstoff-Forschung
DFVLR, 5000 Köln 90, W. Germany

^{**}Department of Materials Engineering
Virginia Polytechnic Institute and
State University
Blacksburg, Va. 24061, USA.

EFFECT OF PHASE COMPOSITION AND MICROSTRUCTURE
ON THE THERMAL DIFFUSIVITY OF SILICON NITRIDE

G. Ziegler^{*}, D. P. H. Hasselman[†]

^{*}Institute of Materials Research, DFVLR, Cologne, Germany

[†]Virginia Polytechnic Institute and State University
Blacksburg, Virginia 24061, USA

The effect of compositional and microstructural variables and processing conditions on the room temperature thermal diffusivity of hot-pressed and reaction-sintered silicon nitride was determined. The thermal diffusivity for hot-pressed silicon nitride increases with β -content. Maximum thermal diffusivity is reached at about 3 wt.% MgO. The higher thermal diffusivity of the β -phase is attributed to its higher purity level and the less distorted crystal structure compared to the α -phase.

In reaction-sintered nitride the thermal diffusivity is strongly influenced by the relative amount and needle-like morphology of the α -phase. Correlations of the thermal diffusivity with mechanical properties are discussed.

1. Introduction

The conduction of heat in dielectric materials depends strongly on the density and nature of structural lattice imperfections such as dislocations, vacancies, lattice vibrations and the degree of crystallinity [1, 2, 3]. Microstructural defects such as pores, grain boundaries (at low temperature) and microcracks also have a significant effect on

heat conduction properties [4, 5, 6]. Impurities and alloying elements also are known to inhibit the rate of heat conduction in dielectric materials considerably [4, 7].

Because of their many advantageous properties, dielectric ceramics, such as silicon nitride and others, are candidate materials for high-temperature energy conversion devices such as the all-ceramic turbine or in the form of replacements for many metallic components in internal combustion engines. The performance and efficiency of such systems in addition to many other properties depends critically on the thermal conductivity and thermal diffusivity of the materials of construction. High engine efficiency frequently requires a low thermal conductivity in order to minimize heat losses. On the other hand for good resistance to failure due to thermal stresses high values of the thermal conductivity and diffusivity are preferred. For purposes of reliable engineering design and the achievement of the proper trade-offs it is essential that the values of thermal conductivity and thermal diffusivity of such dielectric ceramics and the variables which control them are well understood.

In this respect, silicon nitride is expected to be very complex. Silicon nitride in the hot-pressed form (HPSN) can exhibit different densities as well as different crystal structures. Hot-pressed silicon nitride can consist of varying amounts of the α -phase and the β -phase which are bonded together by a grain boundary phase. The amount, composition, crystallinity of the grain boundary phase are expected to play a major role in establishing the values for the heat conduction properties. Reaction-sintered silicon nitride (RSSN) can exhibit variations in density, free unreacted silicon content, different crystal

structures as well as a wide range of pore sizes and shape. The matrix of reaction-sintered silicon nitride consists mainly of the two modifications α and β which are different in grain size and grain shape. The α -matte containing very small pores is characterized by very thin whisker-shaped crystallites; the β -phase exists in equiaxed grain [8, 9]. All these microstructural variables are expected to effect heat conduction profoundly. The wide variation of reported values of the thermal conductivity and diffusivity of silicon nitrides including CVD-Si₃N₄ and the sialons is well documented [10, 11, 12, 13, 14].

The purpose of the present study was to determine the thermal diffusivity of well-characterized hot-pressed and reaction-sintered silicon nitride in which by systematic variations of grain size and composition of the starting powder and through careful process control many of the pertinent compositional and microstructural parameters were isolated as much as possible.

2. Experimental

2.1 Sample Preparation

2.1.1 Hot-pressed silicon nitride

The microstructure of hot-pressed silicon nitride can be controlled by variation of phase composition and morphology of the starting powder and by the type and amount of sintering aids as well as by change of the processing parameters as temperature, pressing time and pressure during hot-pressing process [15, 16, 17, 18]. In this investigation MgO was used as sintering aid. To study the effect of crystal structure and the amount of glassy phase two sets of specimens were prepared:

Set I : Variation of the amount of β -phase at constant amount of 5 wt.% MgO sintering aid. These specimens were hot-pressed at a temperature of 1973 K for various lengths of time to result in certain percentage of the β -phase.

Set II: Variation of the amount of MgO content between 1 and 10 wt.% for constant β -amount of 100%. Specimens were hot-pressed at 2053 K. Hot-pressing time was changed in such a way that for each grade with different MgO content complete transformation was just achieved.

For the preparation of these above specimens a commercial Si_3N_4 powder* was used with a 0.04 fraction of β -phase and a specific surface area of $8.8 \text{ m}^2/\text{g}$. The impurity contents of the powder were (in wt.%): 0.02 Al; 0.04 Ca; 0.04 Fe; 0.6 C. This powder was mixed with different amounts of MgO under isopropanol using a teflon container with agate balls. The powders were hot-pressed under vacuum at a pressure of 31 MN/m^2 . From the hot-pressed discs, 75 mm diameter, 6 mm height, circular (diameter 12.5 mm) or rectangular plates (5 mm by 5 mm) with a thickness of 2.1 mm were prepared. These samples were cut in such a way that the measured thermal diffusivity corresponded to heat flow parallel to the hot-pressing direction. Both sides of the plates were diamond ground.

2.1.2 Reaction-sintered silicon nitride

Three sets of specimens of reaction-sintered silicon nitride were prepared following procedures described elsewhere [9, 19, 20]. In set I artificial pores of different sizes were introduced by mixing the starting silicon powders with 4 vol.% of an organic combustible wax of dif-

* H. C. Starck, Goslar, West-Germany.

ferent particle sizes (0.36 μm ; 63-90 μm ; 125-180 μm). These mixtures were isostatically pressed and the wax particles were burnt out at 653 K. In set II and III at nearly constant total porosity the pore structure was varied by using different grain sizes of the starting silicon powder (< 10 μm ; 10-37 μm ; 37-63 μm). These specimens were prepared by injection-molding. The specimens of all three sets nitrided at 1673 K for 100 hrs in a mixture of 90 vol.% N_2 and 10 vol.% H_2 at constant pressure of 950 mbar. More experimental details of the nitridation procedure are given by [9].

2.2 Microstructural and Crystallographic Characterization

The density was determined by the Archimedes principle using H_2O at 20°C for HPSN and mercury at 20°C and atmospheric pressure for RSSN. Pore and grain structure of HPSN and RSSN were examined by light and scanning electron microscopy on unetched and on etched sections and on fracture surfaces. The content of the α - and β -phases were established by quantitative X-ray crystallography. The free Si content was determined by means of optical metallography and by X-ray crystallography. For HPSN quantitative grain size data were determined from polished and etched surfaces (etching with $\text{HF} + \text{H}_2\text{O}_2 + \text{HNO}_3$ - determination of the mean grain intercept [17, 18]). For RSSN changes in the distribution of the pore-opening diameter of the bottle-shaped pores (micropores) were determined using mercury pressure porosimetry. The degree of nitridation in RSSN was calculated from the weight gain during the nitriding process [8]. The morphology of the α -phase in RSSN was determined on Ar ion-etched microsections [8] and on unetched fracture surfaces.

2.2.1 Hot-pressed silicon nitride

During the hot-pressing process at temperatures above 1500°C a liquid phase is formed and the α -crystals dissolve in the liquid and the β -crystals are recipitated. Using MgO as sintering aid the molten magnesia silicates at the grain boundaries solidifies during cooling mainly in the glassy state. The thickness of the grain boundary phases is in the order of 10-100 Å [17]. During the α to β transformation an elongated growth of β -crystals takes place due to different growth rates perpendicular and parallel to the c-axis [17]. The mean grain size varies from 0.3 to 1.5 μm with a shortest diameter of the rod-like β -grains between 0.2 and 2 μm and the length of the elongated grains up to 10 μm .

Figure 1 shows the density and the $\beta/\alpha+\beta$ ratio of the hot-pressed specimens of set I with 5 wt.% MgO as a function of hot-pressing time at 1973 K. The densification occurs in the early stage of the hot-pressing process. As expected the β -content increases with increased duration at temperature. The kinetics of the α to β transformation are strongly influenced by the amount of the glassy phase, the number of the pre-existing β -grains in the starting powder and the processing conditions such as temperature and pressure during hot-pressing [15, 16, 17]. With regard to the amount of the sintering aid this means that the time required for complete conversion of the $\alpha\text{-Si}_3\text{N}_4$ to $\beta\text{-Si}_3\text{N}_4$ decreases with increasing MgO content.

Figure 2 shows the change in microstructure during α to β transformation in set I. After short hot-pressing time a fine grained mostly equiaxed grain structure is observed. With increasing hot-pressing time a change in grain morphology from equiaxed to prismatic rod-like grains takes place accompanied by the growth of elongated grains.

For the specimens in Set II, Fig. 3 gives the density as a function of MgO content for hot-pressing times required for a 100% conversion of the α - into the β -phase. The density indicates a slight decrease with increasing MgO content. The deviations from theoretical density of $3.20 \text{ g}\cdot\text{cm}^3$ probably is the result of the relatively high amount of the grain boundary glassy phase. For all MgO contents the microstructure consists of elongated β -grains. The values of the mean grain intercepts are in the range of 0.7 to $1.2 \text{ }\mu\text{m}$. No systematic changes in grain size were observed.

2.2.2 Reaction sintered silicon nitride

Table 1 lists the data for the microstructural characterization for the RSSN samples. As indicated by Morgan [21] a number of questions on the nature of the formation of the α - and β -phase in RSSN still remain to be answered. For the method of preparation used for the specimens of this study, the α -phase most probably is formed by a gas-phase reaction between the Si and/or SiO and N_2 , which leads to whisker-shaped crystallites in the form of a matte. At nitriding temperatures below the melting point of Si, the β -phase is formed by a diffusion process of the nitrogen to the Si-Si₃N₄ interface [8, 9]. As indicated by the data in Table 1, the size of the natural pores in sets II and III range from about 0.06 to $0.25 \text{ }\mu\text{m}$ for the micropores and from 7 to $34 \text{ }\mu\text{m}$ for the macropores. The micropores are thought to correspond to the spacings between the very fine fibers in the α -matte [8]. The β -grains were found to be equiaxed ranging in size from about 0.5 to $3 \text{ }\mu\text{m}$. Further microstructural details for these materials were presented in earlier publications [8, 19].

In set I at nearly constant other microstructural parameters only the size of the artificially introduced macropores are changed. In the sets II and III the amount of α -phase decreases from batches A to C, while the diameter of the micro- and macro-pores increase. The change in the $\alpha/\alpha+\beta$ ratio and in the size of micro- and macropores is due to the variation of the grain size of the starting silicon powder and to the corresponding change in size and arrangement of pores in the green body [9]. Figure 4 shows the microstructure of the α -phase for the two specimens A and C of set III, which exhibited large differences in thermal diffusivity for the same density. These micrographs clearly indicate the difference in morphology, in particular the increase in thickness and in contact area between the fibers in batch C.

2.3 Technique for Measuring the Thermal Diffusivity

The thermal diffusivity was measured by the laser-flash technique [11]. Samples of the silicon nitride in the form of thin rectangular or circular plates were flashed on one side by means of a 50 J glass-Nd laser. A liquid N₂ cooled infra-red detector coupled to a storage-oscilloscope was used to monitor and record the transient temperature of the opposite side of the sample. The recorded trace of the temperature as a function of time permitted calculation of the thermal diffusivity [22]. Measurements were made only at room temperature, at which any differences in the thermal diffusivity are expected to be most pronounced without having the resort to specimen cooling and major equipment modifications.

2.4 Elastic Properties, Strength and Fracture Toughness

Frequently for porous materials correlation are found between the amount of pore phase, pore morphology and the thermal and mechanical properties. For this reason, experimental data for the mechanical behavior can assist in the proper interpretation of the thermal property data. For the samples of reaction-sintered silicon nitride of the present study, the elastic properties, fracture stress (determined in 4-point bending tests) and fracture toughness were reported in detail as part of a previous study [19]. The results are shown in Table 2.

3. Experimental Results and Discussion

3.1 Hot-Pressed Silicon Nitride

Figure 5 shows the thermal diffusivity of the silicon nitride with 5% MgO as a function of hot-pressing time. As indicated in Fig. 1, increasing time for hot-pressing results in the transformation of the α - into the β -phase. Comparisons of Fig. 1 and 5 indicate clearly that the thermal diffusivity shows a significant increase with increasing β -content.

Some explanations for this observation can be given. For very short times of hot-pressing ($t_p = 10$ min) the increase can be attributed to an increase in density. For the samples subjected to longer hot-pressing times in which complete densification occurred the increase in thermal diffusivity must be attributed to changes in the relative amounts of the α - and β -phase and to corresponding changes in grain morphology and heat transfer behavior.

It is expected that heat conduction in the α - and β -silicon nitride at room temperature occurs primarily by phonon transport. For this reason, differences in the thermal diffusivity must arise because of differences in the phonon velocity or phonon mean free path. Since the elastic properties and density of α - and β - Si_3N_4 do not differ significantly (as far as the authors are aware) a difference in thermal diffusivity due to differences in phonon velocity seems unlikely. Phonon mean free path differences can be attributed to at least two possible effects. Firstly, differences appear to exist in the crystal structure of the α - and β -modifications.

Henderson and Taylor [23] suggested that the α -phase has a more strained crystal structure than the β -phase. For this reason, phonon scattering is expected to occur to a greater degree in the α -phase than in the β -phase, thereby yielding a lower value for the thermal diffusivity of the former.

A second reason for this increase in thermal diffusivity with increasing β -content may be related to the formation and growth mechanism of the β - Si_3N_4 . Although still a topic of discussion [24], the formation of the β -phase is thought to result from the dissolution of the α -phase in the liquid grain boundary phase and a re-precipitation of the silicon nitride in the β -form [17]. It is likely that the solubility of impurities in the β -phase is lower than in the liquid grain boundary phase. For this reason, it is expected that during the α - to β - transformation an enrichment of the purities in the grain boundary phase occurs, so that the purity of the β -grains is higher than the original α -grains. Impurities or other atoms are well-known

to be effective phonon scatterers [4, 7] so the higher purity of the β -phase is responsible for its higher diffusivity.

The difference in the size, shape and orientation of the β -grains compared to the α -grains should also be examined as possible contributing factors to the observed increase in thermal diffusivity. Since the phonon mean free path in the silicon nitride at room temperature is much smaller than the grain size any effect of the latter appears unlikely. A change in grain shape for randomly oriented grains contained in a matrix, as may be inferred from the analytical results of Bruggeman [25] and Niesel [26] should not lead to a change in thermal diffusivity. However, as shown by Powers [27] from the results of Fricke [28] an elongation of the grains in a preferred orientation will result in an increase or decrease in the direction of heat flow parallel and perpendicular to the direction of preferred orientation, resp., regardless of the relative values of the thermal conductivities of the two phases. However, since the β -grains are elongated perpendicular to the hot-pressing direction [29] and the direction of heat flow, the present observation cannot be attributed to this latter effect. Therefore, it can be concluded that the increase in thermal diffusivity with increasing β -content after complete densification must be because the thermal conductivity/diffusivity of the β -phase is inherently higher than of the α -phase.

Figure 7 shows the data for the thermal diffusivity as a function of MgO content after complete α -to- β transformation. As can be noted, with increasing MgO content, the thermal diffusivity first increases to a maximum followed by a decrease at the highest values of MgO content. The initial increase in thermal diffusivity at low MgO content is thought

to be due primarily to a reduction of residual porosity with increasing MgO content. Maximum thermal diffusivity is reached at about 3% MgO. This MgO-content is commonly used in practice to achieve optimum mechanical behavior. The decrease in thermal diffusivity with higher MgO content most likely can be attributed to the increasing amount of glassy grain boundary phase. Glassy materials generally have values of thermal conductivity or diffusivity some order of magnitude less than crystalline solids. For high MgO contents the higher amount of magnesium silicates is expected to be particularly effective in controlling the overall rate of heat transfer through hot-pressed $\text{MgO-Si}_3\text{N}_4$.

3.2 Reaction-Sintered Silicon Nitride

Table 2 lists the experimental data for the thermal diffusivity, elastic properties, strength and fracture toughness for all specimens sets I, II, III. Comparisons with the microstructural and compositional data in Table 1 leads to the following correlations and conclusions:

The data for the specimens for set I, which were prepared to ascertain the effect of macropore size on thermal mechanical properties near constant other microstructural variables showed that no such pore size effect exists for the thermal diffusivity and Young's modulus, in agreement with theory [30]. The decrease in strength with increasing macro-pore size is in accordance with theoretical considerations based on pore size to flow size ratios [31, 32].

The data for the specimens in sets II and III indicate a pronounced negative correlation between the thermal diffusivity and $\alpha/\alpha+\beta$ ratio and a positive correlation with the size of the micro- and macro-pores. As indicated by the data for set I, this variation in thermal diffusivity cannot be attributed to the variation in size of the macro-

pores. The negative correlation between the strength and the size of the macropores is to be expected from pore size to flow size considerations, referred to earlier.

Particularly noteworthy for the data for sets II and III is the strong negative correlation between the thermal diffusivity and the strength at nearly constant Young's modulus.

The above observations and correlations are not in general agreement with the behavior of single-phase brittle structural materials. For these, with decreasing density, strength shows the greatest relative decrease followed by Young's modulus, thermal conductivity and thermal diffusivity in accordance with theoretical predictions [33-37]. Also, in the absence of radiation heat transfer, thermal conductivity and diffusivity should be unaffected by pore size.

An answer to these observations must be found in the unique microstructure of reaction sintered silicon nitride. Fibrous microstructures, due to the long path-length for phonon heat transfer will exhibit a much lower thermal conductivity [38] than a matrix with the same relative density containing isolated equi-dimensional pores. For this reason, the thermal conductivity/diffusivity of RSSN is expected to decrease with increasing α -content. Furthermore, differences in fiber morphology for a given α -content are expected to affect the thermal diffusivity as well. Generally, the smaller the thickness and inter-spacing of the fibers for constant bulk-density the lower will be the thermal conductivity, in part due to increase phonon scattering at the fiber surfaces, reduced contact areas between the fibers and reduction in heat transport by the gaseous phase and radiation within the pores. For this reason, the observed variations in the thermal diffusivity for

present RSSN samples are due primarily to differences in morphology and the relative amount of the α -phase. This effect is enhanced further because as stated earlier, the lower thermal diffusivity of the α -phase compared to the β -phase is thought to be due to the more distorted crystal structure of the former.

The inverse correlation between strength and thermal diffusivity at near constant Young's modulus, particularly noticable for the specimens of set II, probably also can be attributed to the amount and size of the α -fibers. An increase in fiber amount is expected to improve the fracture toughness, as observed, which improves strength.

The free Si-content does not seem to have a pronounced effect on the thermal diffusivity, possibly because its relatively small amount.

3.3 General

It should be noted that although for both the hot-pressed and reaction-sintered silicon nitride, the thermal diffusivity increases with increasing β -content; these effects occur for different reasons. For the hot-pressed silicon nitride, the more perfect crystal structure and the higher purity of the β -phase leads to the increase in the thermal diffusivity. In the reaction-sintered silicon nitride, however, the fibrous morphology and amount of the more strained α -silicon nitride appears to be the deciding factor in establishing the value of the thermal diffusivity.

The results of the present study suggest that by careful process modifications, a measure of control can be exerted over the heat conduction properties of silicon nitride. For high thermal stress resistance which requires high thermal conductivity the relative amount of the β -phase should be maximized. For reaction-sintered silicon nitride, however,

this latter approach involves an undesirable trade-off with a decreasing strength. On the other hand, for engine components which require low thermal conductivity in order to maintain high engine efficiency because of reduced heat losses, the relative α -content should be kept as high as possible for both the hot-pressed as well as the reaction-sintered silicon nitride.

Acknowledgments

This study was supported in part by the Deutsche Forschungsgemeinschaft (D-5300 Bonn-Bad Godesberg, Kennedyallee 40) for Dr. Ziegler's stay at V.P.I. and S.U. as a Visiting Scientist, in part by the DFVLR and by the Office of Naval Research as a part of a larger programme on the thermo-mechanical and thermal properties of structural ceramics under contract: N 00014-78-C-0431.

Table 1. Microstructural and Compositional Characteristics
of Reaction Sintered Si_3N_4

Specimen Set and Number	Density gm/cc	Degree of Reaction (%)	$\frac{\alpha}{\alpha+\beta}$	Pore Size (μm)		Si Content wt. %
				Micro	Macro*	
ID1	2.39	92.8	0.71	0.137	48**	1-2
ID2	2.39	92.5	0.73	0.129	66	1-2
ID3	2.41	90.1	0.64	0.097	100	1-2
IIA	2.25	97.3	0.78	0.130	8	3-5
IIB	2.17	96.8	0.75	0.240	22	3-5
IIC	2.23	96.8	0.66	0.250	34	3-5
IIIA	2.41	89.9	0.82	0.058	7	1-3
IIIB	2.42	91.0	0.70	0.108	19	1-3
IIIC	2.38	93.0	0.60	0.152	28	1-3

* Mean pore size (50%) from cumulative pore size distribution

** Arithmetic mean value of artificial pores

Table 2. Thermal Diffusivity, Tensile Strength, Elastic Properties and Fracture Toughness of Reaction Sintered Si_3N_4

Specimen Set and Number	Thermal Diffusivity $\text{cm}^2 \text{ s}^{-1}$	Tensile Strength MNm^{-2}	Young's Modulus $\text{MNm}^{-2} \times 10^{-3}$	Poisson's Ratio	Fracture Toughness $\text{MNm}^{-3/2}$
ID1	0.099	140	161	0.22	1.87
ID2	0.101	119	167	0.23	1.81
ID3	0.098	101	165	0.24	1.93
IIA	0.058	205	139	0.20	2.5
IIB	0.083	139	127	0.23	2.08
IIC	0.100	124	133	0.24	2.0
IIIA	0.060	150	171	0.23	2.80
IIIB	0.084	164	160	0.22	2.68
IIIC	0.109	127	154	0.24	2.14

References

- [1] R. Berman: Thermal Conductivity in Solids, Clarendon Press - Oxford (1976).
- [2] H. J. Siebeneck, W. P. Minnear, R. C. Bradt and D. P. H. Hasselman: J. Am. Ceram. Soc. 59 (1976) 84.
- [3] K. Chyung, G. E. Youngblood and D. P. H. Hasselman: J. Am. Ceram. Soc. 61 (1978) 590.
- [4] W. D. Kingery, H. K. Bowen and D. R. Uhlmann: Introduction to Ceramics, 2nd Ed. John Wiley, N.Y. (1975).
- [5] H. J. Siebeneck, D. P. H. Hasselman, J. J. Cleveland and R. C. Bradt: J. Am. Ceram. Soc. 58 (1976) 241.
- [6] D. P. H. Hasselman: J. Comp. Mat. 12 (1978) 403.
- [7] J. E. Matta and D. P. H. Hasselman: J. Am. Ceram. Soc. 58 (1975) 458.
- [8] J. Heinrich and G. Streb: J. Mater. Sci. 14 (1979) 2083.
- [9] J. Heinrich, DFVLR-Report FB 79-32, DFVLR, 5000 Cologne 90, FRG.
- [10] W. George: Proc. Brit. Ceram. Soc. 22 (1973) 147.
- [11] F. F. Lange, H. J. Siebeneck and D. P. H. Hasselman: J. Am. Ceram. Soc. 59 (1976) 454.
- [12] T. Hirai, S. Hayashi and K. Niihara: Am. Ceram. Soc. Bull. 57 (1978) 1126.
- [13] M. Kuriyama, Y. Inomata, T. Kujima and Y. Hasegawa: Am. Ceram. Soc. Bull. 57 (1978) 1119.
- [14] R. J. Lumby, B. North and A. J. Taylor, pp. 893-906 in Ceramics for High Performance Application - II, J. J. Burke, E. N. Lenoë and R. N. Katz, eds. Brook Hill Publishing Comp., Chestnut Hill, Mass. (1978).

- [15] H. Knoch and G. Ziegler: Science of Ceramics (1977) 494.
- [16] H. Knoch and G. Ziegler: Ber. Dt. Keram. Ges. 55 (1978) 4, 242.
- [17] H. Knoch and G. E. Gazza, Ceramurgia International (in press).
- [18] G. Ziegler and H. Knoch: (in preparation).
- [19] G. Ziegler and J. Heinrich: Ceramurgia International (in press).
- [20] J. Heinrich, D. Munz and G. Ziegler: (in preparation)
- [21] P. E. D. Morgan: J. Mater. Sci. 15 (1980) 791.
- [22] W. J. Parker, R. J. Jenkins, C. P. Butler and G. L. Abott:
J. Appl. Phys., 32 (1961) 1697.
- [23] C. M. B. Henderson and D. Taylor: Trans. J. Brit. Ceram. Soc.,
2 (1975) 49.
- [24] H. M. Jennings, S. C. Danforth and M. H. Richmand: J. Mat. Sci.,
14 (1979) 1013.
- [25] D. A. G. Bruggeman: Ann. Physik, 24 (1935) 636.
- [26] W. Niesel: Ann. Physik, 10 (1952) 336.
- [27] A. E. Powers: Conductivity in Aggregates, Knolls Atomic Power
Laboratory Report KAPL-2145, March 1961.
- [28] H. Fricke: Phys. Rev. 24 (1924) 575.
- [29] F. Lange: J. Am. Ceram. Soc., 57 (1974) 84; 56, (1973) 518.
- [30] Z. Hashin: J. Appl. Mech. 29 (1962) 143.
- [31] O. L. Bowie, J. Math. Phys. 35 (1956) 60.
- [32] F. Erdogan: in Fracture Mechanics of Ceramics, Vol. 1, ed. by R. C.
Bradt, D. P. H. Hasselman and F. F. Lange, Plenum Press, N.Y. 1974.
- [33] R. M. Spriggs: J. Amer. Ceram. Soc. 44 (1961) 628.
- [34] D. P. H. Hasselman: J. Am. Ceram. Soc. 45 (1962) 452.
- [35] L. Rayleigh: Phil. Mag. 34 (1892) 48.

- [36] J. C. Maxwell: A Treatise on Electricity and Magnetism, 3rd Ed.
Oxford Univ. Press (1904).
- [37] E. H. Kerner: Proc. Phys. Soc. (London) B 69 (1956) 802.
- [38] H. J. Siebeneck, R. A. Penty, D. P. H. Hasselman and G. E. Young-
blood: Amer. Ceram. Soc. Bull 56 (1977) 572.

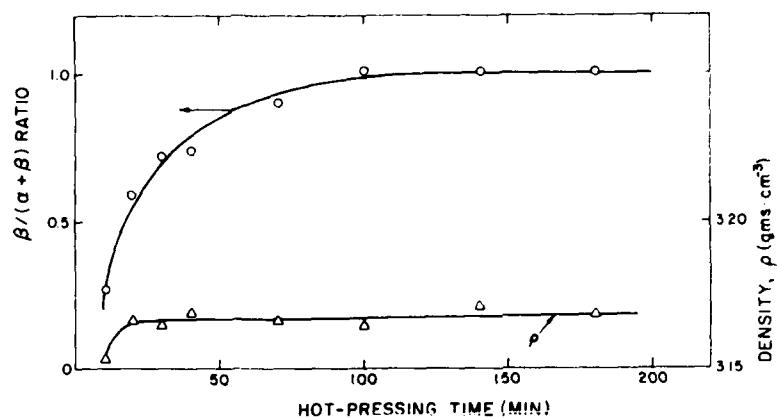


Fig. 1. Effect of hot-pressing time at 1973°K on $\beta/(\alpha+\beta)$ ratio and density of hot pressed silicon nitride with 5 wt.% MgO.

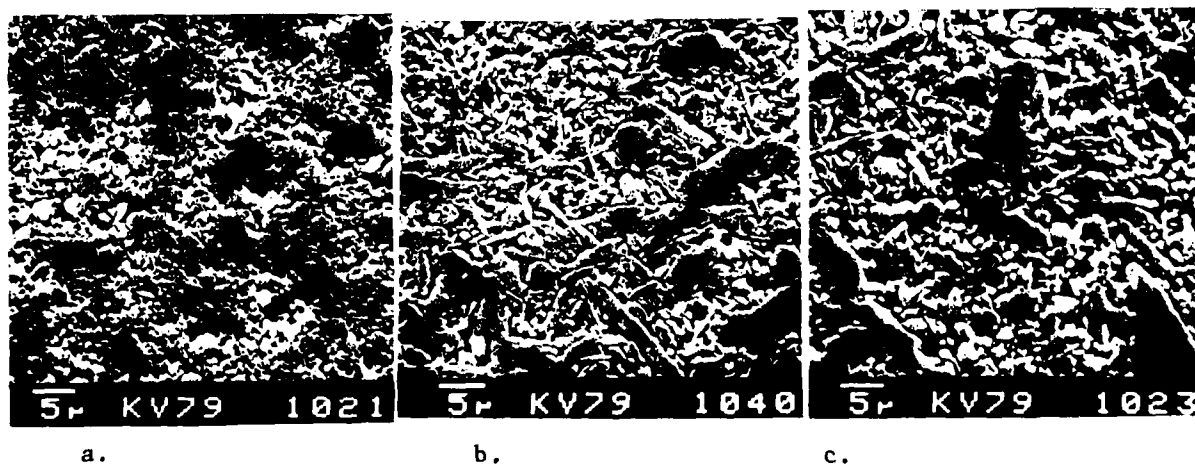


Fig. 2. Change in grain morphology with increasing $\beta/(\alpha+\beta)$ ratio in silicon nitride with 5 wt.% MgO hot pressed at 1973K for: a, 10 min; b, 40 min and c, 100 min.

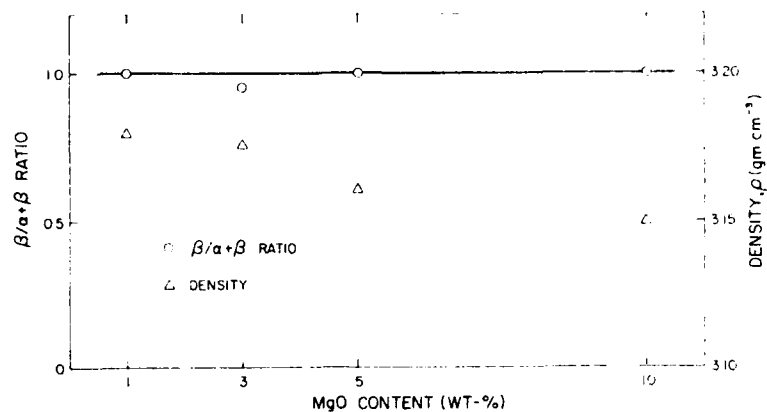


Fig. 3. Density of hot pressed silicon nitride of set II as a function of MgO content for hot pressing times required to result in $\beta/\alpha+\beta$ ratio equal to unity.

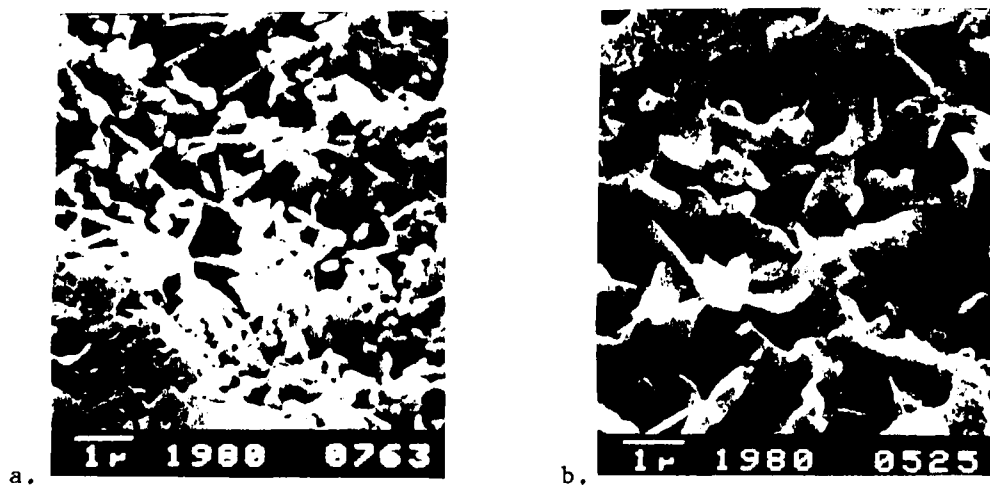


Fig. 4. Microstructures of α -matte in reaction-sintered silicon nitride of set III with large differences in room temperature thermal diffusivity, a: 0.06 cm².s and b: 0.11 cm².sec.

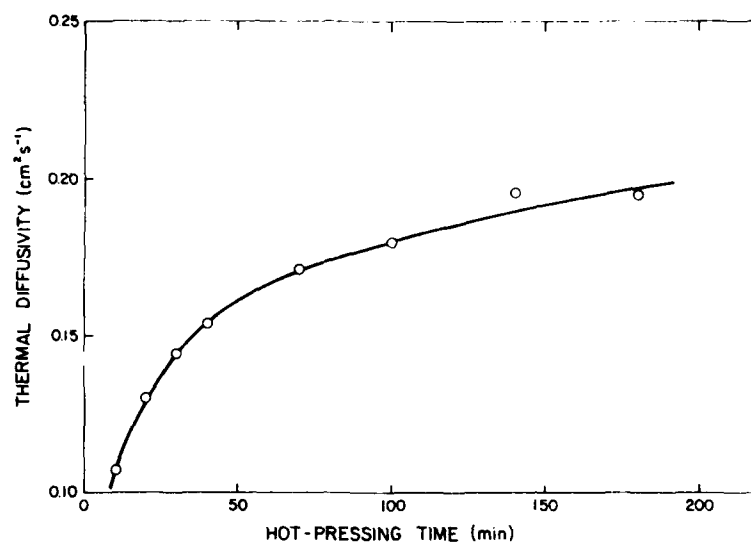


Fig. 5. Thermal diffusivity at room temperature of hot-pressed silicon nitride with 5% MgO (set I) as a function of hot-pressing time at 1973°K.

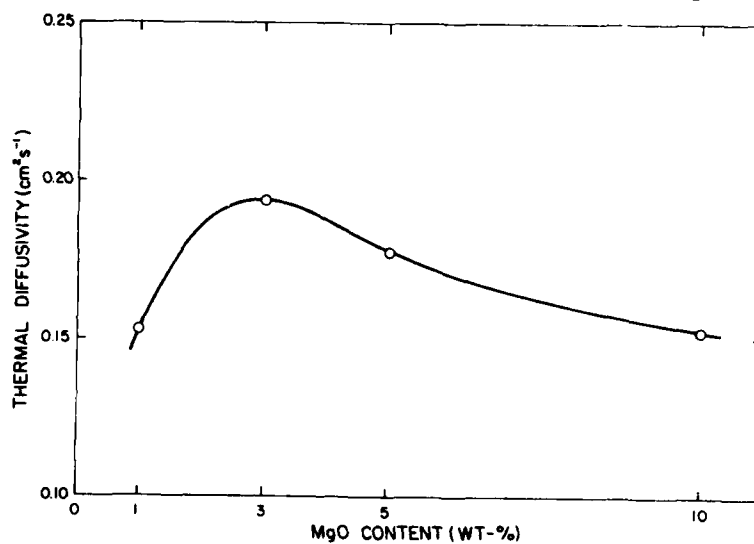


Fig. 6. Thermal diffusivity at room temperature of silicon nitride hot-pressed at 2053°K (set II) with $\beta/\alpha + \beta = 1$ as a function of MgO content.

CHAPTER IV

ORIENTATION EFFECTS ON THE THERMAL
DIFFUSIVITY OF HOT-PRESSED SILICON NITRIDE

by

G. Ziegler^{*}, L. D. Bentsen[†], D. P. H. Hasselman[†]

^{*}Institut fuer Werkstoff-Forschung
DFVLR, Cologne
Federal Republic of Germany

[†]Department of Materials Engineering
Virginia Polytechnic Institute and
State University
Blacksburg, Virginia 24061, USA

The hot-pressing of silicon nitride requires a densification aid such as magnesium oxide. During hot-pressing the grains of the silicon nitride in the α -modification are transformed gradually into elongated grains of the β -modification most probably by a dissolution and re-precipitation process. The β -grains exhibit a preferred orientation such that their direction of elongation, which coincides with the crystallographic c-axis, is oriented perpendicularly to the hot-pressing direction¹⁻⁴. This preferred orientation has been shown to result in a pronounced anisotropy in strength at high temperature as well as fracture toughness. Recent results⁵ indicate that the α -to- β transformation resulted in a significant increase in the room temperature thermal diffusivity of hot-pressed silicon nitride in a direction parallel to the hot-pressing direction. It was suggested that this latter effect arose because the thermal conductivity of the β -phase was higher than for the α -phase.

Theoretical solutions of Powers⁶ based on the original theory of Fricke⁷, for the thermal conductivity of composites consisting of matrices with oriented elongated dispersions in the shape of prolate ellipsoids of revolution indicate that the thermal conductivity of the composite would be a maximum in the direction of elongation. This effect would occur regardless whether the matrix or dispersions had the higher thermal conductivity. At least qualitatively this result is expected to occur for hot-pressed silicon nitride, due to the elongation of the β -grains, perpendicular to the hot-pressing direction. For this reason, the thermal conductivity and diffusivity perpendicular to the hot-pressing direction would be expected to be higher than the corresponding values parallel to

the hot-pressing direction. The purpose of this communication is to present experimental data in support of this conclusion.

For this purpose specimens were cut from disks approximately 70 mm wide by 6 mm thick prepared by vacuum hot-pressing in graphite dies at a pressure of $35 \text{ MN} \cdot \text{m}^{-2}$ for previous studies⁵ on the effect of micro-structure, composition on mechanical properties and thermal diffusivity⁵ measured parallel to the hot-pressing direction. For the specimens, the processing parameters, MgO content, density and $\beta/\alpha+\beta$ ratio are listed in Table 1. The aspect ratio of the β -grains was about 5. Additional discs containing 10 wt.% MgO were hot-pressed as well for a range of time periods as listed in Table 1. Specimens for the measurement of the thermal diffusivity in the form of plates approximately 5 mm square by 2 mm thick were cut from larger specimens used for measurements of bend strength. Most specimens for thermal diffusivity were cut from the same strength specimens in order to minimize possible effects of non-uniformity in density or composition within the hot-pressed disks.

The thermal diffusivity was measured by the laser-flash technique⁹ using equipment described elsewhere¹⁰. The transient temperature of the specimen during the measurement was monitored by a liquid N_2 cooled IR-detector. Data were obtained at room temperature at which any directional effects on the thermal diffusivity would be expected to be a maximum without cooling the specimens below room temperature.

The experimental data are shown in Figs. 1, 2 and 3. Comparison shows that for all compositions and heat treatments the thermal diffusivity perpendicular to the hot-pressing direction

exceeds the corresponding value parallel to the hot-pressing direction, in agreement with the above hypothesis. The observation that the thermal diffusivity increases with increasing β -amount for both directions relative to the hot-pressing direction is confirmation that the thermal conductivity/diffusivity of the β -phase is significantly higher than that of the α -phase. This was attributed⁵ to the fact that the crystal structure of the α -phase is a more distorted structure with shorter phonon mean free path than the β -structure and probably also to impurity segregation in the grain boundary phase so that the β -grains have lower impurity content than the original α -phase. The maximum in the thermal diffusivity as a function of MgO content probably occurs because once complete densification near 3 wt.% MgO is achieved, further additions of MgO result in a lowering of the thermal diffusivity as the result of the lower value of the glassy grain-boundary phase. The slight increase in the thermal diffusivity with increasing hot-pressing time for 10% MgO content possibly is due to an increase in crystalline order. X-ray studies of this effect were not positive, possible as the result of the low thickness of the grain boundary phase ($< 100 \text{ \AA}$).

In general, the present results indicate that even at a single temperature, the heat transport properties of hot-pressed silicon nitride are subject to a number of simultaneous variables including the effect of composition, microstructure, processing, purity, as well as orientation. For purposes of practical application of silicon nitride it is imperative that such effects are well understood.

Acknowledgments

Specimen preparation was carried out at the DFVLR, Cologne, Germany as part of a research program supported by the Deutsche Forschungsgemeinschaft (D-5300 Bonn-Bad Godesberg, Kennedyallee 40). The measurement of the thermal diffusivity was performed in the Thermophysical Properties Laboratory in the Department of Materials Engineering at Virginia Polytechnic Institute and State University as part of a research program supported by the Office of Naval Research under Contract N00014-78-C-0431.

References:

1. Ram Kossowsky, "The Microstructure of Hot-Pressed Silicon-Nitride," J. Mat. Sc. 8, 1603-15 (1973).
2. F. F. Lange, "Relation Between Strength, Fracture Energy, and Microstructure of Hot-Pressed Si_3N_4 ," J. Amer. Ceram. Soc. 56 [10] 518-22 (1973).
3. K. Nuttall and D. P. Thompson, "Observations on the Microstructure of Hot-pressed Silicon Nitride," J. of Mat. Sc. 9, 850-53 (1973).
4. F. F. Lange, "High-Temperature Strength Behavior of Hot-Pressed Si_3N_4 : Evidence for Subcritical Crack Growth," J. Amer. Ceram. Soc., 57 [2] 84-87 (1979).
5. G. Ziegler and D. P. H. Hasselman, "Effect of Phase Composition and Microstructure on the Thermal Diffusivity of Silicon Nitride," J. Mat. Sc. (in review).
6. A. E. Powers, Conductivity in Aggregates, Knolls Atomic Power Laboratory, General Electric Company, Schenectary, N.Y. (1961)
7. H. Fricke, "The Electrical Conductivity of a Suspension of Homogeneous Spheroids," Phys. Rev., 24, 575-87 (1924).
8. G. Ziegler and H. Knoch, "Influence of Microstructure on the Thermal Shock Resistance of Hot-pressed Silicon Nitride," Ceramurgia International (in press).
9. W. J. Parker, R. J. Jenkins, C. P. Butler and G. L. Abbott, "Flash Method of Determining Thermal Diffusivity, Heat Capacity and Thermal Conductivity," J. Appl. Phys., 32 [9] 1679-84 (1961).
10. H. J. Siebeneck, J. J. Cleveland, D. P. H. Hasselman and R. C. Bradt, "Effect of Microcracking on the Thermal Diffusivity of Fe_2TiO_5 ," J. Amer. Ceram. Soc., 59 [5-6] 241-44 (1976).

1. COMPOSITION, PROCESSING CONDITIONS AND DENSITY OF HOT-PRESSED SILICON NITRIDE

Amount pressed (g.)	Processing Conditions °C;Min	Density (g.cc-1)	$\frac{\beta}{\alpha+\beta}$
5	1700;10	3.15	0.26
5	1700;40	3.17	0.73
5	1700;100	3.17	1
5	1700;180	3.17	1
1	1780;180	3.18	1
3	1780;120	3.17	0.95
5	1780;50	3.16	1
10	1780;30	3.15	1
10	1700;70	3.18	1
10	1700;100	3.15	1
10	1700;150	3.16	1
10	1700;200	3.16	1
10	1700;400	3.16	1

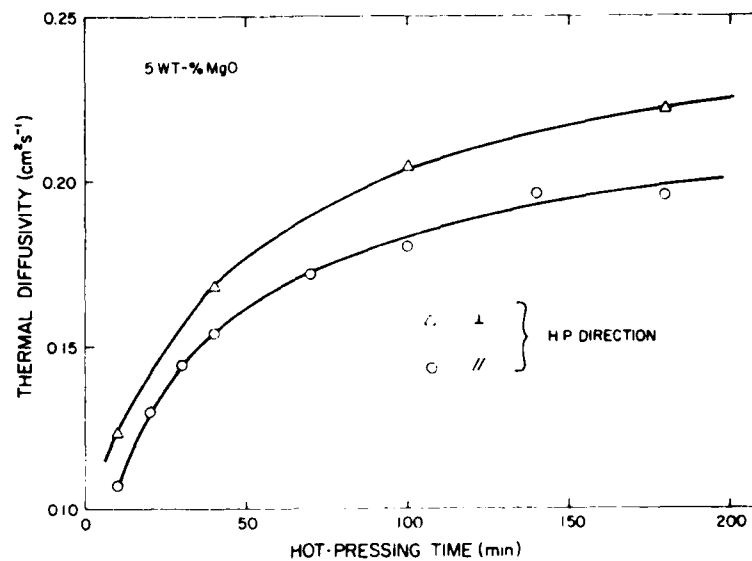


Fig. 1. Effect of hot-pressing direction on the thermal diffusivity of silicon nitride subjected to various hot-pressing time to increase β -fraction.

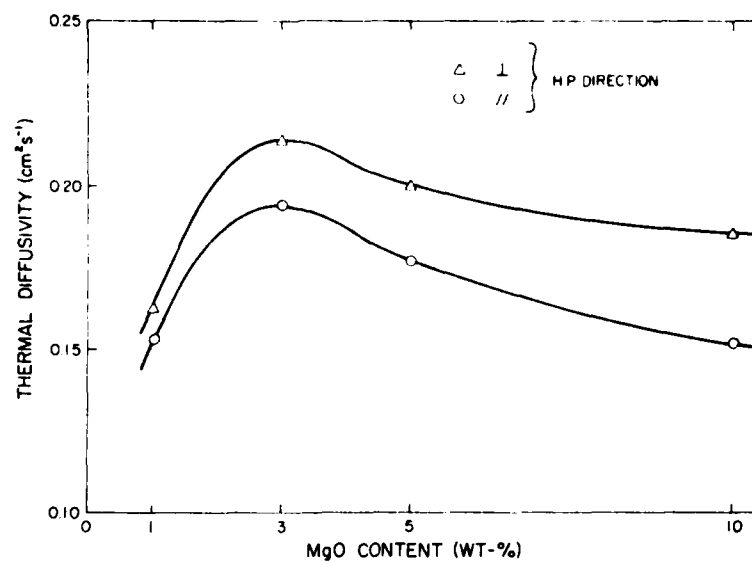


Fig. 2. Effect of hot-pressing direction on the thermal diffusivity of silicon nitride with a range of MgO content for $\rho/\alpha+\beta$ ratio near unity.

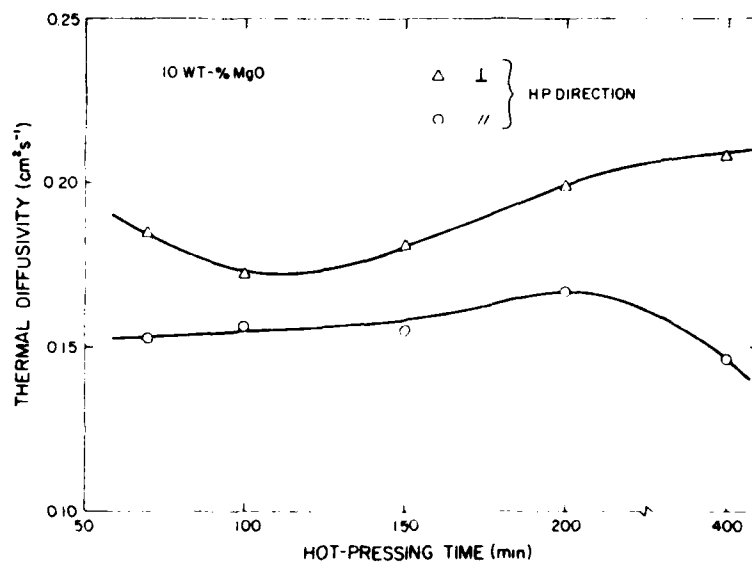


Fig. 3. Effect of hot-pressing direction on the thermal diffusivity of silicon nitride with 10 wt.% MgO and $\beta/\alpha+\beta = 1$ as a function of hot-pressing time.

CHAPTER V

OBSERVATIONS ON THE SUB-CRITICAL GROWTH AND HEALING OF MICRO- CRACKS IN BRITTLE CERAMICS

K. Niihara, J.P. Singh, L.D. Bentsen and D.P.H. Hasselman

Department of Materials Engineering
Virginia Polytechnic Institute and State University
Blacksburg, Virginia 24061

ABSTRACT

Micro-cracking in brittle composites was monitored by measuring the temperature dependence of thermal diffusivity by the laser flash method. Depending upon the material system, micro-cracks can exhibit a time dependent growth or healing or a combination of both. A theoretical basis for these observations was established by analyzing the stability and nature of crack propagation of precursor micro-cracks in a spherical inclusion contained in an infinite matrix with different elastic properties.

INTRODUCTION

Microcracked materials, in view of their potential for high fracture toughness¹, high thermal shock resistance² and low thermal conductivity³, are of considerable technical interest. Optimization of these properties requires a detailed understanding of the variables which control the formation of microcracks.

Micro-cracking is observed in composites with large mismatches in the coefficients of thermal expansion of the components. Extensive micro-cracking can also occur in polycrystalline aggregates with high thermal expansion anisotropy of the individual grains. Micro-cracking occurs due to the internal stresses which arise from the non-uniform thermal expansion whenever the material is subjected to a temperature change from the value at which the material is stress-free. This latter temperature usually is the fabrication temperature. For linearly elastic materials the magnitude of the internal stresses is a function of the thermal expansion differ-

ences, the range of temperature change and the elastic properties of the components⁴ or the polycrystalline array. The magnitude of the internal stresses can also be affected by stress relaxation phenomena as governed by the kinetics of available creep mechanisms and the time period over which such relaxation is permitted to occur.

Microcracking is also strongly dependent on grain size¹, in spite of the fact that the magnitude of the internal stresses is independent of the scale of the microstructure. This observation has led to the development of a theory of microcrack formation based on the criterion that microcracking will occur only for grains of sufficient size such that the elastic energy of the residual stress field equals the surface energy required to create a crack equal to the grain size⁵. This hypothesis does not define the conditions for the onset of microcrack formation.

More recently, the conditions for the formation of micro-cracks have been defined in terms of the size and geometry of micro-crack precursors in the form of crack-like residual pores at triple points and grain boundaries⁶. From these precursors, microcracks will form when the stress intensity factor exceeds the critical stress intensity factor. Since the size of such precursors frequently is proportional to the grain size, an indirect grain size effect is expected.

The variables which control microcracking can be studied by the measurement of those material properties which are affected by microcracks. These include strength, fracture toughness, elastic behavior and thermal conductivity or diffusivity. These latter two properties are preferred since their measurement does not involve the application of a mechanical load, which could affect crack stability.

For a material with randomly oriented, equal sized, penny-shaped cracks, the thermal conductivity (K) in the absence of heat transfer across the cracks is³:

$$K = K_0 [1 + 8N\ell^3/9]^{-1} \quad (1)$$

where K_0 is the thermal conductivity of the crack-free material, N is the number of cracks per unit volume and ℓ is the radius of the cracks. Since microcracking has negligible effect on the specific heat per unit volume, eq. 1 also describes the effect of micro-cracking on the thermal diffusivity.

Equation 1 indicates that any changes in the thermal conductivity or diffusivity can be attributed to changes in the crack density or crack size or combinations thereof. For this reason, measurements of the thermal diffusivity of microcracked material

can provide information on the variables which control microcrack stability and propagation behavior. The purpose of this paper is to present a number of such experimental data. These will be interpreted qualitatively first, followed by a quantitative analysis.

EXPERIMENTAL

The experimental data for the thermal diffusivity to be presented for a number of different materials include recent observations as well as data obtained in a number of previous studies. These latter studies contain descriptions of the equipment and procedures of the laser-flash diffusivity method used for these measurements as well as details on material fabrication and microstructures.

Figure 1 shows the thermal diffusivity⁷ as a function of temperature for a coarse-grained polycrystalline iron-titanate. Because of its relatively low values of thermal diffusivity compared to a fine-grained iron-titanate, the material of fig. 1 must have undergone extensive micro-cracking as it was cooled from the annealing temperature prior to the measurement of the thermal diffusivity. It is significant to the objectives of the present study that the thermal diffusivity displays a significant hysteresis in such a manner that the thermal diffusivity on cooling considerably exceeds the corresponding values obtained during heating. To provide an explanation for this behavior it should be noted that on heating the material the differential thermal strains responsible for the microcracking are reduced or even eliminated. At sufficiently high temperature the excess surface energy of the microcracks can be reduced by material transport by diffusional processes. This leads to crack-healing i.e., a decrease in crack size and possible crack density and a corresponding increase in the thermal diffusivity.

Figure 2 shows the thermal diffusivity of a fine-grained magnesium dititanate also subjected to a single heating and cooling cycle. In contrast to the behavior noted in fig. 1, these data show that the thermal diffusivity on cooling has values below those found on the heating part of the cycle. This suggests that during the thermal cycle an increase in crack density and/or crack size occurred.

It is critical to note that these data suggest that the microcracks formed during cooling from the fabrication or annealing temperature are not necessarily in an equilibrium condition. As an explanation for the data of fig. 2 it is suggested that during the first cooling, the precursor microcracks were not of sufficient size that they could lead to microcrack formation at room temperature. On reheating the specimens, however, they could grow

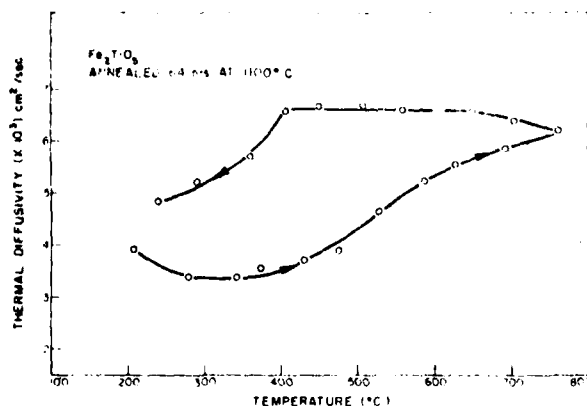


Fig. 1. Thermal diffusivity of thermally cycled coarse-grained iron-titanate.

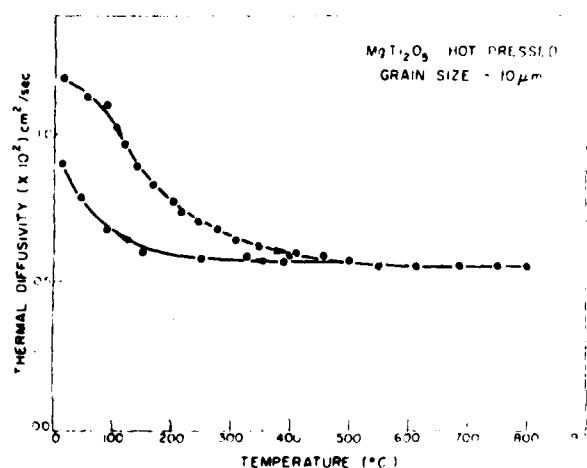


Fig. 2. Thermal diffusivity of thermally cycled fine grained magnesium dititanate.

subcritically to a large enough size, such that on cooling to room temperature, criticality was reached and microcracks formed.

Figure 3 shows the thermal diffusivity for magnesium dititanate⁸, which indicates a combination of the behavior noted for figs. 1 and 2. At high temperatures the expected crack healing occurs but on cooling to room temperature the values for the thermal diffusivity fall below the values at the beginning of the thermal cycle. This behavior is attributed to the existence of a relatively large size distribution of the microcrack precursors. During cooling from the annealing temperature those precursors which were large enough led to the formation of microcracks. However, the precursors which were not of sufficient size, required a second reheat for them to grow, which then led to additional microcracking during the second cooling, i.e., the cooling part of the thermal cycle for the measurement of the thermal diffusivity. Again, as

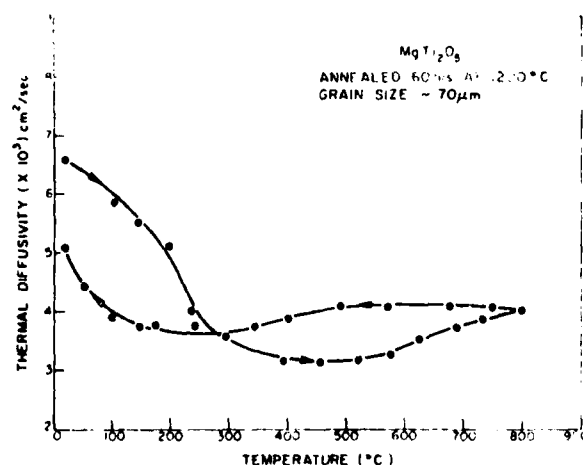


Fig. 3. Thermal diffusivity of thermally cycled coarse-grained magnesium dititanate exhibiting both crack healing and growth.

stated earlier, microcrack configurations developed during a single cycle may not represent an equilibrium. In general, the number and size of the microcracks and their effect on material properties are a function of the thermal history of the material. Furthermore, theoretical assessments of microcracking should include various statistical aspects of microcrack-precursors including not only their size, but also their orientation and geometry.

Further support for the above conclusions is given in figs. 4a and 4b, which show the thermal diffusivity of composites of magnesium oxide containing 20 wt.% SiC cycled to 1300°C and 1400°C, respectively. Both these figures show qualitatively similar behavior to that shown in fig. 3. However, the specimen cycled to 1400°C shows a thermal diffusivity on cooling which is higher than for the specimen cycled to 1300°C. These differences can be attributed to the differences in the temperature dependence of the processes for microcrack healing and precursor growth. At 1300°C, the internal stresses will be higher than at 1400°C. For this reason, at the lower temperature the material will exhibit a higher tendency for precursor growth than at the higher temperature. The opposite effect will exist for crack-healing, which is more likely to occur at 1400°C than at 1300°C. For these reasons, heating to 1400°C is expected to show a greater improvement in thermal diffusivity on cooling than heating to 1300°C, in agreement with the observations. This effect is further evidenced by the diffusivity data for MgO + 20 wt.% SiC composites which showed an 8.1%, 11.3%, and 15.4% decrease in room temperature thermal diffusivity values for specimens thermally cycled to 1300°C and held for 0, 3, and 10 hours respectively.

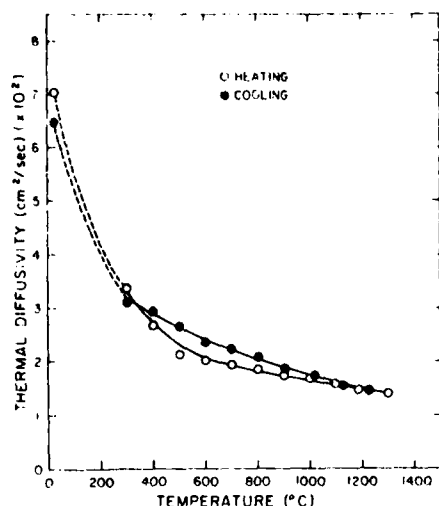


Fig. 4a. Thermal diffusivity of magnesium oxide with 20 wt.% silicon carbide thermally cycled to 1300°C.

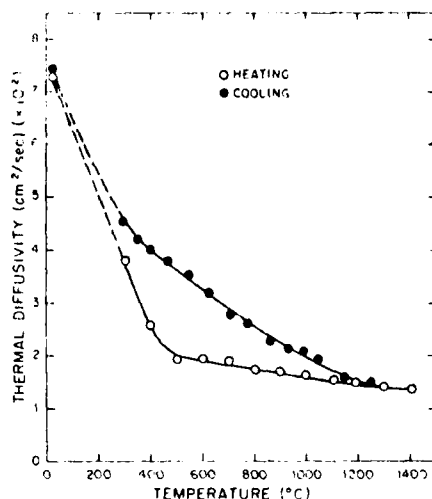


Fig. 4b. Thermal diffusivity of magnesium oxide with 20 wt.% silicon carbide thermally cycled to 1400°C.

Similar effects are indicated in fig. 5, which shows the values for the thermal diffusivity at room temperature before and after thermal cycling of SiC-MgO composites as a function of SiC content. The decrease in the thermal diffusivity after thermal cycling for all compositions is evidence for the growth and/or formation of additional cracks. It is of interest to note that a minimum in the thermal diffusivity occurs at about 20 wt.% SiC. This implies that at this composition microcracking is most extensive. At first sight, it may be expected that the number of microcracks should be proportional to the amount of silicon carbide, with a corresponding monotonic decrease in the thermal diffusivity. The fact that this is not observed is thought to be related, as described in greater detail elsewhere⁹, to the change in phase distribution. At low SiC contents, the silicon carbide represents a discontinuous dispersed phase. At the higher SiC contents, however, particle-to-particle contact will occur so that both the SiC and MgO become continuous phases. This will have a major effect on the magnitude and distribution of the internal stress field, which can have a profound effect on the onset of microcracks due to orientation effects of the precursors, as well the ability of the composite to undergo internal stress relaxation.

Evidence of the stability of microcracks controlled by still another phenomenon is given in fig. 6, which shows the thermal diffusivity of a relatively fine-grained iron-titanate subjected to

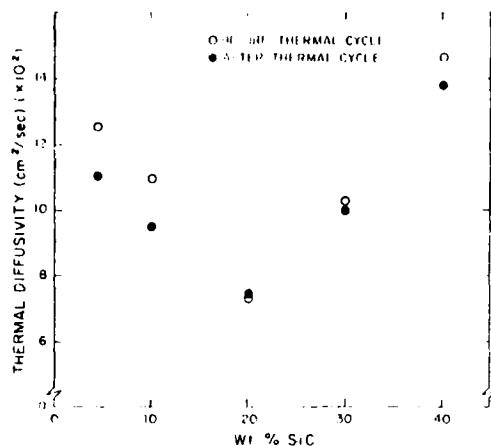


Fig. 5. Effect of thermal cycle to 1400°C on room temperature thermal diffusivity of MgO-SiC composites.

repeated thermal cycles⁷. These data indicate that repeated thermal cycling leads to permanent recovery of the thermal diffusivity. This indicates that following the first cooling from the manufacturing or annealing temperature, microcracks exhibit maximum dimensions, which are permanently decreased following subsequent heat treatments. This effect is expected for micro-cracks formed from relatively small precursors. In analogy to crack formation under conditions of thermal shock¹⁰ these cracks can form by unstable propagation to reach a size such that they are subcritical with respect to the temperature condition required for their creation.

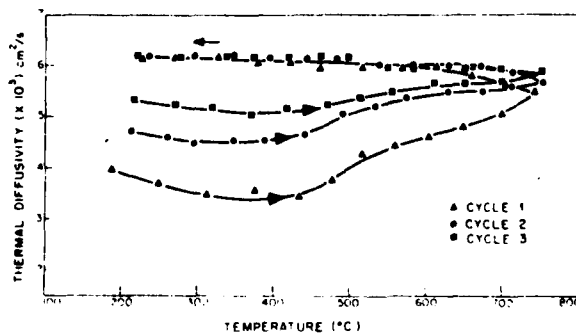


Fig. 6. Effect of temperature and thermal cycling on the thermal diffusivity of polycrystalline Fe_2TiO_5 annealed for 4 hrs. at 1100°.

Such cracks should exhibit permanent healing especially if partially healed, so that on subsequent cycles repropagation occurs in a stable mode only.

The collective evidence of these experimental data is clearly indicative of the non-equilibrium nature of microcracks. In particular, their size and number can be strongly influenced by subcritical growth and healing effects. A quantitative basis for these effects can be provided by a simple analysis of microcrack stability and propagation behavior.

ANALYSIS

The mechanical model chosen for the analysis consists of a single isotropic inclusion contained within an infinite isotropic matrix. Microcracking is assumed to occur within the inclusion. Since the stress (strain) state within the inclusion is uniform, by treating the relevant properties of the inclusion with cracks as pseudo-continuum properties, analytical solutions are easily obtained. Estimates of micro-crack formation at the interface or within the matrix where the stress state is non-uniform require numerical methods. However, the analytical results to be obtained for microcracking within the inclusion, also qualitatively describe behavior of microcracking at the interface or within the matrix.

The analysis, similar to the one by Griffith, is based on the hypothesis that micro-cracks will be unstable if for propagation the decrease in the elastic energy of the internal stress field associated with the inclusion equals or exceeds the corresponding increase in surface energy. In contrast to the Griffith theory, this analysis assumes the existence of two surface energy levels. The first one corresponds to the minimum energy level required for subcritical crack growth. The second (higher) one corresponds to the value of surface energy required for fast fracture.

For an isostatic stress σ in the inclusion, the total elastic energy (W) within the inclusion and matrix is¹¹:

$$W = 2\pi\sigma^2(1-2\nu_p)R^3/E_p + \pi\sigma^2(1+\nu_m)R^3/E_m \quad (2)$$

where ν is Poisson's ratio, E is Young's modulus, R is the inclusion radius and p and m refer to the inclusion and matrix respectively.

In terms of the misfit-strain due to the mismatch of the coefficients of thermal expansion of the inclusion and matrix, W can be written:

$$W = 2\pi\alpha^2\Delta T^2R^3/((1-2\nu_p)/E_p + (1+\nu_m)/2E_m) \quad (3)$$

where $\Delta\alpha$ is the difference in coefficients of thermal expansion between matrix and inclusion and ΔT is the cooling range.

For randomly oriented penny-shaped microcracks of equal size, Young's modulus E_p of the inclusion can be expressed:

$$E_p = E_{po} [1 + 16(1-\nu_p^2) N \ell^3 / 9(1-2\nu_p)]^{-1} \quad (4)$$

where N is the number of cracks per unit volume of inclusion, E_{po} is the Young's modulus of the inclusion without cracks and ℓ is the radius of the cracks. The condition $\ell < R$ is assumed to exist always, for the validity of the mechanical model.

The total surface energy of the cracks within the particle is:

$$T = 4\pi R^3 N \gamma \pi \ell^2 / 3 \quad (5)$$

where γ is the surface energy.

Crack instability occurs when

$$d/d\ell (W-T) \geq 0 \quad (6)$$

Substitution of eqs. 3 and 5 into eq. 6 followed by differentiation, leads to the critical temperature difference ΔT_c based on the fracture surface energy γ_f for unstable crack propagation:

$$\Delta T_c = \left(\frac{\pi \gamma_f (1-2\nu_p)}{(\Delta\alpha)^2 E_{po} (1-\nu_p^2)^2} \right)^{1/2} \ell^{-1/2} \left(\frac{E_{po} (1+\nu_m)}{2E_m (1-2\nu_p)} + 1 + \frac{16(1-\nu_p^2) N \ell^3}{9(1-2\nu_p)} \right) \quad (7)$$

The expression for the critical temperature difference ΔT_{sc} based on the fracture surface energy γ_s for subcritical crack growth can be obtained from equation 7 by using γ_s in place of γ_f .

Small cracks of length ℓ_o which on instability at $\Delta T = \Delta T_c$ propagate in an unstable mode when $d^2(W+T)/d\ell^2 > 0$, will arrest when the total elastic strain energy released is converted to fracture surface energy. This will occur at a final crack length

$$\ell_f = (3 E_{po} (1+\nu_m) / 16 E_m (1-\nu_p) N \ell_o)^{1/2} \quad (8)$$

Equations 7 and 8 are not conveniently expressed in dimensionless form. For this reason, ΔT_c , ΔT_{sc} and ℓ_f were calculated for an MgO inclusion within a SiC matrix for a value of crack density $N = 10^8$ /unit volume and a ratio $\gamma_f/\gamma_{sc} = 4$. The solid curves in

fig. 7 denote ΔT_{sc} and ΔT_c . Similarly, ℓ_f is shown by the dotted curve.

Figure 7 shows three regimes of different crack behavior. In the regime labelled (A), the crack will propagate critically. Subcritical crack growth occurs in region B, whereas region C indicates crack healing. A number of conclusions can be made from fig. 7 related to the experimental data presented earlier.

It is critical to note that a change in ΔT also involves a change in the absolute value of temperature. This in turn, can have a large effect on the rate of the diffusional processes responsible for crack growth and crack healing. For this reason, on cooling to low temperatures microcracks are not expected to exhibit their equilibrium length, because crack growth and healing is suppressed. In other words, microcracks can be "super-cooled". Only at temperatures where rates of crack growth or healing are sufficiently high, can microcracks reach their equilibrium length corresponding to these particular values of ΔT and temperature. This implies that microcracked materials which in service are subjected to variations in temperatures, generally will not be at equilibrium and are expected to show temperature and time-dependent properties.

A number of characteristics of microcrack stability and propagation can be discussed on the basis of the numerical data in fig. 7. For small values of crack length such that in eq. 7 the term involving the crack size is small compared to unity, ΔT_c is independent of crack density and inclusion size. In addition, eq. 8 clearly indicates that for a given crack density, the final crack length which results from unstable crack propagation at $\Delta T = \Delta T_c$ also is independent of the inclusion size. This suggests that theories for the existence of a critical grain size based on energy considerations will require reexamination.

Inclusion size will have an effect on ΔT_c when for a given number of cracks, the cracks are sufficiently large such that the effective Young's modulus of the inclusion is affected. This behavior is responsible for the increase in ΔT_{sc} and ΔT_c with increasing crack length to the right of the minimum of the solid curves in fig. 7.

A microcracked material, reheated to a temperature close or equal to its fabrication or annealing temperature ($\Delta T \rightarrow 0$), will undergo crack healing. This should manifest itself in an increase in the thermal diffusivity, in agreement with the data shown in figs. 1, 3 and 4.

The value of final crack length (denoted by ℓ_f in fig. 7) which results from instability of a short crack of length ℓ_0 at

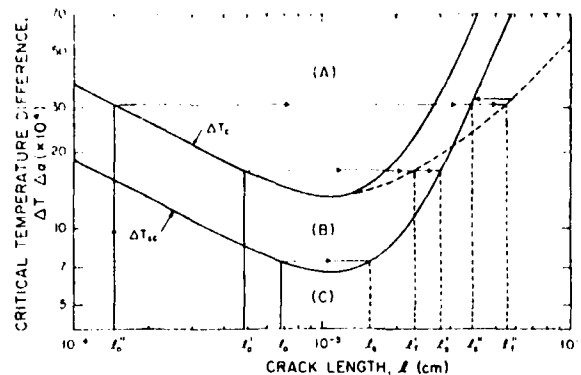


Fig. 7. Microcrack stability diagram indicating critical and sub-critical crack propagation and crack healing for three cooling histories (numerical data for MgO inclusion in SiC matrix).

ΔT_c , is subcritical with respect to ΔT_{sc} . Such a crack for any value of $\Delta T \leq \Delta T_{sc}$ will undergo permanent crack healing. For this type of crack behavior, the crack size will be largest after cooling from the preparation temperature, when the thermal diffusivity also will show its minimum. Due to crack healing, heating will cause a permanent increase in the thermal diffusivity, as shown by the data in fig. 6.

Materials with a range of sizes of precursors will undergo partial microcracking due to those precursors which are of critical size. On reheating, the microcracks will undergo healing whereas the precursors which were too small for microcracking will undergo crack growth. On a second cooling, those precursors which grew to critical size will propagate into microcracks. This behavior manifests itself in a recovery in the thermal diffusivity at higher temperatures and a room temperature diffusivity value which is lower at the end of the thermal cycle than at the beginning. This behavior is in agreement with the data shown in figs. 3 and 4. The relative rates of crack healing and precursor growth are expected to be very sensitive to temperature in view of the competitive effects of the magnitude of temperature and residual stress on the kinetics of crack healing and growth. If on the first cooling, none of the precursors were of sufficient size to create microcracks, but grew on reheating, thermal diffusivity as a function of temperature as shown in fig. 2 would be expected.

The above discussion suggests that many of the experimental observations can be explained by the analytical results for a simple mechanical model for microcrack stability and propagation

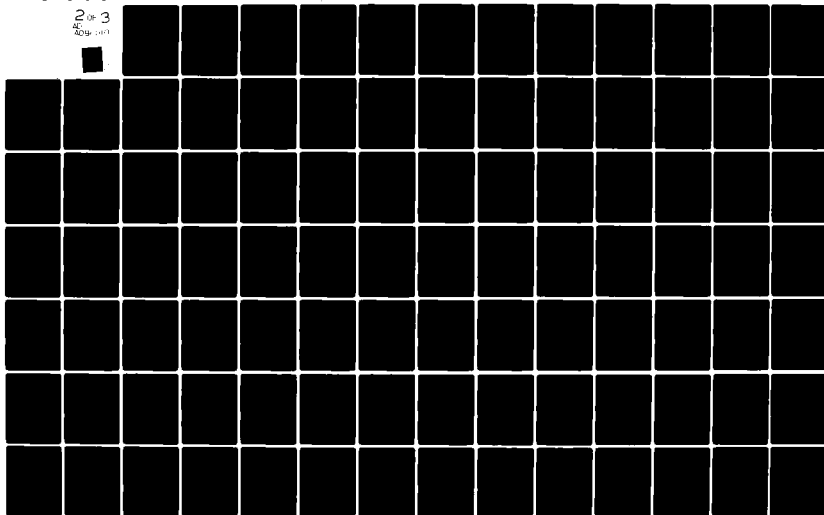
AD-A096 010

VIRGINIA POLYTECHNIC INST AND STATE UNIV BLACKSBURG --ETC F/6 11/2
THERMO-MECHANICAL AND THERMAL BEHAVIOR OF HIGH-TEMPERATURE STRU--ETC(U)
DEC 80 D P HASSELMAN N00014-78-C-0431

UNCLASSIFIED

NL

2 OF 3
AL 009-1001



behavior and that this behavior can be monitored by measurement of thermal diffusivity.

ACKNOWLEDGEMENTS

This study was conducted as part of a research program supported by the Office of Naval Research under contract N00014-78-C-0431.

REFERENCES

1. J. A. Kuszyk and R. C. Bradt, J. Am. Ceram. Soc., 56:420 (1973).
2. D.P.H. Hasselman and J.P. Singh, J. Am. Ceram. Soc., 58:856 (1979).
3. D.P.H. Hasselman, Comp. Mat., 12:403 (1978).
4. J. Selsing, J. Am. Ceram. Soc., 44:419 (1961).
5. J.J. Cleveland and R. C. Bradt, J. Am. Ceram. Soc., 61:478 (1978).
6. A.G. Evans and D. R. Clarke, in "Proc. Intl. Conf. on Thermal Stresses in Materials and Structures in Severe Thermal Environments," D.P.H. Hasselman and R. Heller, eds., Plenum Press, N.Y. (in press).
7. H.J. Siebeneck, D.P.H. Hasselman, J. J. Cleveland and R. C. Bradt, J. Am. Ceram. Soc., 59:241 (1976).
8. H.J. Siebeneck, J. J. Cleveland, D.P.H. Hasselman and R. C. Bradt, in: "Ceramic Microstructures '76", R. M. Fulrath and J. A. Pask, eds., Westview Press, Boulder, Colorado (1977).
9. J.P. Singh, D.P.H. Hasselman, W.M. Su, J.A. Rubin and R. Pallicka, J. Mat. Sc., (in press).
10. D.P.H. Hasselman, J. Am. Ceram. Soc., 52:600 (1969).
11. R.W. Davidge and T.J. Green, J. Mat. Sc., 3:629 (1968).

CHAPTER VI

THERMAL STRESSES IN PARTIALLY ABSORBING
FLAT PLATE SYMMETRICALLY HEATED BY THERMAL RADIATION
AND COOLED BY CONVECTION

by

J. P. Singh, J. R. Thomas, Jr., D. P. H. Hasselman

Departments of Materials and Mechanical Engineering
Virginia Polytechnic Institute and State University
Blacksburg, Virginia 24061

List of Symbols:

α : Greek l.c., alpha

ϵ : Greek l.c., epsilon

κ : Greek l.c., kappa

λ : Greek l.c., lambda

ν : Greek l.c., nu

μ : Greek l.c., mu

ABSTRACT

The stresses due to "thermal trapping" of internally absorbed radiation in solid materials are analyzed for a flat plate symmetrically heated by radiation and cooled by convection with finite values of the heat transfer coefficient. The thermal stress state consists of an initial transient followed by a steady state stress at $t \rightarrow \infty$ and involves a reversal in sign of the stresses. The maximum value of the transient stress increases with optical thickness whereas the maximum value of the steady-state stress occurs at an optical thickness, $\mu a \approx 1.3$ with zero stresses at $\mu a = 0$ and ∞ .

INTRODUCTION

The current interest in solar radiation as an important energy source has focused attention on the problem of thermal stress failure of materials of construction of solar installations. Analyses of thermal stresses due to radiative heat transfer involve non-linear integral equations. For this reason the usual approach of obtaining complete transient or steady-state solutions for the temperature equations from which the thermal stresses are evaluated, becomes rather complex. To circumvent this problem at least for some instances it should be noted that for a body initially at low temperature suddenly subjected to radiation heating, the temperature rise at the time when the thermal stresses are at or near their maximum value, is sufficiently small that any re-emitted radiation, to a first approximation, can be neglected. For practical purposes then, the body can be considered to be subjected to a constant heat flux.

This latter approach was followed in an analysis of thermal stresses due to radiation heating of materials essentially opaque to the incident radiation, which was absorbed in the immediate surface regions of the material [1]. This analysis was extended to include the spectral dependence of the absorption coefficient typical for dielectric materials, which to a good approximation can be described to be transparent below a given wave-length and opaque above this value of wave-length [2].

In addition to complete opacity or complete transparency, thermal radiation can also interact with materials such that it is absorbed as it is being transmitted through the material. The rate of absorption is governed by the absorption coefficient. Internal absorption of radiation, depending on the external cooling condition, can lead to the phenomenon

referred to as "thermal trapping" in which the interior of the plate reaches temperatures higher than the surface or surrounding medium [3]. The non-uniform non-linear temperature distributions associated with thermal trapping should result in thermal stresses. This effect was analyzed recently for a flat plate symmetrically heated by normally incident thermal radiation and cooled by convection for heat transfer coefficients (h) for simplicity taken as $h = 0$ and ∞ [4]. The present writers became aware of the general solutions of Viskanta et. al [3] for the thermal trapping effect involving finite values of the heat transfer coefficient. Using these solutions, the purpose of the present study is to analyze the thermal stresses in a flat plate symmetrically heated by radiation and cooled by convection for finite values of the heat transfer coefficient. Thermal stresses in assymmetrically heated plates will be presented in future reports.

ANALYSIS

A. Boundary and Initial Conditions

The flat plate, considered infinite in extent, is located in the yz -plane and $-a < x < a$. At $x = a$ and $-a$ the plate is subjected at $t = 0$ to a constant normally incident uniform thermal radiation. At $x = -a$ and a the plate is cooled by Newtonian convection with a heat transfer coefficient h . The optical properties of the material are assumed to be "grey" i.e., independent of wave-length. The reflectivity of the plate will be assumed sufficiently low that the effect of multiple reflections within the plate can be neglected. The material properties which affect the temperature distribution and thermal stresses, such as the emissivity (absorptivity), absorption coefficient, thermal conductivity and thermal diffusivity, the

coefficient of thermal expansion, Young's modulus and Poisson's ratio are assumed to be independent of temperature. As stated earlier, it will be assumed that over the time period for the stresses to reach a value equal to or nearly equal to their maximum, the temperatures in the plate remain sufficiently low that the intensity of the re-emitted radiation to a first approximation is negligible in comparison to the incident radiation.

The intensity of the heat flux, q within the plate due to the thermal radiation entering at $x = a$ is:

$$q = \epsilon q_0 e^{-\mu(a-x)} \quad (1)$$

where ϵ is the emissivity (or $\epsilon = 1 - r$ where r is the reflectivity) q_0 is the intensity of the incident heat flux and μ is the absorption coefficient.

Similarly, the radiation within the plate due to the incident radiation at $x = -a$ is:

$$q = \epsilon q_0 e^{-\mu(a+x)} \quad (2)$$

From eqs. 1 and 2 the total radiative heat flux (q_t) within the plate is:

$$q_t = 2\epsilon q_0 e^{-\mu a} \cosh(\mu x) \quad (3)$$

The rate of internal heat absorption (g''') within the plate is:

$$g''' = 2\mu\epsilon q_0 e^{-\mu a} \cosh(\mu x) \quad (4)$$

Solutions for the transient temperature (T) are obtained by solving [5]:

$$\frac{\partial^2 T}{\partial x^2} + \frac{g'''(x)}{k} = \frac{1}{\kappa} \frac{\partial T}{\partial x} \quad (5)$$

where k is the thermal conductivity and κ is the thermal diffusivity.

For the present heating and cooling conditions the initial and boundary conditions are:

$$T(x,0) = T_0 \quad (6)$$

$$\frac{\partial T}{\partial x}(0,t) = 0 \quad (7)$$

$$\frac{\partial T}{\partial x}(a,t) = -\frac{h}{k} \{T(a,t) - T_0\} \quad (8)$$

$$\frac{\partial T}{\partial x}(-a,t) = -\frac{h}{k} \{T(-a,t) - T_0\} \quad (9)$$

where h is the heat transfer coefficient.

For $h = 0$, the initial and boundary conditions are given by Eqs. (6) and (7) and

$$\frac{\partial T}{\partial x}(-a,t) = \frac{\partial T}{\partial x}(a,t) = 0 \quad (10)$$

B. Solutions for transient temperatures.

Solution of Eq. (5) for the initial and boundary conditions given by Eqs. (6), (7), (8) and (9) yields:

$$T(x,t) = T_0 + \sum_{n=0}^{\infty} B_n(t) \cos(\lambda_n x) \quad (11)$$

where λ_n are the roots of the transcendental equation

$$\lambda_n \tan(\lambda_n a) = h/k \quad (12)$$

and

$$B_n(t) = \frac{G_n}{\kappa \lambda_n^2} (1 - e^{-\kappa \lambda_n^2 t}) \quad (13)$$

$$\text{with } G_n = \frac{2\kappa\mu\epsilon q_0 e^{-\mu a}}{N_n k} \left[\frac{\mu \cos(\lambda_n a)(e^{\mu a} - e^{-\mu a}) + \lambda_n \sin(\lambda_n a)(e^{\mu a} + e^{-\mu a})}{\mu^2 + \lambda_n^2} \right]$$

$$\text{and } N_n = a + \frac{h}{\lambda_n^2 k} \cos(\lambda_n a)$$

C. Thermal stresses.

Expressions for the thermal stresses $\sigma_{y,z}(x,t)$ are obtained by substitution of Eq. (11) for T in [6]:

$$\sigma_{y,z} = \frac{\alpha E}{1-\nu} \left[-T + \frac{1}{2a} \int_{-a}^a T dx + \frac{3x}{2a^3} \int_{-a}^a T x dx \right] \quad (14)$$

which yields:

$$\sigma_{y,z} = \frac{-\alpha E}{1-\nu} \sum_{n=0}^{\infty} B_n(t) \cos(\lambda_n x) + \frac{\alpha E}{a(1-\nu)} \sum_{n=0}^{\infty} \frac{B_n(t)}{\lambda_n} \sin(\lambda_n a)$$

For convenience the numerical results are reported in terms of the non-dimensional temperature:

$$T^* = (T - T_0)k/\epsilon q_0 a$$

the non-dimensional stress:

$$\sigma^* = \sigma(1-\nu)k/\alpha E q_0 \epsilon a$$

the non-dimensional time:

$$t^* = \kappa t/a^2$$

and the non-dimensional distance, x/a .

RESULTS AND DISCUSSION

Figure 1 shows the stresses at the center ($x=0$) and surface ($x = -a$ and a) of the plate (with $a = 1$ cm) as a function of time for a range of values of the optical thickness, and h/k arbitrarily chosen equal to 0.09 cm^{-1} .

Figure 2 shows the stresses in the center and surface of the plate ($a = 1$ cm) as a function of time for a range of values of $h/k \text{ (cm}^{-1}\text{)}$ for arbitrary value of the optical thickness, $\mu a = 3$.

Figures 3 and 4 give the maximum values of the transient and steady-state thermal stresses as a function of optical thickness, μ_a .

From the above figures a number of effects may be noted. Firstly, it may be observed that after an initial transient the thermal stresses reach a steady-state value at $t \rightarrow \infty$. The maximum value of the transient stresses increases with increasing optical thickness, μ_a as shown in Fig. 3. In contrast, the steady-state value of the thermal stresses as shown in Fig. 4 exhibits a maximum at $\mu_a \approx 1.3$ and approaches zero as $\mu_a \rightarrow 0$ or ∞ . Secondly, the magnitude of the transient thermal stresses is a function of h/k , whereas the steady-state stresses are independent of h/k . It is of interest to note that the maximum transient stresses decrease with increasing h/k , in contrast to many literature solutions for transient thermal stresses in convective heat transfer which indicate that the magnitude of maximum thermal stress increases with increasing heat transfer coefficient. The independence of the steady-state stress on h/k occurs because the profile of the temperature distribution within the plate is independent of h/k , in spite of the fact that the magnitude of the temperatures for a given profile is an inverse function of the heat transfer coefficient. A steady-state temperature distribution will be attained regardless of the magnitude of the heat transfer coefficient, with the exception of $h = 0$. For this latter value of h , although the thermal stresses after an initial transient will attain a constant value [4], the temperatures will continue increasing linearly with time (at least within the assumption that the re-emitted radiation can be neglected).

The "thermal trapping" and associated thermal stresses are most effectively illustrated for the limiting value of the heat transfer coefficient $h = \infty$. For this value no increase in surface temperature occurs,

and the temperature rise within the plate is due to the internal absorption of the incident radiation. As indicated by Fig. 4, this effect is most pronounced at an optical thickness $\mu a \approx 1.3$.

Probably the most interesting observation as indicated by Figs. 1 and 2 is the reversal in sign of the stresses in going from the transient to the steady-state condition. This phenomenon is the direct result of the thermal trapping and the spatial non-uniformity of the heat generation within the plate, which is a maximum in the surface regions of the plate. During the very initial time periods after initiation of radiation at $t = 0$, the regions of the plate in the immediate surface area will be at a higher temperature than the interior of the plate. During this period, the heat losses by convection from the plate are relatively small for small values of h with the heat flowing primarily from the surface regions towards the interior of the plate. This results in a temperature distribution such that the surface is placed in compression, whereas the center of the plate is in tension. However, as the plate approaches the steady-state condition ($t \rightarrow \infty$), the surface temperatures will be sufficiently high that the heat losses at the surface by convection become appreciable. In fact, the maximum surface temperature will correspond to the condition that the heat lost by convection equals the total radiation energy absorbed. Under this condition, all heat generated within the plate must flow outward. This implies that the maximum temperature occurs at the center of the plate (for this symmetric case), which will result in a tensile stress in the plate surface and a compressive stress in the plate interior. However, as $h/k \rightarrow \infty$, no stress reversal in the surface takes place because the surface temperature remains constant resulting in the tensile stress for $t > 0$. This effect of the reversal

of stress is illustrated in Figs. 5 and 6 which give the spatial variation of the temperature and stress for increasing values of t^* for the specific case of $h/k = 1 \text{ cm}^{-1}$ and $\mu a = 10$. As far as these authors are aware the occurrence of such a stress reversal has not been reported in the literature to date. It appears that this phenomenon requires a spatially non-uniform internal heat generation and may not only be encountered in the absorption of thermal radiation but possibly nuclear radiation as well, such as in the form of neutrons or other nuclear particles.

ACKNOWLEDGMENTS

This study was conducted as part of a research program on the thermo-mechanical and thermal properties of brittle structural materials supported by the Office of Naval Research under Contract N00014-78-C-0431.

REFERENCES

1. D. P. H. Hasselman, Thermal Shock by Radiation Heating, J. Amer. Ceram. Soc., Vol. 46, pp. 229-234, 1963.
2. D. P. H. Hasselman, Theory of Thermal Stress Resistance of Semi-Transparent Ceramics Under Radiation Heating, J. Amer. Ceram. Soc., Vol. 49, pp. 103-104, 1966.
3. R. Viskanta and E. E. Anderson, Heat Transfer in Semitransparent Solids in F. Irvine, Jr., and James P. Hartnett (eds.), Advances in Heat Transfer, Vol. 11, pp. 317-441, Academic Press, New York, 1975.
4. D. P. H. Hasselman, J. R. Thomas, Jr., M. P. Kamat and K. Satyamurthy, Thermal Stress Analysis of Partially Absorbing Brittle Ceramics Subjected to Symmetric Radiation Heating, J. Amer. Ceram. Soc., (in press).
5. H. S. Carslaw and J. C. Jaeger, Conduction of Heat in Solids, 2nd Ed., Oxford at the Clarendon Press (1960).
6. B. A. Boley and J. H. Wiener, Theory of Thermal Stresses, Wiley, New York, 1960.

List of Figures

- Figure 1. Maximum thermal stress in a partially absorbing flat plate symmetrically heated by normally incident radiation and cooled by convection for a range of values for optical thickness, μa with $h/k = 0.03 \text{ cm.}^{-1}$ and $a = 1 \text{ cm.}$
- Figure 2. Time dependence of maximum thermal stress in a partially absorbing flat plate symmetrically heated by normally incident radiation and cooled by convection for various values of $h/k \text{ (cm.}^{-1}\text{)}$ with optical thickness, $\mu a = 3$ and $a = 1 \text{ cm.}$
- Figure 3. Maximum values of transient thermal stresses as a function of optical thickness μa in a partially absorbing flat plate symmetrically heated by normally incident radiation and cooled by convection for various values of $h/k \text{ (cm.}^{-1}\text{)}$ with $a = 1 \text{ cm.}$
- Figure 4. Maximum values of steady state stress as a function of optical thickness μa in a partially absorbing flat plate symmetrically heated by normally incident radiation and cooled by convection for various values of $h/k \text{ (cm.}^{-1}\text{)}$ with $a = 1 \text{ cm.}$
- Figure 5. Temperature distribution in a partially absorbing flat plate symmetrically heated by normally incident radiation and cooled by convection for various values of time with $h/k = 1 \text{ cm.}^{-1}$, $\mu a = 10$ and $a = 1 \text{ cm.}$
- Figure 6. Stress distribution in a partially absorbing flat plate symmetrically heated by normally incident radiation and cooled by convection for various values of time with $h/k = 1 \text{ cm.}^{-1}$, $\mu a = 10$ and $a = 1 \text{ cm.}$

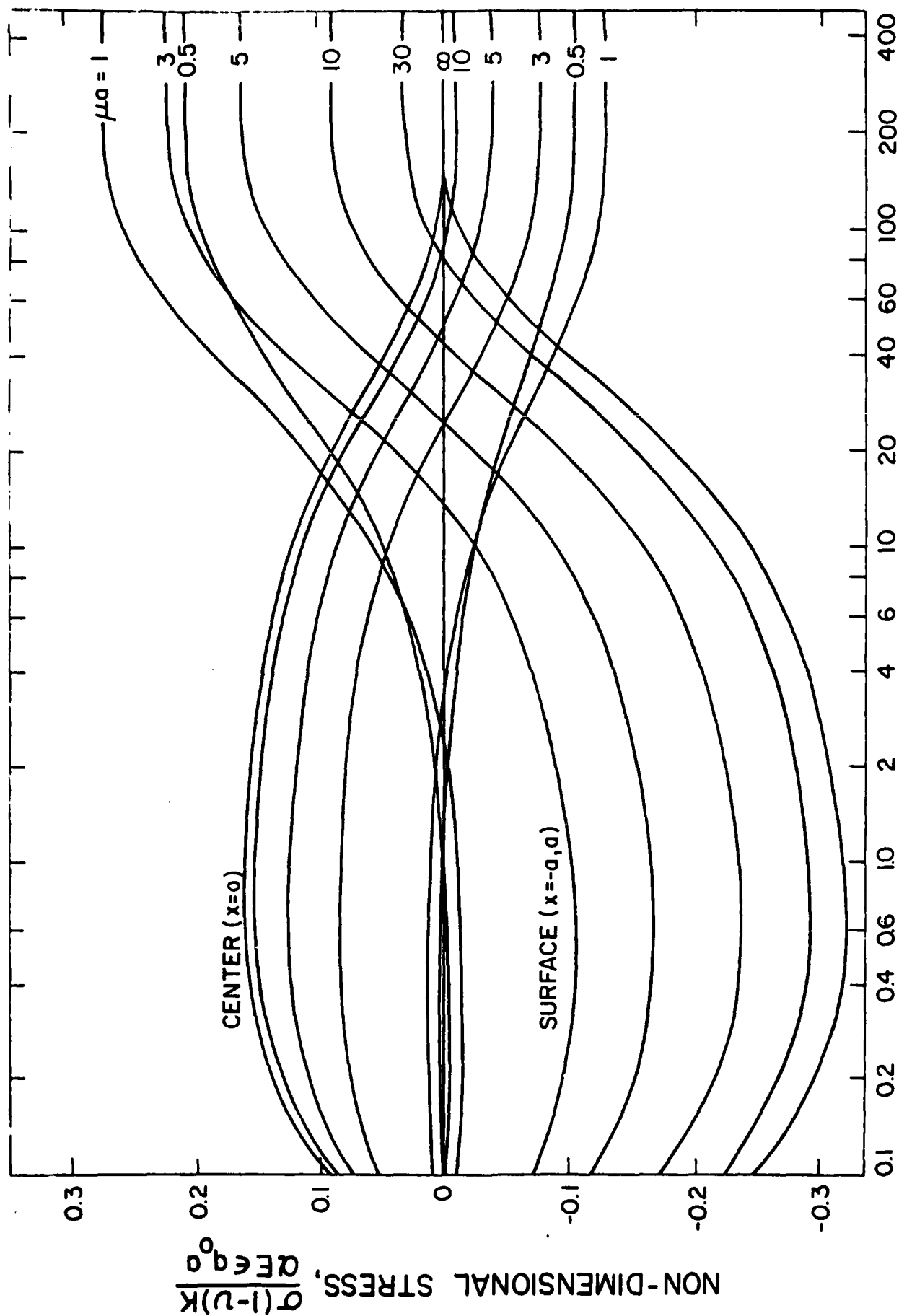


Fig. 1. Maximum thermal stress in a partially absorbing flat plate symmetrically heated by normally incident radiation and cooled by convection for a range of values for optical thickness, μa with $h/k = 0.03 \text{ cm}^{-1}$ and $a = 1 \text{ cm}$.

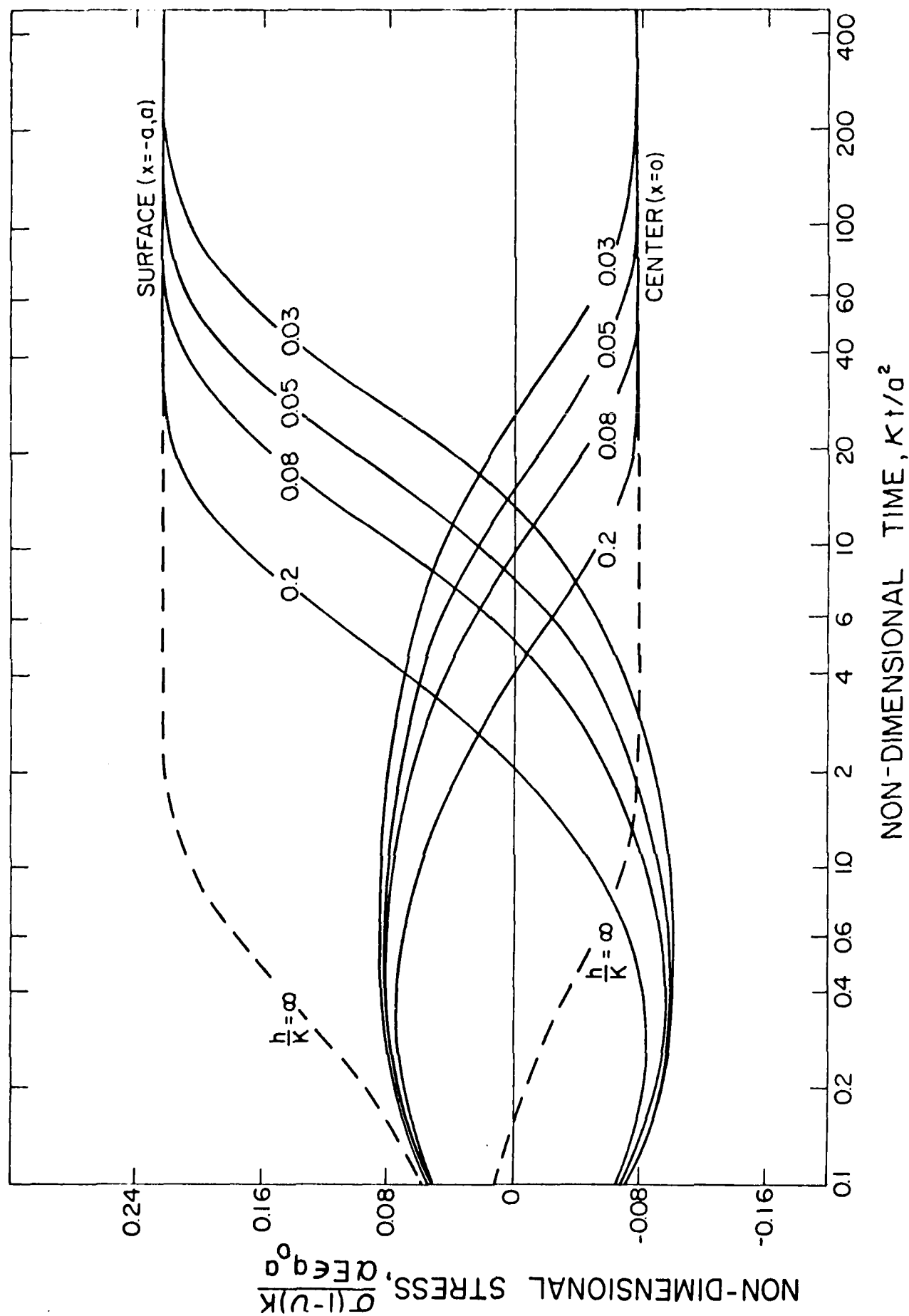


Fig. 2. Time dependence of maximum thermal stress in a partially absorbing flat plate symmetrically heated by normally incident radiation and cooled by convection for various values of h/k (cm.⁻¹) with optical thickness, $\mu_a = 3$ and $a = 1$ cm.

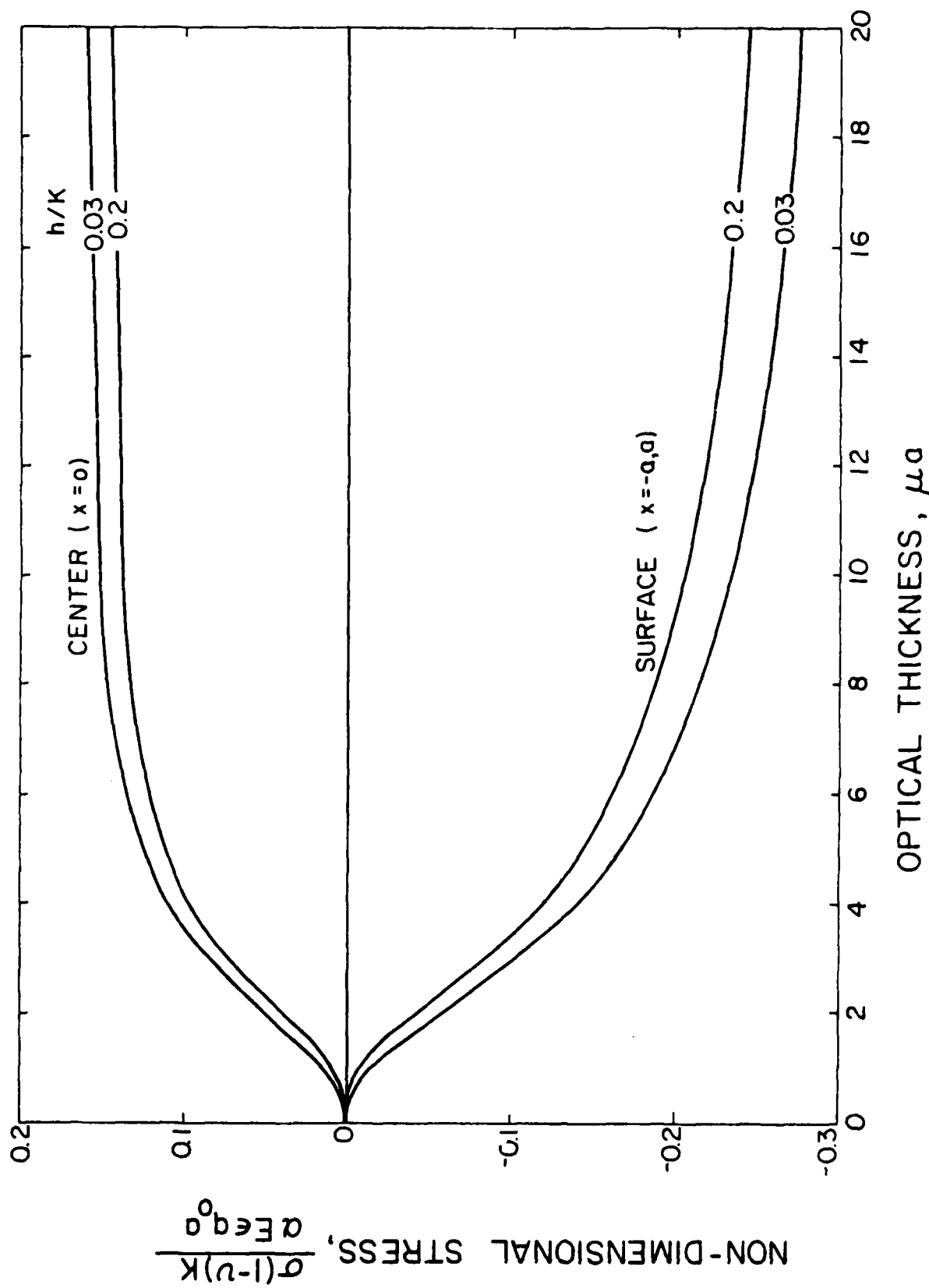


Fig. 3. Maximum values of transient thermal stresses as a function of optical thickness μa in a partially absorbing flat plate symmetrically heated by normally incident radiation and cooled by convection for various values of h/k (cm.⁻¹) with $a = 1$ cm.

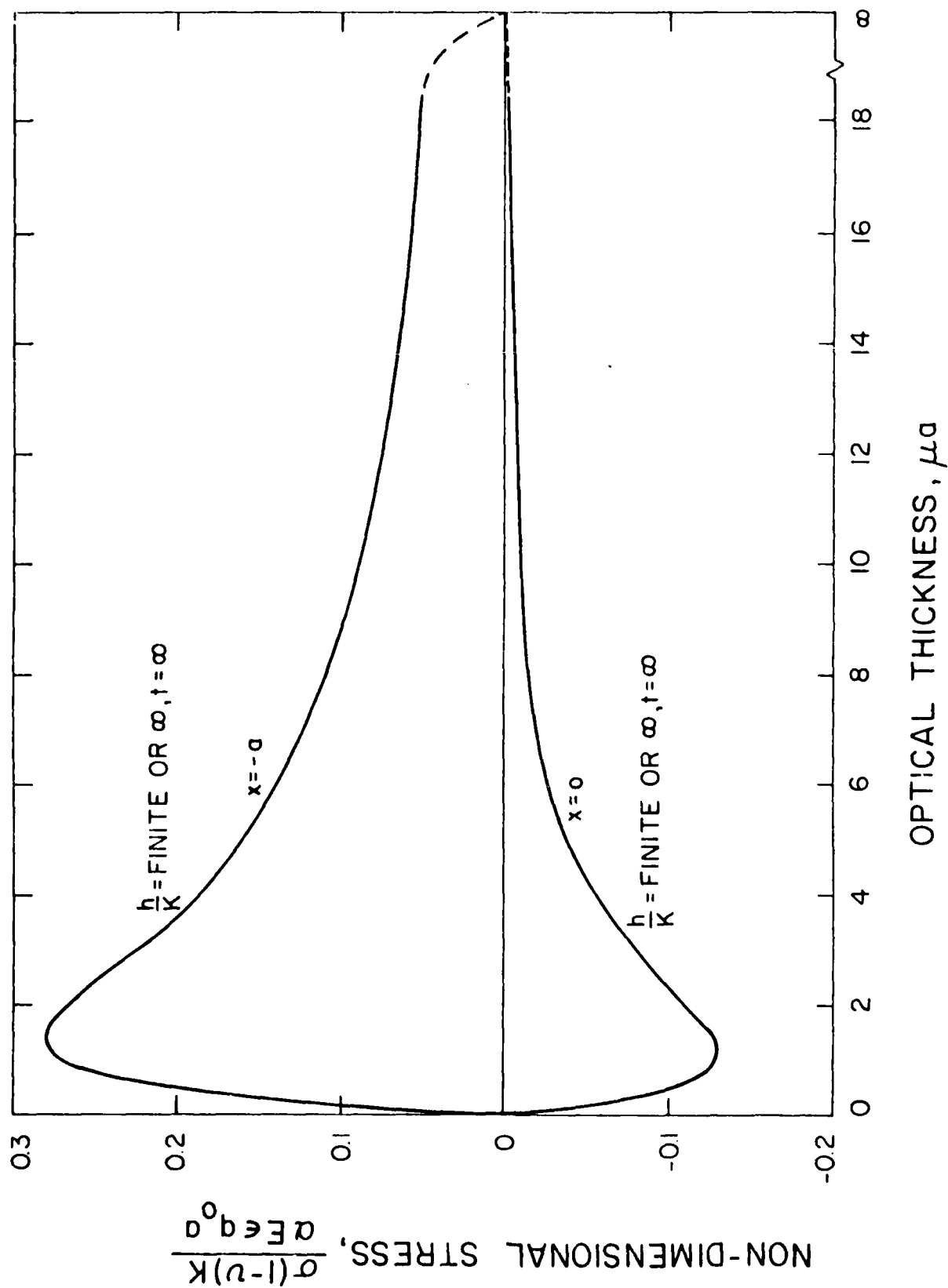


Fig. 4. Maximum values of steady state stress as a function of optical thickness μa in a partially absorbing flat plate symmetrically heated by normally incident radiation and cooled by convection for various values of h/k (cm.⁻¹) with $a = 1$ cm.

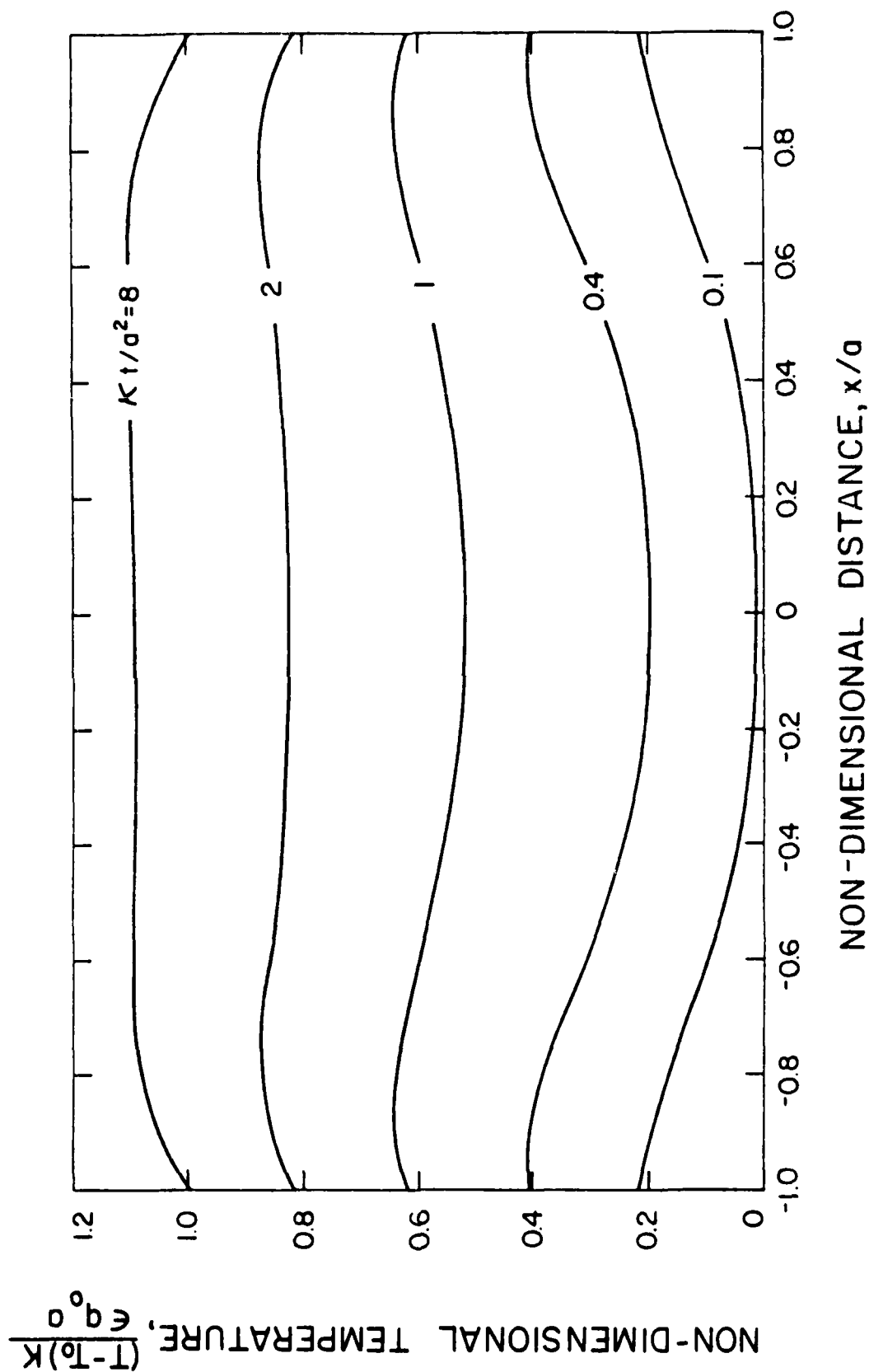


Fig. 5. Temperature distribution in a partially absorbing flat plate symmetrically heated by normally incident radiation and cooled by convection for various values of time with $h/k = 1 \text{ cm.}^{-1}$, $\mu a = 10$ and $a = 1 \text{ cm.}$

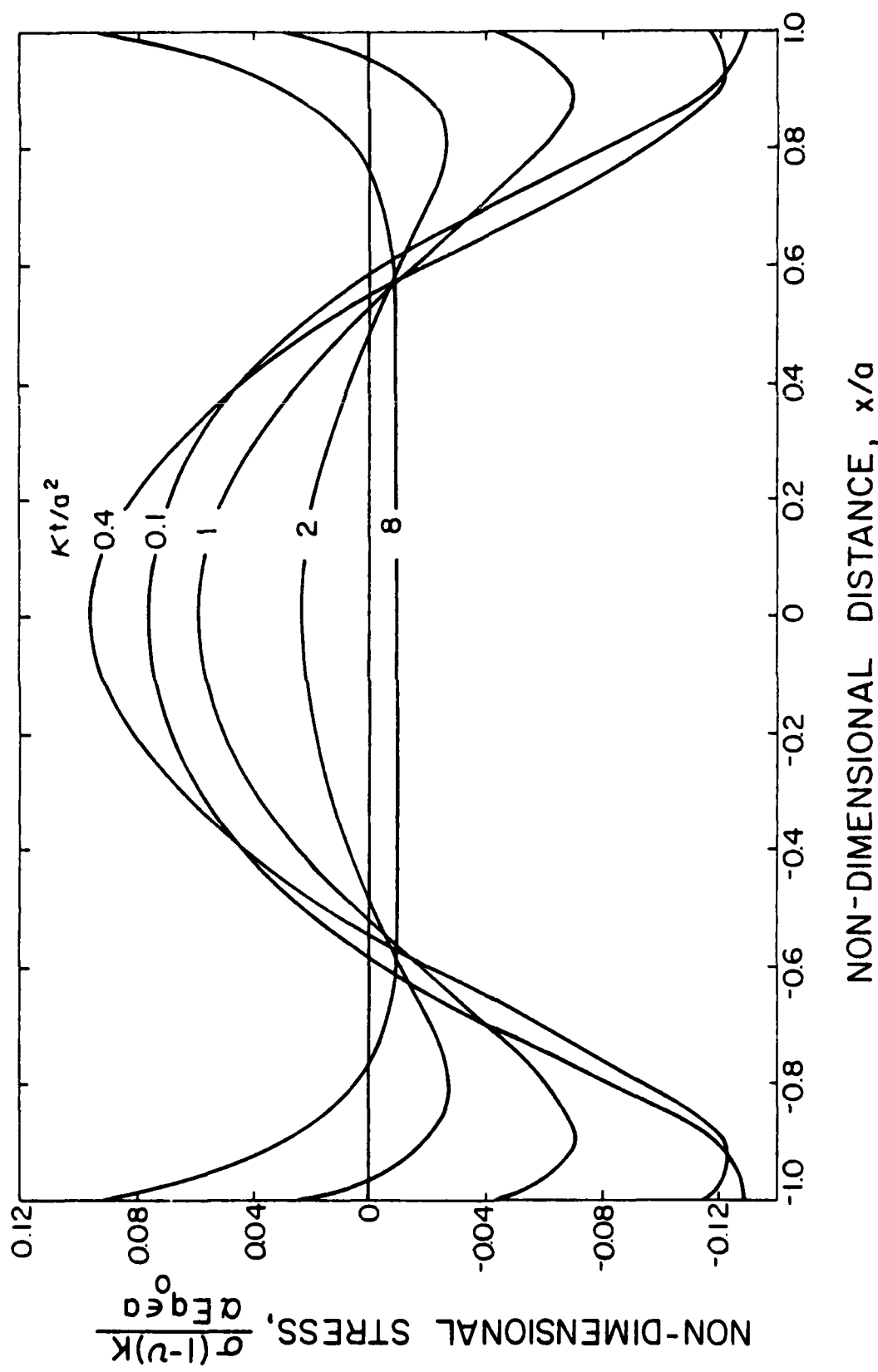


Fig. 6. Stress distribution in a partially absorbing flat plate symmetrically heated by normally incident radiation and cooled by convection for various values of time with $h/k = 1 \text{ cm.}^{-1}$, $\mu a = 10$ and $a = 1 \text{ cm.}$

CHAPTER VII

ANALYSIS OF THERMAL STRESS RESISTANCE OF PARTIALLY ABSORBING CERAMIC PLATE SUBJECTED TO ASSYMMETRIC RADIATION, II: CONVECTIVE COOLING AT FRONT SURFACE

by

J. P. Singh, K. Satyamurthy, J. R. Thomas, D. P. H. Hasselman

Departments of Mechanical and Materials Engineering
Virginia Polytechnic Institute and State University
Blacksburg, Virginia 24061, USA

ABSTRACT

Thermal stresses in a partially absorbing brittle ceramic plate assymmetrically heated by radiation and cooled by convection on the same surface with finite and infinite heat transfer coefficient are analyzed.

Comparison of the results from this study with those obtained in Part I, where the plate is subjected to radiation heating in the front surface and cooled by convection at the rear surface, indicates that the magnitude of the maximum steady state tensile thermal stresses are nearly identical. Significant differences are found in the transient thermal stresses and the temperature distribution. The relative temperature levels in the present case are found to be significantly lower than those obtained in Part I. Implications of these results to the design and operation of engineering structures such as concentrated solar receivers are discussed.

I. INTRODUCTION

A number of analyses on the role of the properties which affect the thermal stress resistance of semi-absorbing ceramics were presented previously^{1,2,3}. For these studies the geometry consisted of a flat plate subjected to symmetric radiation heating and convective cooling as well as asymmetric radiation heating on one side of the plate with cooling on the opposite face. For these two heating and cooling conditions, the magnitude of the maximum tensile thermal stress was found to be a complex function of the optical thickness (absorption coefficient times plate thickness). At steady-state ($t = \infty$), for non-zero heat transfer coefficient the thermal stresses were equal to zero for values of the optical thickness equal to 0 and ∞ . For a non-zero heat transfer coefficient the maximum value of steady-state tensile thermal stress for the symmetric and asymmetric radiation heating occurred at values of the optical thickness of 1.334 and 2, respectively.

Comparison of the numerical results shows that for the symmetrically heated and cooled plate the magnitude of the thermal stresses considerably exceed those for asymmetric heating and cooling. The reason for this is that in the asymmetric case, the non-uniformity of the thermal expansions in part can be accommodated by bending. In view of the symmetric temperature distributions, this mode of deformation cannot occur for symmetric heating and cooling.

Comparison of the temperature distributions, on the other hand, shows that for high values of optical thickness (i.e. opaque materials) the temperature differences encountered at steady-state for asymmetric heating and cooling significantly exceed those for symmetric heating and cooling.

This occurs because in the symmetric heating and cooling case, the heat is removed from the same surface subjected to radiation, with little or no heat absorption in the interior of the material. In fact, for an optical thickness which approaches infinity, the temperature within the plate at steady-state (time $t \rightarrow \infty$) is uniform. Under this condition the rise in temperature above ambient is inversely proportional to the convective heat transfer coefficient (with exception of $h = 0$). In contrast, for the plate heated by radiation at the front face and cooled by convection at the back face, all the heat must be conducted through the thickness of the plate. This will result in a highly non-uniform temperature distribution even at an optical thickness of infinity and steady-state conditions for which the magnitude of thermal stresses equals zero. For high radiation fluxes this can result in excessive front face temperatures even for moderate or low rear face temperature especially for ceramic materials with moderate or low values of thermal conductivity. This latter effect can have important implications for the design and operation of concentrated solar energy receivers which generally will operate in an asymmetric heating mode and for which ceramic materials are serious contenders for the materials of construction. In order to avoid excessively high temperatures at the front face subjected to radiation, may well require limiting the temperature of the back-face. This in turn would reduce the temperature of the heat transfer fluid with an associated decrease in overall efficiency of the receiver. If so, a design modification appears in order. One such modification is suggested by the previous analyses, which indicate that asymmetric heating and convective cooling at the same side of the plate can result in the lower

thermal stresses associated with the assymmetric heating and the greater temperature uniformity observed for the symmetric heating and cooling.

Accordingly, the objective of this study is to analyze the role of the material properties in the thermal stress resistance and temperature distribution in a ceramic plate subjected to radiative heating and convective cooling at the same side, with no heat transfer (i.e., completely insulated) at the opposite (back) face of the plate.

II. ANALYSIS

The flat plate of thickness $2a$, located parallel to y - z plane and bounded by $x = a$ and $-a$, is initially at a uniform temperature, T_0 . It is heated by an incident radiation, q_0 , and cooled by Newtonian convection with heat transfer coefficient, h , at $x = -a$. Similar to the previous study,¹ it was assumed that the reflectivity of the plate is small enough to neglect the effect of multiple internal reflection and the physical properties of the material are independent of temperature. It was also assumed that the temperature of the plate, over the time period required for stresses to reach their maximum, was low enough that the re-emission of the absorbed energy is negligible in comparison to the incident radiation. In addition, the optical properties of the plate was taken to be independent of the wavelength of the incident radiation.

A. Temperature Distribution

Due to the normally incident radiation, q_0 , on the front face ($x = -a$) of the plate, the flux transmitted through the surface is ϵq_0 where $\epsilon = 1 - r$

with r being the reflectivity. The rate of internal heat generation (g''') within the plate is given by¹:

$$g'''(x) = \mu \epsilon q_0 e^{-\mu(a+x)}$$

where μ is the absorption coefficient. The temperature solutions (T) for the specific initial and boundary conditions were obtained by solving the differential equation⁴:

$$\frac{\partial^2 T}{\partial x^2} + \frac{g'''(x)}{k} = \left(\frac{1}{\kappa}\right) \frac{\partial T}{\partial x} \quad (1)$$

where k is the thermal conductivity and κ is the thermal diffusivity.

Equation (1) was solved for three values of heat transfer coefficient, h , viz. $h = 0$, finite and infinity. The initial and boundary conditions along with the temperature solutions are as follows:

a. Finite heat transfer coefficient, h

The initial and boundary conditions are:

$$T(x, 0) = T_0; \quad \frac{\partial T}{\partial x}(a, t) = 0 \quad (2)$$

$$k \frac{\partial T}{\partial x}(-a, t) = h\{T(-a, t) - T_0\} \quad (3)$$

The solution of equation (1) subjected to the initial and boundary conditions (2) and (3) is given by:

$$T(x, t) = T_0 + \sum_{n=0}^{\infty} B_n(t) \cos \lambda_n(a-x) \quad (4)$$

where

$$B_n(t) = \frac{G_n}{\kappa \lambda_n^2} [1 - e^{-\kappa \lambda_n^2 t}] \quad (5a)$$

$$G_n = \frac{\kappa q_0 \mu \epsilon}{N k} \left[\frac{\lambda_n \sin(2\lambda_n a) - \mu e^{-2\mu a}}{\mu^2 + \lambda_n^2} \right] \quad (5b)$$

$$N_n = a + \frac{h}{2\lambda_n^2 k} \cos^2(2\lambda_n a) \quad (5c)$$

and λ_n is the root of the transcendental equation:

$$\lambda_n \tan(2\lambda_n a) = \frac{h}{k} \quad (6)$$

b. Heat transfer coefficient, $h = \infty$

The initial and boundary conditions are:

$$T(x, 0) = T(-a, t) = T_0 \quad (7)$$

$$\frac{\partial T}{\partial x}(a, t) = 0 \quad (8)$$

The temperature solution for conditions (7) and (8) is given by:

$$T(x, t) = T_0 + \sum_{n=0}^{\infty} B_n(t) \sin\{\lambda_n(x+a)\} \quad (9)$$

where

$$B_n(t) = \frac{G_n}{\kappa \lambda_n^2} [1 - e^{-\kappa \lambda_n^2 t}] \quad (10a)$$

$$G_n = \frac{\kappa q_0 \mu e}{ak} \left[\frac{\lambda_n - \mu e^{-2\mu a} \sin(2\lambda_n a)}{\mu^2 + \lambda_n^2} \right] \quad (10b)$$

$$\text{and} \quad \lambda_n = \frac{(2n-1)\pi}{4a} \text{ with } n=0, 1, 2, \dots \quad (10c)$$

The thermal environment with $h=0$ is identical to the one discussed in an earlier study and, therefore, the expressions for temperature and thermal stresses for this case can be found in reference 3.

B. Thermal Stresses

The expressions for thermal stresses were obtained from⁵:

$$\sigma_{y,z} = \frac{\alpha E}{1-\nu} \left[-T + \frac{1}{2a} \int_{-a}^a T dx + \frac{3x}{2a^3} \int_{-a}^a T x dx \right] \quad (11)$$

where α is the coefficient of thermal expansion, E is the Young's modulus of elasticity, ν is the Poisson's ratio and T is the temperature,

The stresses were obtained for two cases with finite and infinite heat transfer coefficients:

a. Finite heat transfer coefficient, h

For this case the temperature distribution T in equation (4) was substituted in equation (11) to yield the thermal stress distribution:

$$\begin{aligned}\sigma_{y,z} = & -\frac{\alpha E}{1-\nu} \sum_{n=0}^{\infty} B_n(t) \cos\{\lambda_n(a-x)\} \\ & + \frac{\alpha E}{2a(1-\nu)} \sum_{n=0}^{\infty} \frac{B_n(t) \sin(2\lambda_n a)}{\lambda_n} \\ & + \frac{3\alpha E}{2a^3(1-\nu)} \sum_{n=0}^{\infty} B_n(t) \left[\frac{1-\cos(2\lambda_n a)}{\lambda_n^2} - \frac{a \sin(2\lambda_n a)}{\lambda_n} \right] \quad (12)\end{aligned}$$

where $B_n(t)$ and λ_n are defined in equations (5) and (6).

b. Heat transfer coefficient $h = \infty$

Thermal stress distribution for this case was obtained from equations (9) and (11):

$$\begin{aligned}\sigma_{y,z} = & -\frac{\alpha E}{(1-\nu)} \sum_{n=1}^{\infty} B_n(t) \sin\{\lambda_n(x+a)\} \\ & + \frac{\alpha E}{2a(1-\nu)} \sum_{n=1}^{\infty} \frac{B_n(t)}{\lambda_n} \\ & + \frac{3\alpha E}{2a^3(1-\nu)} \sum_{n=1}^{\infty} B_n(t) \left[\frac{\sin(2\lambda_n a)}{\lambda_n^2} - \frac{a}{\lambda_n} \right] \quad (13)\end{aligned}$$

where $B_n(t)$ and λ_n are defined in equation (10).

The maximum steady state tensile stress is found to occur in the front face of the plate ($x = -a$) and is given by:

$$\sigma_{\max}(-a, \infty) = \frac{\alpha E}{2a(1-\nu)} \sum_{n=1}^{\infty} \frac{G_n}{\kappa \lambda_n^3} - \frac{3\alpha E}{2a^2(1-\nu)} \sum_{n=1}^{\infty} \frac{G_n}{\kappa \lambda_n^2} \left[\frac{\sin(2\lambda_n a)}{\lambda_n^2} - \frac{a}{\lambda_n} \right] \quad (14)$$

where G_n is defined in equation (10b).

Equation (14) can be simplified for optically very thick ($\mu a \rightarrow \infty$) and optically very thin ($\mu a \ll 1$) plates to:

$$\sigma_{\max}(-a, \infty) = 0 \quad (\mu a \rightarrow \infty) \quad (15a)$$

$$\sigma_{\max}(-a, \infty) = \frac{\alpha E q_0 \epsilon \mu a^2}{3(1-\nu)k} \quad (\mu a \ll 1) \quad (15b)$$

Equating σ_{\max} with the tensile strength S_t , the expressions for the maximum permissible heat flux q_{\max} to which the plate can be subjected without the risk of failure under steady state condition is given by:

$$q_{\max} \rightarrow \infty \quad (\mu a \rightarrow \infty) \quad (16a)$$

$$q_{\max} = \frac{3S_t(1-\nu)k}{\alpha E \epsilon \mu a^2} \quad (\mu a \ll 1) \quad (16b)$$

III. NUMERICAL RESULTS AND DISCUSSION

Following previous practice¹⁻⁴, the temperatures, stresses and time will be presented in the non-dimensional form:

$$T^* = (T - T_0) k / \epsilon q_0 a \quad (17a)$$

$$\sigma^* = \sigma (1 - \nu) k / \alpha E \epsilon q_0 a \quad (17b)$$

$$\text{and} \quad \alpha = \kappa t / a^2 \quad (17c)$$

for convenience, hereafter, referred to as temperature, stress and time, respectively.

Figures 1a and 2a, for a range of values of time and $h = 0.06$ watts. $\text{cm.}^{-2} \text{C}^{-1}$. show the spatial variation of the temperature within the plate for values of optical thickness $\mu a = 0.5$ and 30, respectively. These results indicate that during the initial stages of heating, the regions of the plate near the front surface are at a higher temperature than those regions near the back surface. This is because the rate of heat generation within the plate near the front is higher than near the back. This effect is more pronounced for the higher value of optical thickness, since the incident radiation does not penetrate as far into the plate as for the lower values of optical thickness.

At higher values of time ($t \rightarrow \infty$), however, the temperature near the rear of the plate exceeds those near the front. This effect, is expected for any non-zero value of the heat transfer coefficient since all the absorbed heat must be removed in the front, resulting in a heat flow in a direction opposite to that of the incoming radiation.

Figures 1b and 2b show the distribution of stresses corresponding to the temperatures shown in figs. 1a and 2a. For $\mu a = 0.5$, the stresses in the front surface of the plate are always tensile even at the shortest values of time at which the front of the plate is at higher temperature. As pointed out in Part I of this study, tensile thermal stresses can occur

in the hottest part of a structure, when the temperature distribution is assymmetric and exhibits a downward concavity. This effect is absent for $\mu a = 30$ for which the temperature distributions exhibit an upward concavity over most of its range with the exception of the region immediately at the surface of the plate at the lower values of time.

For purposes of comparison with the results obtained in Part I of this study, fig. 3 shows the spatial distribution of temperature at $t = \infty$ and $h = 0.06 \text{ watts.cm.}^{-2} \text{C.}^{-1}$ for a range of values of μa . For other values of the heat transfer coefficient, the temperature distributions are identical to those shown in fig. 3 with the exception that the temperature at the front surface of the plate is inversely proportional to the heat transfer coefficient. As expected, for all values of μa , the temperature distribution shows a positive gradient since all the absorbed heat is removed at the front of the plate. For $\mu a = \infty$, the plate is at uniform temperature throughout, since at thermal equilibrium all the heat absorbed by radiation in the immediate surface is removed by convection without flowing into the plate interior.

Figure 4 shows the effect of the magnitude of the heat transfer coefficient on the magnitude of maximum tensile stress for $\mu a = 3.0$. The magnitude of the peak transient tensile thermal stress at the beginning of the thermal history is an inverse function of the heat transfer coefficient. At thermal equilibrium ($t \rightarrow \infty$), the magnitude of stress is independent of the value of the heat transfer coefficient.

Figures 5a and 5b show the transient behavior of the maximum tensile stress for a range of values of μa and values of $h = 0.06 \text{ watts.Cm.}^{-2} \text{C.}^{-1}$ and ∞ , respectively. For $h = 0.06 \text{ watts.Cm.}^{-2} \text{C.}^{-1}$ and $\mu a \geq 2$ the stresses go through a transient peak, before reaching their equilibrium value.

For $h = 0.06 \text{ watts.cm.}^{-2} \text{C.}^{-1}$ and $\mu a \leq 2$ and all values of μa for $h = \infty$ no such peak transient thermal stress exists.

Figure 6 summarizes the values for maximum tensile stress as a function of optical thickness, μa . Above an optical thickness, $\mu a \geq 11$, the peak transient stresses exceed the steady-state stresses. Conversely, for $\mu a \leq 11$, the steady-state stresses exceed the transient stresses. For $\mu a < 2$ no peak transient stresses are found. Maximum steady-state stresses are found at $\mu a \approx 2$.

A comparison of the present results with those obtained in Part I of this study indicates that for asymmetric radiation heating with convective cooling at the front or rear surface, the magnitude of the maximum steady-state tensile thermal stresses are nearly identical, but significant differences are found in the transient thermal stresses and the temperature distributions.

For purposes of discussion of this latter effect, the value of optical thickness, $\mu a = \infty$ can be taken as an extreme case. At steady-state ($t = \infty$) the stresses for both front and rear cooling are identically equal to zero. For front cooling as found in the present study, the zero thermal stress state results from the temperature state which is completely uniform throughout the plate thickness as shown in fig. 3. In contrast, for cooling at the rear surface, the heat absorbed in the front is transferred by solid conduction throughout the thickness of the plate. As shown in fig. 4a of Part I of this study, this results in a linear temperature distribution. Such a linear temperature distribution in an unconstrained plate, also results in a zero-thermal stress state. The temperature gradient in this case equals, $dT/dx = -q_0/k$.

The above observation is critical to the design and operation of structures asymmetrically heated by radiation and cooled by convection such as receivers of concentrated solar energy. For high collector

efficiency it is critical that the temperature of the working fluid be as high as possible. This requires the high temperature of the surface from which the heat is transferred to the working fluid. For cooling at the rear surface, this implies that the front surface will be at a higher temperature than the rear surface, as for $\mu a \rightarrow \infty$ all absorbed radiation must be transported through the plate by solid conduction.

This effect can be illustrated by a numerical example. For a peak solar intensity of 10^3 watts/m^2 concentrated by a factor of 200 at the surface of the plate, with a value of thermal conductivity of $0.05 \text{ watts/cm}^\circ\text{C}$ (representative of a ceramic at higher temperature) and a value of $\epsilon = 1 - r = 0.9$, the temperature gradient in the plate $dT/dx \approx -300^\circ\text{C.cm}^{-1}$. For a plate of unit thickness, this value of temperature gradient, yields a value for the temperature difference between the front and rear of the plate of 300°C . For rear surface temperatures as high as possible such a temperature difference, will result in front surface temperatures, which could result in oxidation, creep, evaporation and greatly reduced service-life, depending on the ceramic chosen as structural material. Furthermore, even in the absence of thermal stress, high temperature gradients within a material can cause excessive warpage which also must be taken into account. For a temperature gradient of $300^\circ\text{C.cm}^{-1}$, the radius of curvature R , induced in a plate of aluminum oxide ($\alpha \approx 8 \times 10^{-6}^\circ\text{C}^{-1}$) becomes $R \approx 400 \text{ cm}$. Not only will this cause large undesirable displacement, but the plate may even start acting as a lens.

No such disadvantages are found for a plate heated by radiation and cooled by convection on the same side. For $\mu a = \infty$ and $t = \infty$, the temperatures are uniform and of a magnitude considerably below those for a plate

heated by radiation and cooled by convection at opposite surfaces.

As indicated by the combined results of Part I and II of this study, from the point of view of minimizing temperatures and thermal stresses, a solar receiver consisting of a dual-plate design can be used to advantage. The front plate should be highly transparent ($\mu_a \rightarrow 0$), to transmit as much solar radiation as possible. On the other hand the second plate should be highly opaque ($\mu_a \rightarrow \infty$). The working fluid should be placed between the plates to be heated by the second plate which absorbs the radiation. This design reduces problems with temperature related material degradation to a minimum. The above is a further illustration of the well known concept that structures made of structural ceramics must be designed in such a manner to fully benefit from the advantages ceramic materials can offer.

ACKNOWLEDGMENT

This study was supported in part by the Office of Naval Research under contract: N00014-78-C-0431 and by the Department of Materials Engineering and the Department of Mechanical Engineering of Virginia Polytechnic Institute and State University.

REFERENCES

1. D. P. H. Hasselman, J. R. Thomas, Jr., M. P. Kamat and K. Satyamurthy, "Thermal Stress Analysis of Partially Absorbing Brittle Ceramics Subjected to Symmetric Radiation Heating," J. Am. Ceram. Soc. (in press).
2. J. P. Singh, J. R. Thomas and D. P. H. Hasselman, "Thermal Stresses in Partially Absorbing Flat Plate Symmetrically Heated by Thermal Radiation and Cooled by Convection," J. Thermal Stresses (in press)
3. J. R. Thomas, J. P. Singh and D. P. H. Hasselman, "Analysis of Thermal Stress Resistance of Partially Absorbing Ceramic Plate Subjected to Assymmetric Radiation, I: Convection Cooling at Rear Surface," J. Amer. Ceram. Soc. (in review).
4. H. S. Carslaw and J. C. Jaeger, Conduction of Heat in Solids, 2nd Ed. Oxford at the Clarendon Press (1960) 510 pp.
5. B. A. Boley and J. H. Weiner, Theory of Thermal Stresses, John Wiley and Sons, New York, N.Y. (1960) 586 pp.

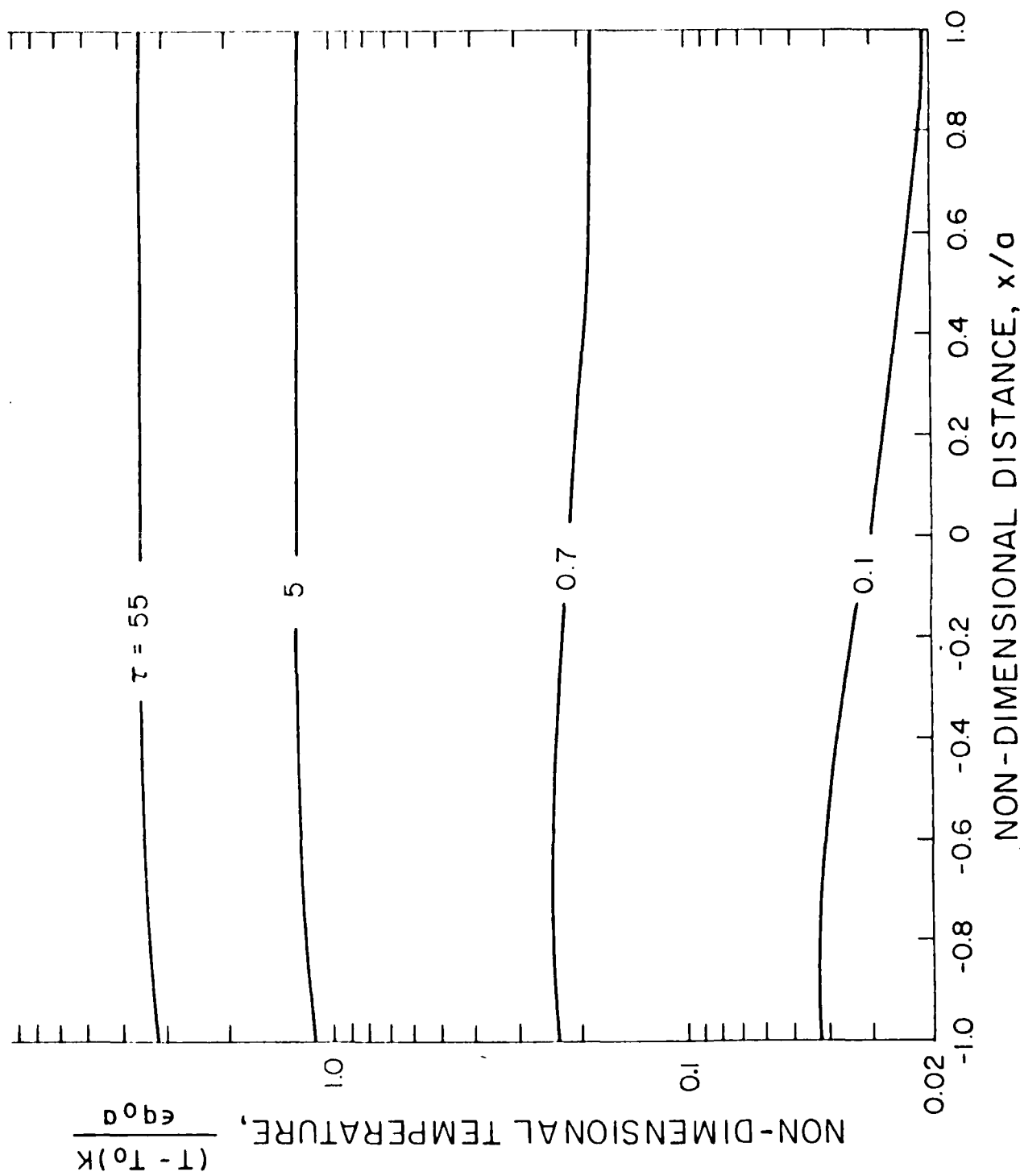


Fig. 1a. Spatial distribution of temperature for various values of time in a partially absorbing flat plate subjected to radiation heating and convection cooling at the front face with heat transfer coefficient, $h = 0.06$ (watts.cm⁻².°C⁻¹), $K = 0.3$ watts. cm⁻¹.°C⁻¹, $\mu_a = 0.5$ and $d = 1$ cm.

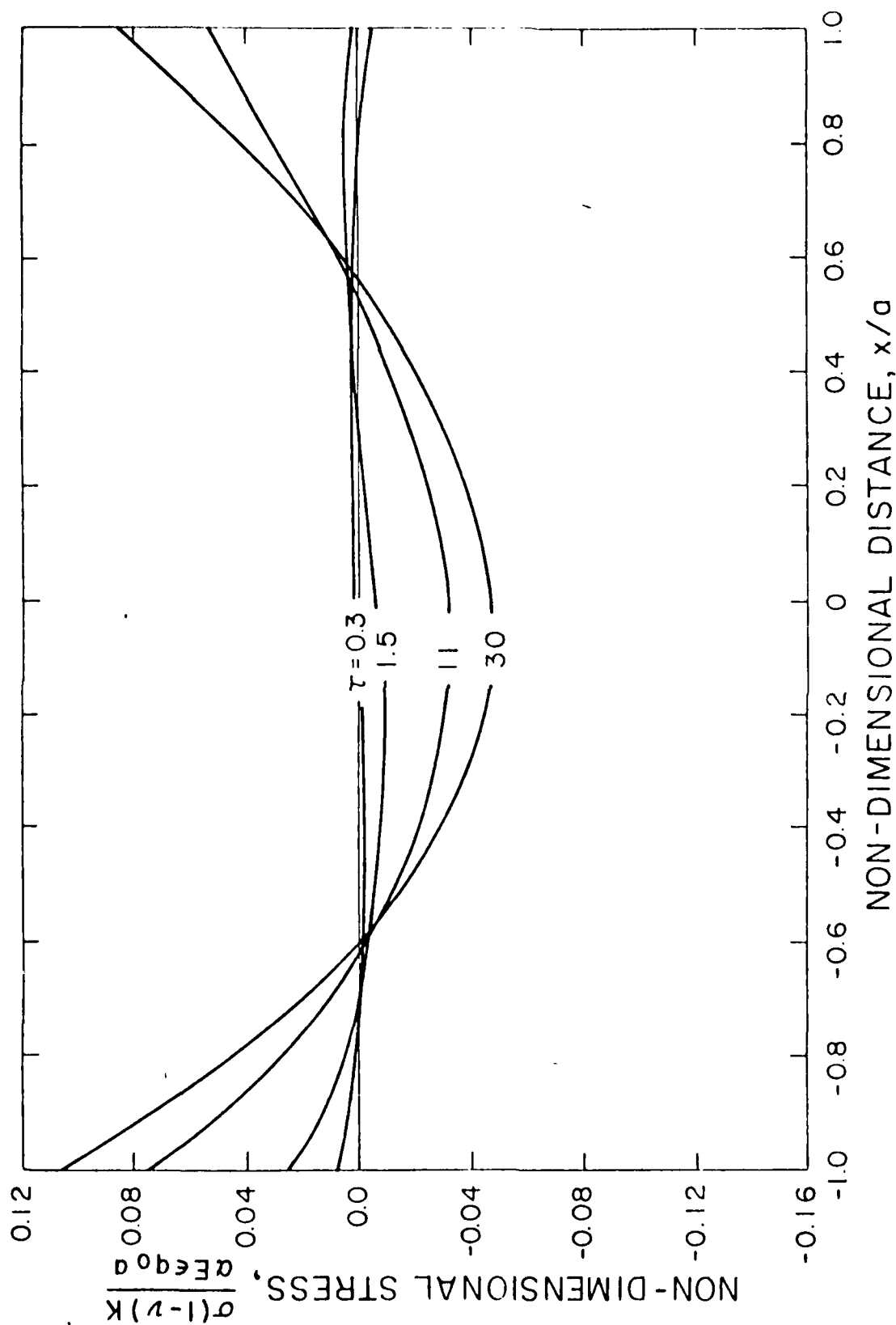


Fig. 1b. Spatial variation of thermal stresses for various values of time in a partially absorbing flat plate subjected to radiation heating and convection cooling at the front face with heat transfer coefficient, $h = 0.06$ (watts. cm. $^{-2}$ C $^{-1}$), $K = 0.3$ watts. cm. $^{-1}$ C $^{-1}$, $\nu a = 0.5$ and $a = 1$ cm.

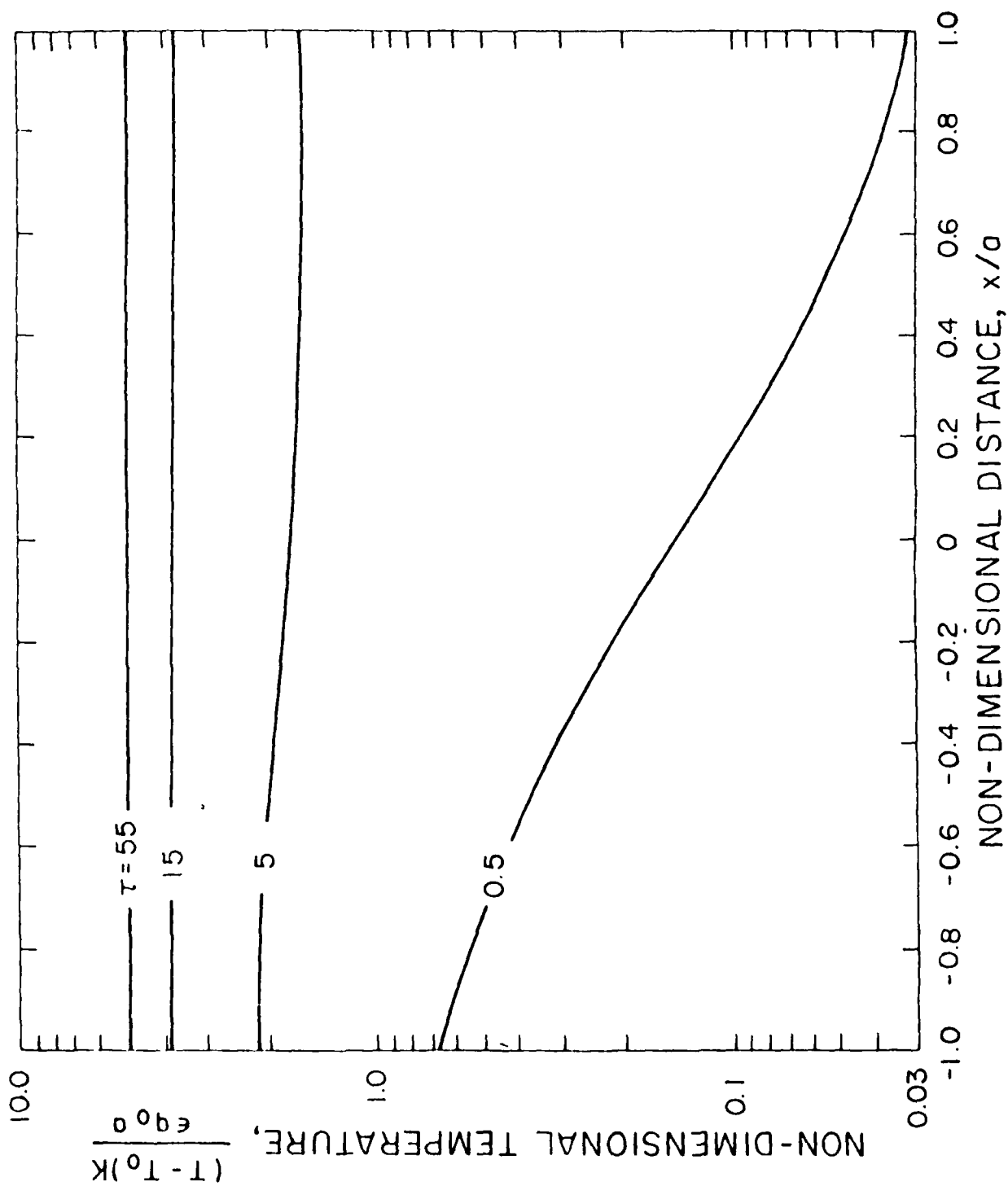


Fig. 2a. Spatial distribution of temperature for various values of time in a partially absorbing flat plate subjected to radiation heating and convection cooling at the front face with heat transfer coefficient $h = 0.06$ (watts. $\text{cm}^{-2}\text{.}^{\circ}\text{C}^{-1}$), $K = 0.3$ watts. $\text{cm}^{-1}\text{.}^{\circ}\text{C}^{-1}$, $\mu a = 30$ and $a = 1$ cm.

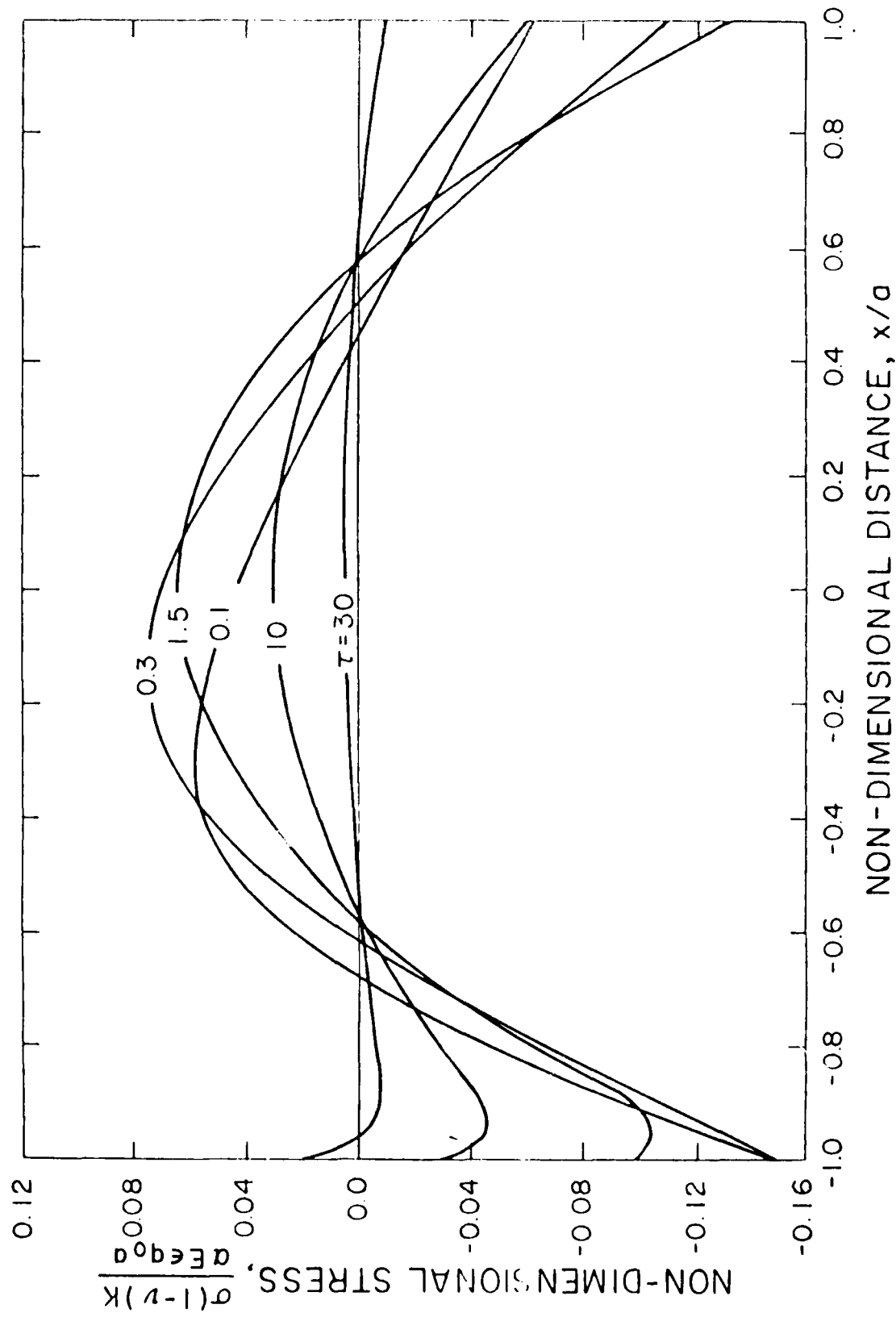


Fig. 2b. Spatial variation of thermal stresses for various values of time in a partially absorbing flat plate subjected to radiation heating and convection cooling at the front surface with heat transfer coefficient, $h = 0.06$ (watts. cm. $^{-2}$ °C $^{-1}$), $K = 0.3$ watts. cm. $^{-1}$ °C $^{-1}$, $\nu a = 30$ and $a = 1$ cm.

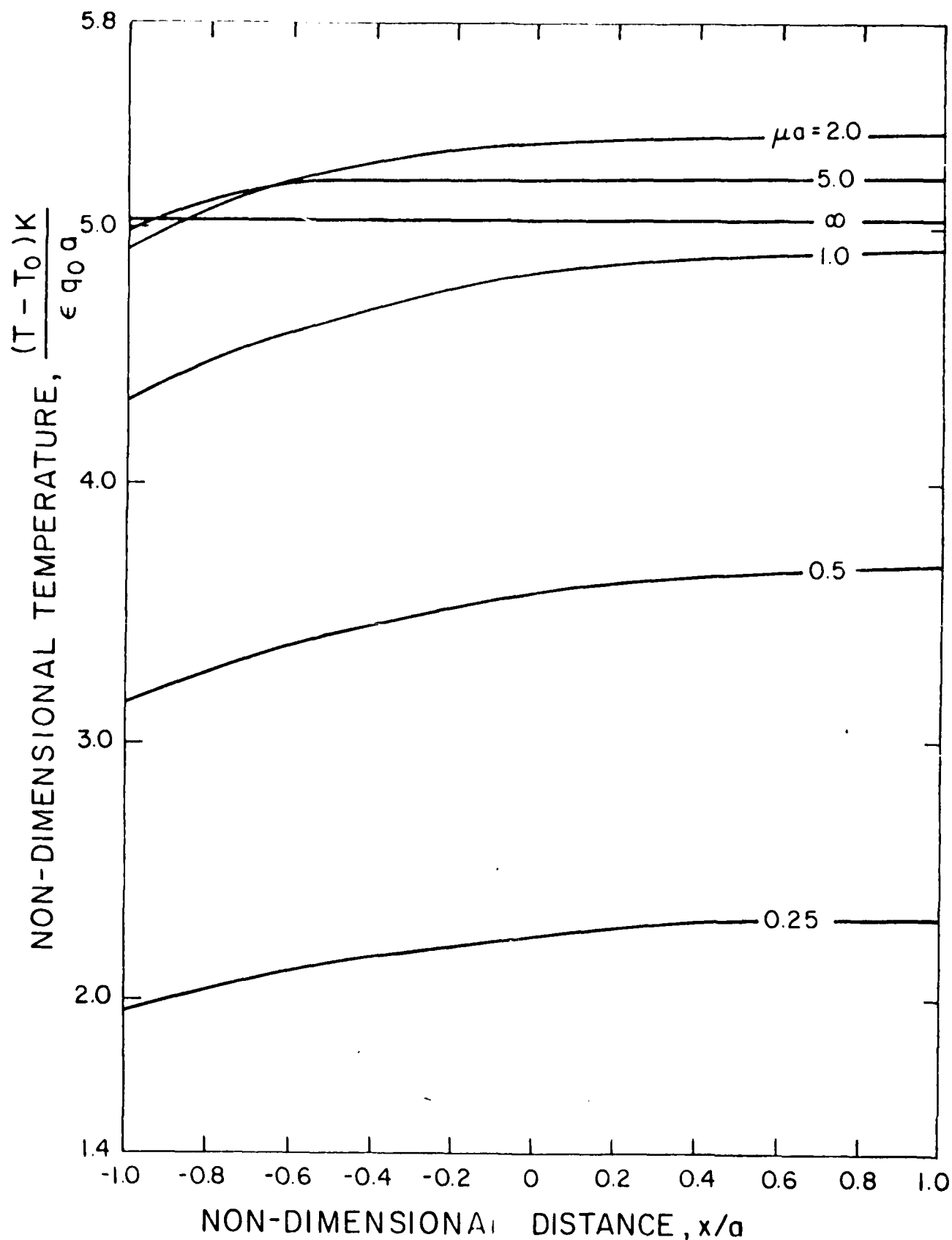


Fig. 3. Spatial distribution of steady state ($t \rightarrow \infty$) temperature for various values of μa in a partially absorbing flat plate subjected to radiation heating and convection cooling at the front face with heat transfer coefficient, $h = 0.06$ (watts.cm. $^{-2}$ °C $^{-1}$), $k = 0.3$ watts.cm. $^{-1}$ °C $^{-1}$ and $a = 1$ cm.

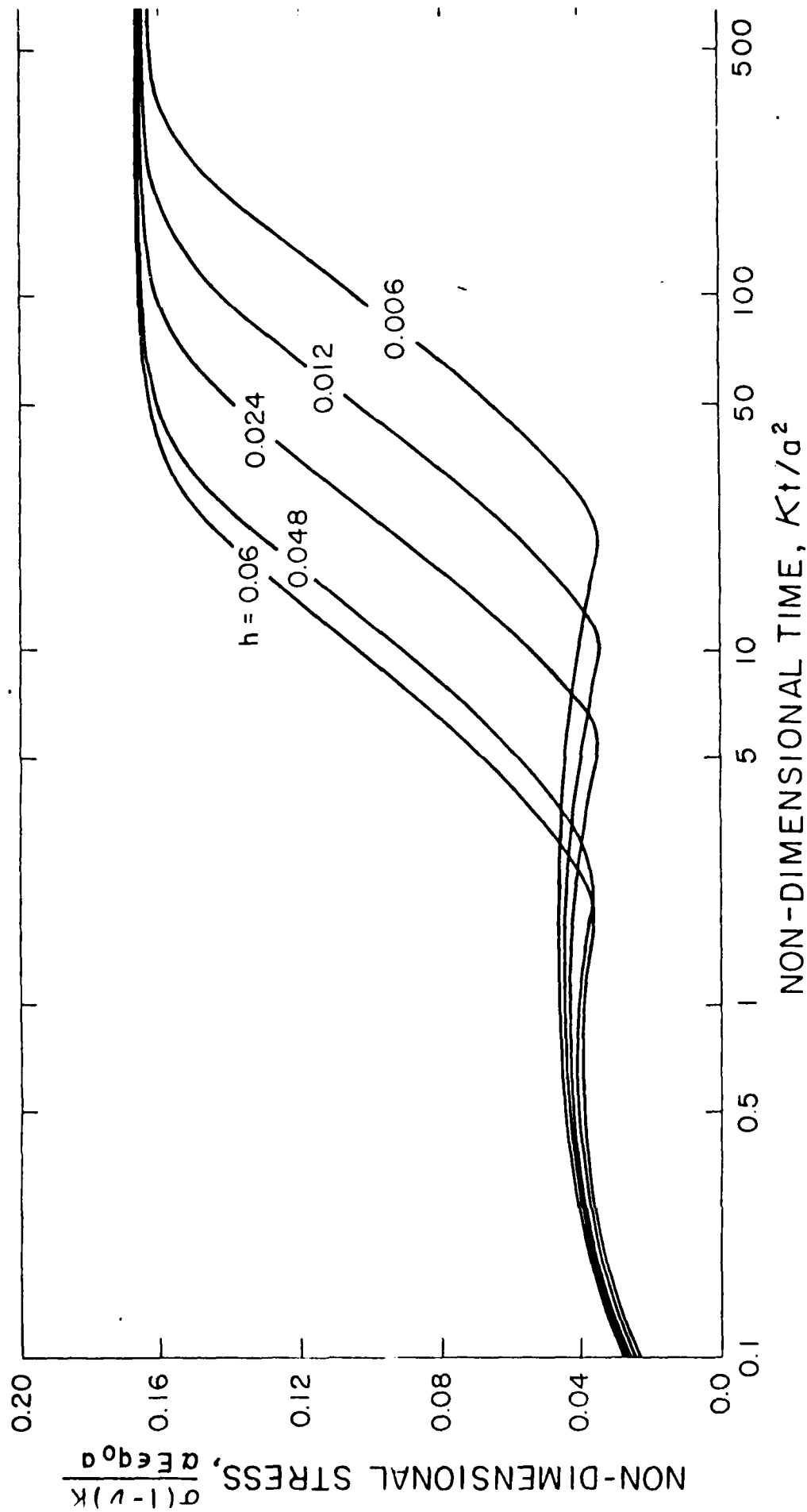


Fig. 4. Time dependence of the maximum tensile thermal stress in a partially absorbing flat plate subjected to radiation heating and convection cooling at the front face for various values of heat transfer coefficient, h (watts. $\text{cm}^{-2} \text{ } ^\circ\text{C}^{-1}$) with $K = 0.3$ watts. $\text{cm}^{-1} \text{ } ^\circ\text{C}^{-1}$, $\mu a = 3.0$ and $\nu = 1$ cm.

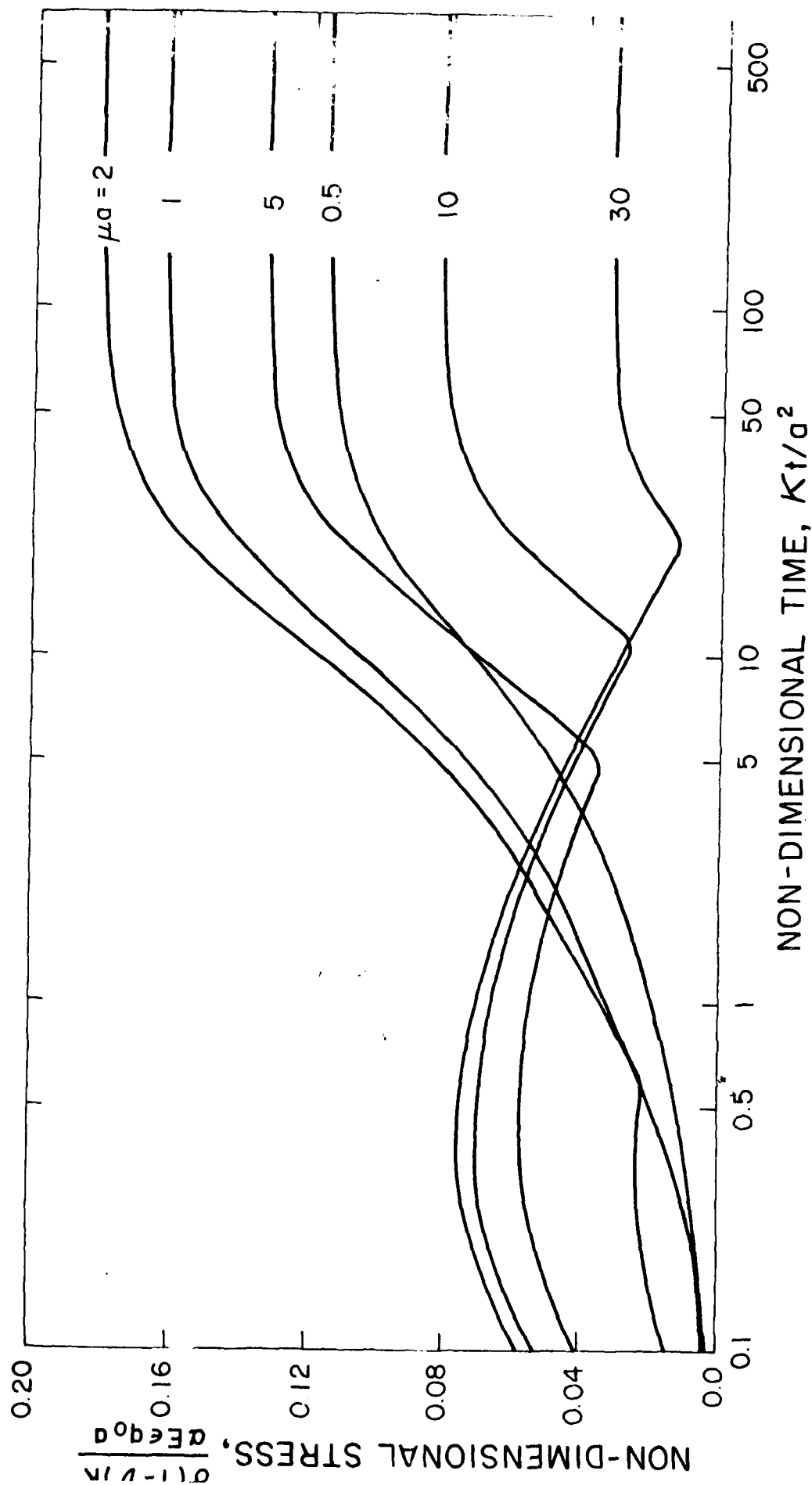


Fig. 5a. Time dependence of the maximum tensile thermal stress for various values of μa in a partially absorbing flat plate subjected to radiation heating and convection cooling at the front face with heat transfer coefficient. $h = 0.06$ (watts. cm.⁻²°C⁻¹), $K = 0.3$ watts. cm.⁻¹°C⁻¹ and $a = 1$ cm.

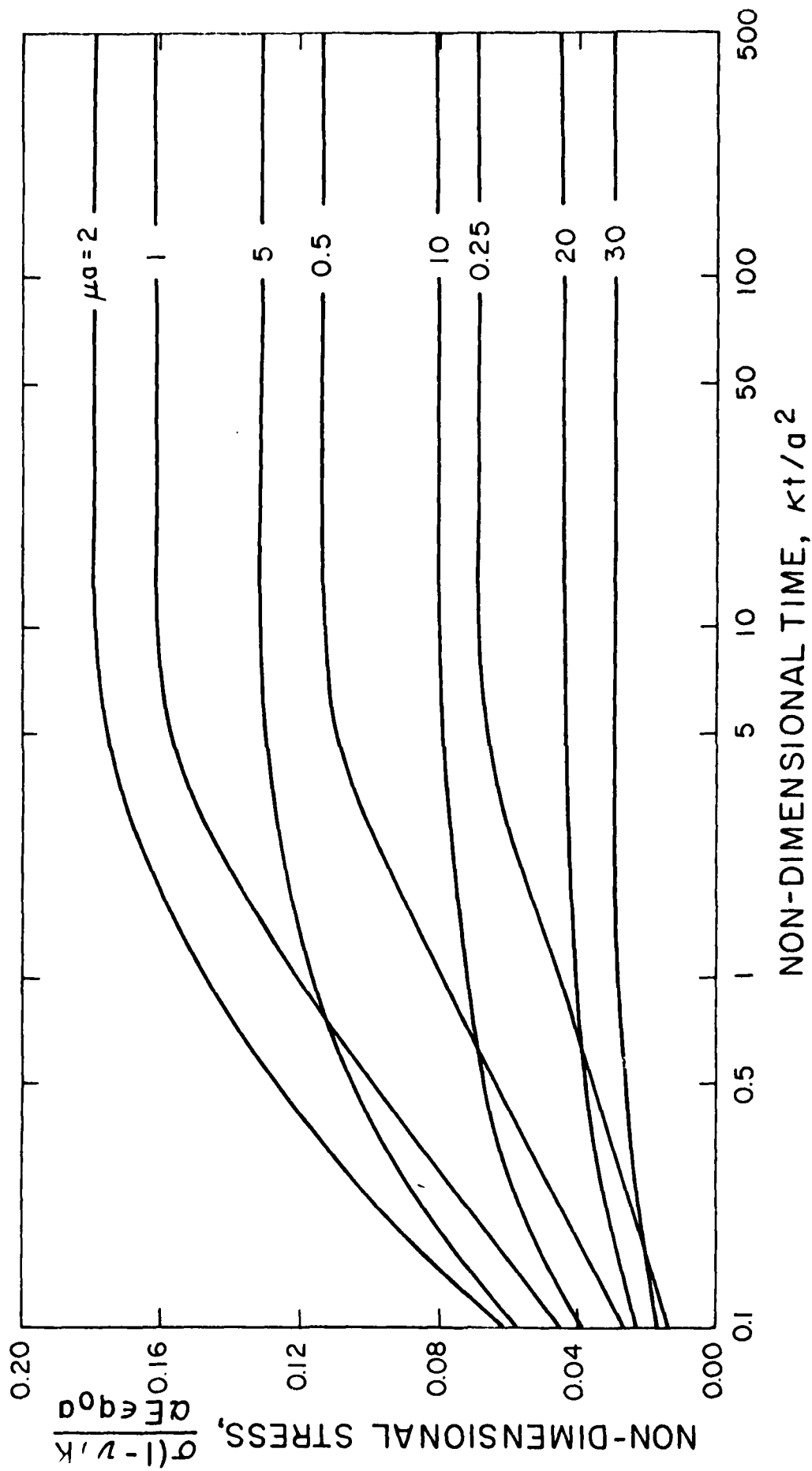


Fig. 5b. Time dependence of the maximum tensile thermal stress for various values of μa in a partially absorbing flat plate subjected to radiation heating and convection cooling at the front face with heat transfer coefficient, $h = \infty$, $K = 0.3 \text{ watts.cm.}^{-1}\text{C}^{-1}$ and $a = 1 \text{ cm}$.

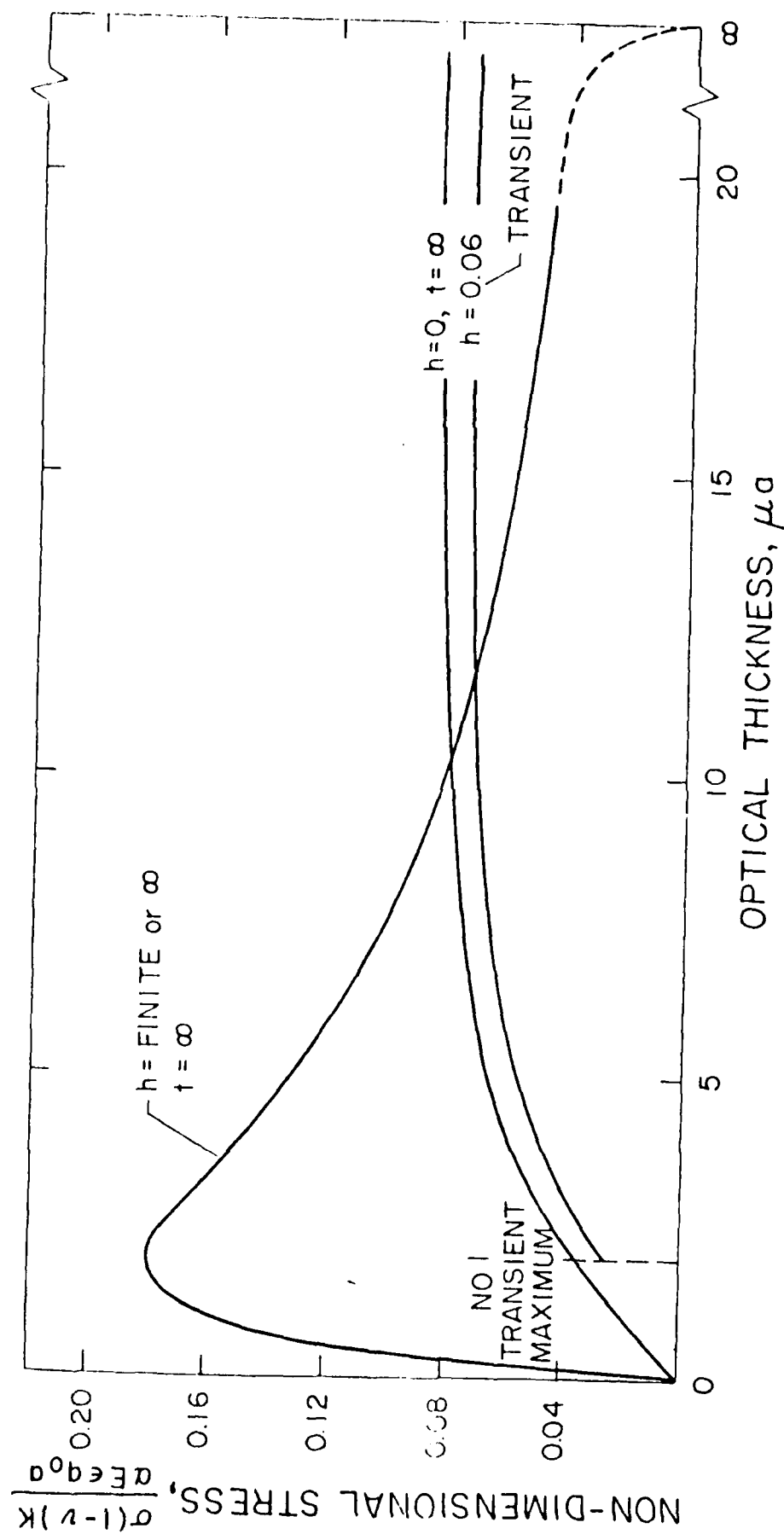


Fig. 6. Variation of maximum tensile thermal stresses as a function of μa in a partially absorbing flat plate subjected to radiation heating and convection cooling at the front face with heat transfer coefficient, $h = 0$, ∞ and finite, $K = 0.3$ watts/cm. 2 and $a = 1$ cm.

CHAPTER VIII

EFFECT OF NATURE OF CONCAVITY OF TEMPERATURE DISTRIBUTION ON POSITION AND SIGN OF MAXIMUM THERMAL STRESS¹

K. Satyamurthy², D. P. H. Hasselman³ and J. P. Singh²

INTRODUCTION

Engineering solutions for the thermal stresses in structures with positive coefficient of thermal expansion, generally indicate that the stresses are compressive (negative) at or near the position in the structure where the temperature has its highest value. Similarly, the tensile stresses generally are found at or near the position of lower temperature. An exception to the above observation was found in a recent analysis [1] of the thermal stresses in a flat plate assymmetrically heated by thermal radiation absorbed in the plate interior. The results of this study showed that the stresses exhibited their maximum tensile value at the surface of the plate being irradiated which is at the highest value of temperature.

In order to provide an explanation for this observation it should be noted that thermo-elastic theory does not predict a unique temperature profile to achieve a thermal stress distribution. The validity of this statement

¹ The results of study were obtained as part of a research program on the thermo-mechanical behavior of brittle structural materials supported by the Office of Naval Research under contract: N00014-78-C-0431.

² Research Associate, Department of Materials Engineering, Virginia Polytechnic Institute and State University, Blacksburg, Virginia 24061.

³ Whittemore Professor of Materials Engineering, Virginia Polytechnic Institute and State University, Blacksburg, Virginia 24061.

can be examined by superposing a zero-stress linear temperature distribution with arbitrary gradient(s) [2] on any other temperature distribution regardless of its nature or source. This shows that any arbitrary relationship between the stress and temperature at any point in a structure can be obtained by the appropriate choice of the temperature gradients.

Such a superposition of linear temperature distribution was not done in the plate subjected to radiation heating referred to above. For this reason, the existence of the maximum tensile thermal stress at the position of highest temperature must be attributed to other reasons. An examination of the general results showed that the temperature distribution exhibited a downward concavity due to the internally absorbed radiation. Such temperature distribution contrasts with the generally concave upward temperature distribution encountered in transient heat transfer for which the exchange of heat between the structure and environment occurs at the surface. It was postulated that the nature of the concavity of the temperature distribution as the result of the internal absorption of the incident radiation, was directly responsible for the finding that the tensile thermal stresses occurred in the hottest part of the plate. The purpose of this communication is to present a simple analysis, which demonstrated the validity of this hypothesis.

ANALYSIS

A thin plate located in the y - z plane and $-a < x < a$ in a rectangular coordinate system will be considered. The plate is subjected to a monotonic distribution of temperature T of the form:

$$T = T_o \left[1 + C \left(\frac{x+a}{2a} \right)^n \right] \quad (1)$$

where T_0 is a reference temperature and C and n are constants. For $C > 0$, the temperature distribution is concave downward or upward for $0 < n < 1$ and $n > 1$, respectively. Similarly, for $C < 0$, the temperature distribution is concave downward or upward for $n > 1$ and $0 < n < 1$, respectively.

The thermal stress distribution can be calculated from [2]

$$\sigma_{y,z} = \frac{\alpha E}{1-\nu} \left[-T + \frac{1}{2a} \int_{-a}^a T dx + \frac{3x}{2a^3} \int_{-a}^a T x dx \right] \quad (2)$$

Substitution of eq. 1 into 2 and integration yields:

$$\sigma_{y,z} = \frac{\alpha E T_0 C}{1-\nu} \left[\frac{1}{n+1} + \frac{3x}{a(n+1)} \left(1 - \frac{2}{n+2} \right) - \left(\frac{x+a}{2a} \right)^n \right] \quad (3)$$

Examination of eqs. 1 and 3 shows that for a concave upward temperature distribution ($C > 0$, $n > 1$ or $C < 0$, $0 < n < 1$), the position of maximum tensile stress coincides with the position of minimum temperature. In contrast for temperature distribution with downward concavity ($C < 0$, $n > 1$ or $C > 0$, $0 < n < 1$), the maximum tensile stress occurs at the position of maximum temperature. For $n = 1$, the temperature distribution is linear with zero thermal stress as expected [2], regardless of the value of C . These results indicate that the direction of the deviation from linearity (i.e. the nature of the concavity) of the temperature distribution controls the relative position of maximum thermal stress and maximum temperature, in agreement with the hypothesis presented earlier.

DISCUSSION

It should be noted that if a symmetric temperature distribution had been chosen the position of maximum tensile thermal stress would have occurred at the position of lowest temperature, regardless of the nature

of the concavity of the temperature distribution. It appears then that for the position of the maximum tensile stress to coincide with the position of the highest temperature, requires an asymmetric concave downward temperature distribution. Such a temperature distribution will result from an asymmetrically distributed non-uniform internal heat generation. This is the case for the aforementioned analysis [1] of the thermal stresses in a plate subjected to asymmetric thermal radiation absorbed within the interior of the plate. Similar effects can be expected for asymmetrically absorbed nuclear radiation or non-uniformly distributed radio-activity.

REFERENCES

1. J. R. Thomas, Jr., J. P. Singh, D. P. H. Hasselman, "Analysis of Thermal Stress Resistance of Partially Absorbing Ceramic Plate Subjected to Asymmetric Radiation, I. Convective Cooling at Rear Surface." J. Amer. Ceram. Soc. (in review).
2. B. A. Boley and J. H. Weiner, Theory of Thermal Stresses. John Wiley and Sons, New York (1960).

CHAPTER IX

EFFECT OF CRACK INTERACTION ON THE FRACTURE INITIATION
AND CRACK PROPAGATION IN BRITTLE CERAMICS SUBJECTED
TO SEVERE THERMAL SHOCK

by

C. Shih, J. P. Singh and D. P. H. Hasselman

Department of Materials Engineering
Virginia Polytechnic Institute and State University
Blacksburg, Virginia 24061, USA

EFFECT OF CRACK INTERACTION ON THE FRACTURE INITIATION
AND CRACK PROPAGATION IN BRITTLE CERAMICS SUBJECTED TO
SEVERE THERMAL SHOCK

C. Shih, J. P. Singh, D. P. H. Hasselman
Department of Materials Engineering
Virginia Polytechnic Institute and State University
Blacksburg, Virginia 24061, USA.

Paper presented at 7th European Thermophysical Conference, Antwerp, Belgium, 30 June - 4 July, 1980.

ABSTRACT

A fracture-mechanical analysis is presented for the effect of crack interaction on the stability and propagation of cracks in brittle ceramic materials subjected to severe thermal stress, based on a model consisting of a flat plate with a rectangular array of columnar and co-linear cracks. It is shown that the combined effect of the interaction between the columnar and co-linear cracks on thermal stress intensity factors and effective elastic behavior of the plate results in a major improvement in thermal stress fracture initiation. However, extensive unstable crack propagation and interaction of closely spaced co-linear cracks will result in complete failure due to crack coalescence.

I. INTRODUCTION

A. General

Engineering structures or components for use at high temperature must rely on ceramics as the only suitable class of materials of construction. Ceramic materials due to their strong ionic or covalent bonding exhibit high melting points, high chemical stability, good creep resistance and other favorable properties.

High-temperature structures or components usually are required to operate under conditions of high thermal stress during transient heating/cooling or steady-state operation. Practical experience has shown that ceramic materials under these conditions are prone to catastrophic failure. One of the principal reasons for this is that in these materials, in contrast to many metals and alloys, thermal stress relaxation by plastic flow cannot readily occur. Furthermore, the corresponding low values of fracture toughness make ceramic materials prone to failure even at moderate thermal stress levels. This low fracture toughness also tends to make such failure completely catastrophic with the crack traversing through the component, rendering it unsuitable for continued satisfactory service. This latter phenomenon is critical since frequently in practice thermal environments can be of such severity that failure even in ceramic materials with optimum thermal stress resistance cannot be avoided. In fact, mate-

rial development in refractory technology usually is more directed toward promoting rapid crack arrest in improving thermal stress fracture, rather than avoiding such fracture altogether.

For this reason, it is imperative that for the purpose of reliable engineering design and selection of materials, the factors and mechanisms which affect thermal stress failure are well understood. Such understanding should cover the initiation of fracture as well as the propagation of cracks following thermal stress fracture. Since thermal stress fracture frequently involves multiple crack formation, the effects of crack interaction should be understood as well. This latter topic represents the objective of the present study. In order to provide a proper framework for the analysis and results to be presented, a brief review of the major variables which control the initiation of thermal stress fracture and crack propagation in brittle ceramics will be given first.

B. Background

Thermal stress fracture of ceramic materials can arise from a wide variety of thermal and mechanical conditions including external constraints, steady-state or transient heat flow, convective or radiative heat transfer, thermal buckling and many others. For the purpose of material selection and the development of reliable design criteria, the role of the pertinent external vari-

ables and material properties which affect thermal stress failure should be carefully assessed. For this reason it is conventional practice in ceramic technology to obtain from the literature or derive expressions for the thermal stresses for a given mode of heat transfer and mechanical boundary conditions. By defining a failure condition, these expressions can be rearranged to yield the maximum thermal environment to which a material can be subjected without incurring the risk of thermal stress failure in terms of the appropriate environmental, geometric and material variables.

As an example, the maximum allowable temperature difference across the thickness of a concentric hollow cylinder undergoing steady-state heat flow can be written (Kingery, 1955; Hasselman, 1978):

$$\Delta T_{\max} = C \sigma_f (1-\nu) / \alpha E \quad (1)$$

where C is a geometric constant related to the ratio of outer to inner radii of the cylinder, σ_f is the tensile fracture stress, ν is Poisson's ratio, α is the coefficient of thermal expansion and E is Young's modulus of elasticity.

As a further example, the maximum sudden change in ambient temperature (ΔT_{\max}) to which a solid cylinder under conditions of convective heat transfer can be subjected (Jaeger, 1945) for Biot number, $\beta = bh/k \ll 1$ is:

$$\Delta T_{\max} \approx 4.95 \sigma_f (1-\nu) k / b h \alpha E \quad (2)$$

where k is the thermal conductivity, h is the heat transfer coefficient and b is radius of cylinder.

Also, the maximum black-body radiation temperature (T_{\max}) to which a spherical body at low initial temperature can be subjected is (Hasselman, 1963):

$$T_{\max} = (5 \sigma_f (1-\nu) k / \alpha E \rho \epsilon b)^{1/4} \quad (3)$$

where ϵ is the absorptivity and ρ is Stefan-Boltzmann constant.

Eqs. 1, 2 and 3 suggest that for a given geometry and body size, ceramic materials with high thermal stress resistance for the three heat transfer conditions referred to above should have high values of the "thermal stress resistance parameters":

$$\sigma_f (1-\nu) / \alpha E ; \sigma_f (1-\nu) k / \alpha E ; \{ \sigma_f (1-\nu) k / \alpha E \epsilon \}^{1/4} \quad (4)$$

These three parameters suggest that ceramic materials with high thermal stress resistance should have high values of tensile strength and thermal conductivity in combination with low values of the coefficient of thermal expansion, Young's modulus of elasticity, absorptivity and Poisson's ratio. A review of the above and many other thermal stress resistance parameters for other thermal environments and failure phenomena was presented recently by one of the present writers (Hasselman, 1978). Important to

note is that these thermal stress resistance parameters are appropriate to the initiation of thermal stress fracture.

The nature of crack propagation in thermally stressed brittle ceramics was analyzed by Hasselman (1969, 1970). A simple mechanical model in the form of a flat plate was considered. The plate was uniaxially constrained from free thermal expansion. The plate had N cracks per unit area of equal size, oriented perpendicularly to the direction of constraint. In the absence of crack interaction the effective Young's modulus (E_{eff}) of the plate was described by:

$$E_{eff} = E_0 (1 + 2\pi Na^2)^{-1} \quad (5)$$

where E_0 is Young's modulus of the crack-free plate and a is the half-length of the crack.

An energy balance analysis, following the well-known Griffith (1920) theory, showed that the critical temperature range (ΔT_{max}) of cooling the plate required for crack instability is:

$$\Delta T_c = (2\gamma/\alpha^2 \pi E a)^{1/2} (1 + 2\pi Na^2) \quad (6)$$

For two values of crack density, fig. 1 shows ΔT_c as a function of crack size indicated by the solid curve. For short crack length such that $2\pi Na^2 \ll 1$, ΔT_c is independent of crack density, and is inversely proportional to $a^{1/2}$. For high crack length such that $2\pi Na^2 \gg 1$, ΔT_c is proportional to $a^{3/2}$, due to the increased compliance of the plate. For a given crack density this

implies that high values of ΔT_c (i.e., high thermal stress resistance) can be achieved by increasing crack length. At first sight this conclusion appears contradictory. However, this effect arises because the failure stress is controlled by a single crack only, whereas the thermal stress is governed by the elastic behavior of the plate, which in turn is governed by the collective effect of all cracks. A minimum in ΔT_c occurs at a crack size, a_m which represents the minimum crack size for which the change in effective Young's modulus becomes significant. At a given value of ΔT the cracks are unstable between two values of crack length.

At ΔT_c for a crack with initial size, $a_o > a_m$ crack propagation occurs in a stable mode. For increase in ΔT to values greater than ΔT_c , the relation between ΔT_c and crack length is given by eq. 6.

For an initial crack size, $a_o < a_m$, the elastic energy release rate exceeds the energy required to create the new crack surfaces. This will cause the crack to propagate in an unstable (dynamic) mode. Following the instability at ΔT_c the crack will accelerate and reach maximum velocity when it reaches a size equal to the higher value of critical crack size. For this reason the crack will continue to propagate until the kinetic energy and additionally released strain energy is converted to fracture energy. For $a_o < a_m$, the final crack size (a_f) which results from this mode of crack propagation can be derived to be (Hasselman, 1971):

$$a_f = (4\pi N a_o)^{-1} \quad (7)$$

The dotted lines in fig. 1 show the value of a_f which results from the unstable crack propagation for cracks with initial size, $a_o < a_m$. As indicated by fig. 1 and eq. 7 the final crack length is an inverse function of the initial crack length.

The results shown in fig. 1 are quantitatively valid only for the particular mechanical model chosen, and assume the absence of crack interaction. Nevertheless on the basis of dimensional grounds the predicted fracture behavior should agree qualitatively with experimental observations. Data in support of this latter conclusion will be reviewed briefly.

Crack sizes in brittle materials are not easily established experimentally. For this reason, it is common practice to monitor the extent of crack propagation indirectly by the measurement of load-bearing ability (tensile strength) after subjecting the ceramic to thermal shock. In order to provide a basis on which to interpret the changes in load-bearing ability, fig. 2 shows the crack length and corresponding changes in strength following thermal shock for unstable and stable crack propagation.

For high-strength materials (i.e. initial crack size, $a_o < a_m$), the unstable mode of crack propagation results in a discontinuity in strength at ΔT_c . Following arrest, the crack is sub-critical so that strength for $\Delta T > \Delta T_c$ remains invariant until at ΔT_c^1 the

crack will resume propagation in a stable mode. Experimental data which support this predicted strength behavior is presented in a number of studies (Hasselman, 1970; Gupta, 1972, Mai and Atkins, 1975).

Since the crack length following thermal stress fracture is inversely proportional to the crack length prior to fracture initiation, the strength retained is expected to be an inverse function of the strength prior to thermal shock, as shown experimentally by Hasselman (1970).

Low strength materials with $a_o > a_m$ will show stable crack propagation and a monotonic decrease in strength as shown by Larson et al. (1974).

The number of cracks participating in the fracture process will govern whether crack propagation will occur in a stable or unstable mode confirmed by Larson and Hasselman (1975).

For unstable crack propagation, the strength loss at ΔT_c will be an inverse function of the number of cracks which form, as shown experimentally by Bertsch et al. (1974).

High densities of small cracks should result in very high thermal stress resistance as confirmed by Rossi (1969) by the comparative thermal shock behavior of hot-pressed magnesium oxide and composites of magnesium oxide with a dispersed phase of tungsten.

The above prediction confirmed by experimental evidence suggests that at least qualitatively the thermal stress fracture and

crack propagation behavior of brittle ceramics is well understood. The possible role of crack interaction will be examined next.

II. EFFECT OF CRACK INTERACTION

Multiple cracks can occur in an almost infinite number of relative orientation. Clearly an exhaustive analysis of all possible interaction effects is beyond the scope of the present study. The specific configuration chosen for an analysis of the effect of crack interaction consists of a flat plate with a rectangular array of co-linear and columnar cracks, shown in fig. 3. For this crack configuration, Delameter et al. (1975) obtained results for the stress intensity factors and effective Young's modulus as a function of co-linear and columnar crack spacings. By uniaxially constraining the plate from free thermal expansion, analogous to the mechanical model used in the previous study, the results of Delameter et al. (1975) can be used to analyze the effect of crack interaction on crack stability and propagation behavior in a thermal stress field. For this purpose, the numerical data of Delameter et al. were curve-fitted to a polynomial which gave an excellent fit with the numerical data to within one percent for the range of values of $0 \leq 2a/d \leq 0.8$ and $0.2 \leq 2a/b \leq 2.0$. All the figures in this section are limited by the extent of the numerical results of Delameter.

The effect of interaction between co-linear cracks should be examined first. For a single row of cracks, fig. 4 shows the critical temperature, ΔT_c required for crack instability as a function of crack size (in arbitrary units) for three values of inter-crack distance. Since for a single row of co-linear cracks, the compliance of an infinite plate is not affected, ΔT_c always decreases with increasing crack length. For short cracks ($a/d < 0.1$) such that interaction effects are absent the $\log \Delta T_c - \log a$ plot has a slope of $-1/2$, as expected. However, as a/d approaches 0.5, the value of the slope decreases very rapidly until at $a/d = 0.5$ the value of ΔT_c goes to zero. This condition occurs because at $a/d = 0.5$ all crack coalesce.

Figure 5 shows ΔT_c for a single column of cracks. For wide crack spacings such that $b/2a \gg 1$, the value for ΔT_c corresponds to the value for a single crack. The $\log \Delta T_c$ vs. $\log a$ curve has a slope which is less than $-1/2$. In fact, as $b/a \rightarrow 1$, the slope becomes positive, strongly indicative of the positive effect on thermal stress resistance due to the interaction between columnar cracks. This effect is not related to the decrease in Young's modulus which for a single column of cracks in an infinite plate is negligible, but is due to the "shielding" between cracks which in effect decreases the stress intensity factor.

To show the combined effect of co-linear and columnar crack interaction, fig. 6 shows ΔT_c for constant co-linear crack spacing d ,

as a function of a/d for a range of values of b/d . In effect, for a given value of crack size, fig. 6 examines the effect of columnar inter-crack spacing on ΔT_c for a plate with a rectangular array of cracks. The data show that ΔT_c is well in excess of the value for a single row of cracks. This effect is due to the combined effect of the "shielding" between columnar cracks and the decrease in effective Young's modulus with decreasing b/d ratio. It should be noted, however, that for a given b/d ratio, ΔT_c goes through a maximum with increasing value of a/d , and approaches zero as $a/d \rightarrow 0.5$. This behavior is in contrast with the results shown in fig. 1, which indicates that in the absence of crack interaction ΔT_c increases monotonically with increasing crack length.

Figure 7 shows similar results for ΔT_c for constant inter-columnar spacing b as a function of a/b for a range of values of d/b . In effect for a given crack size, this shows the effect of co-linear crack spacing on ΔT_c . The results indicate that with decreasing value of d/b , ΔT_c increases over the value of the single column. This effect occurs in spite of the fact that as indicated in fig. 4, ΔT_c decreases with decreasing co-linear crack spacing. The actual increase in ΔT_c is due to the fact that the positive effect of decreasing Young's modulus with decreasing value of d (i.e., increasing crack density) on ΔT_c is greater than the negative effect on ΔT_c due to decrease in co-linear crack spacing, d .

Conclusions similar to those which can be drawn from the data in figs. 6 and 7, are also evident in fig. 8, which shows ΔT_c for constant crack density, $N = (bd)^{-1}$, as a function of $aN^{1/2}$ for a range in values of $dN^{1/2}$. As long as $aN^{1/2}$ remains small, ΔT_c with crack interaction exceeds the corresponding value for the absence of crack interaction as the direct result of the decrease in effective Young's modulus. However, at the higher values of $aN^{1/2}$ and lower values of $dN^{1/2}$, as the result of increased co-linear crack interaction ΔT_c falls below the value of ΔT_c in the absence of crack interaction.

The data presented so far concentrated on the onset of crack propagation. As related earlier, the extent of crack propagation also is a decisive variable in assessing the thermal shock resistance of brittle ceramics. The interaction between cracks also is expected to affect the final crack size (a_f). Values for a_f were calculated on the assumption that all the elastic energy released during crack propagation is converted to surface fracture energy. The results obtained are shown in fig. 9 for a number of values of $dN^{1/2}$ of fig. 8. Primarily as the result of the columnar crack interaction, the final crack length is less than the corresponding one in the absence of crack interaction. This latter conclusion is valid only as long as the final crack length remains small relative to the co-linear crack spacing. If, however, the final crack length approaches the value of the co-linear crack spacing,

an interesting effect should occur, indicated by the curve for $dN^{1/2}=2$. The dotted part of this curve which falls below the crack stability curve, ΔT_c , denotes the position of crack arrest for a crack with initial size $a_o < a_m$. The crack is sub-critical only as long as it falls below the corresponding solid curve (ΔT_c) for continued propagation in a stable mode. This sub-criticality disappears at a value of final critical crack size, a_f at which solid curve for ΔT_c and the dotted curve for crack arrest intersect. For this reason, if the final crack length would exceed the values indicated by the point of intersection of the dotted and the solid curves, the crack will again be unstable and will continue to propagate until complete crack coalescence occurs. In other words the material will completely disintegrate. The same effect will occur for stable crack propagation whenever crack length exceeds the value corresponding to the peak in ΔT_c vs. a curve. These latter results contrast with those obtained for the absence of crack interaction, which do not predict this fracture mode.

These above results have important implication for the retention of load-bearing ability of brittle ceramics subjected to thermal shock and in which strong crack interaction effects are present. Such strength behavior is shown schematically in fig. 10. Curve (a) results from the extensive propagation of an initially very short crack (in a high-strength material) which

due to co-linear crack interaction will not exhibit crack arrest. Curve (b) indicates the strength behavior of a material in which the crack arrests to be subcritical followed by stable crack propagation and crack coalescence resulting in complete disintegration of the material. Curve (c) corresponds to a crack which propagated in a stable mode until crack coalescence and complete failure. These writers are not aware of experimental data which demonstrate this behavior. A search of the literature for such data or an experimental research program to establish such data is recommended as highly valuable.

III. SUMMARY AND CONCLUSIONS

The effect of crack interaction on the initiation of thermal stress fracture and resulting crack propagation in brittle materials was investigated using mechanical model consisting of a flat plate with a rectangular array of co-linear and columnar cracks. The general results indicate that the crack interaction in combination with changes in the effective elastic behavior of the plate, has a beneficial effect on thermal stress resistance. Only when the crack sizes approach the co-linear crack spacing, thermal stress resistance is decreased. Implications of these results on the retention of the load-bearing ability of brittle ceramics fractured by thermal shock are discussed.

ACKNOWLEDGMENTS

This study was conducted as part of a research program on the thermal-mechanical and thermal behavior of structural ceramics supported by the Office of Naval Research under contract N00014-78-C-0431.

REFERENCES

- Bertsch B E, Larson D R and Hasselman D P H, 1974 J. Am. Ceram. Soc. 57 235-236
- Delameter W R, Herrmann G and Barnett D M, 1975 J. Appl. Mech., Trans. ASME 42 74-80
- Griffith A A, 1920 Phil. Trans. Roy. Soc. Lond. A221 163-198
- Gupta T K, 1972 J. Am. Ceram. Soc. 55 249-53
- Hasselman D P H, 1963 J. Am. Ceram. Soc. 46 229-34
- Hasselman D P H, 1969 J. Am. Ceram. Soc. 52 600-604
- Hasselman D P H, 1970 J. Am. Ceram. Soc. 53 491-495
- Hasselman D P H, 1971 Int. J. Fract. Mech. 7 157-161
- Hasselman D P H, 1978 Ceramurgia International 4 147-150
- Jaeger J C, 1945 Philos. Mag. 36 418-428
- Kingery W D, 1955 J. Am. Ceram. Soc. 38 3-15
- Larson D R, Coppola J A and Hasselman D P H, 1974 J. Am. Ceram. Soc. 57 417-421
- Larson D R and Hasselman D P H, 1975 J. British Ceram. Soc. 74 59-65
- Mai Y W and Atkins A G, 1975 J. Am. Ceram. Soc. 54 593
- Rossi R C, 1969 Bull. Am. Ceram. Soc. 48 736-737

- Fig. 1. Crack stability and propagation behavior for a rigidly held thermally stressed flat plate for two values of density of non-interacting cracks (Hasselman, 1971)
- Fig. 2. Crack propagation and strength behavior for (A) and (B): unstable and (C) and (D): stable mode of propagation of non-interacting cracks under conditions of thermal shock (Larson et. al., 1974)
- Fig. 3. Flat plate with rectangular array of cracks for the analysis of the effect of crack interaction on the thermal fracture of brittle ceramics
- Fig. 4. Effect of colinear crack-interaction on the critical temperature difference for crack instability
- Fig. 5. Effect of columnar crack-interaction on the critical temperature difference for crack instability
- Fig. 6. Combined effect of colinear and columnar crack-interaction on the critical temperature difference for constant colinear crack spacing
- Fig. 7. Combined effect of colinear and columnar crack-interaction on the critical temperature difference for constant columnar crack spacing
- Fig. 8. Combined effect of colinear and columnar crack-interaction on the critical temperature difference for crack instability for a range of value of colinear and columnar crack spacing with a constant value of crack density, N
- Fig. 9. Effect of crack interaction on the extent of crack propagation following unstable crack propagation
- Fig. 10. Predicted strength behavior of brittle ceramics as a function of the severity of thermal shock for stable and unstable propagation of interacting cracks

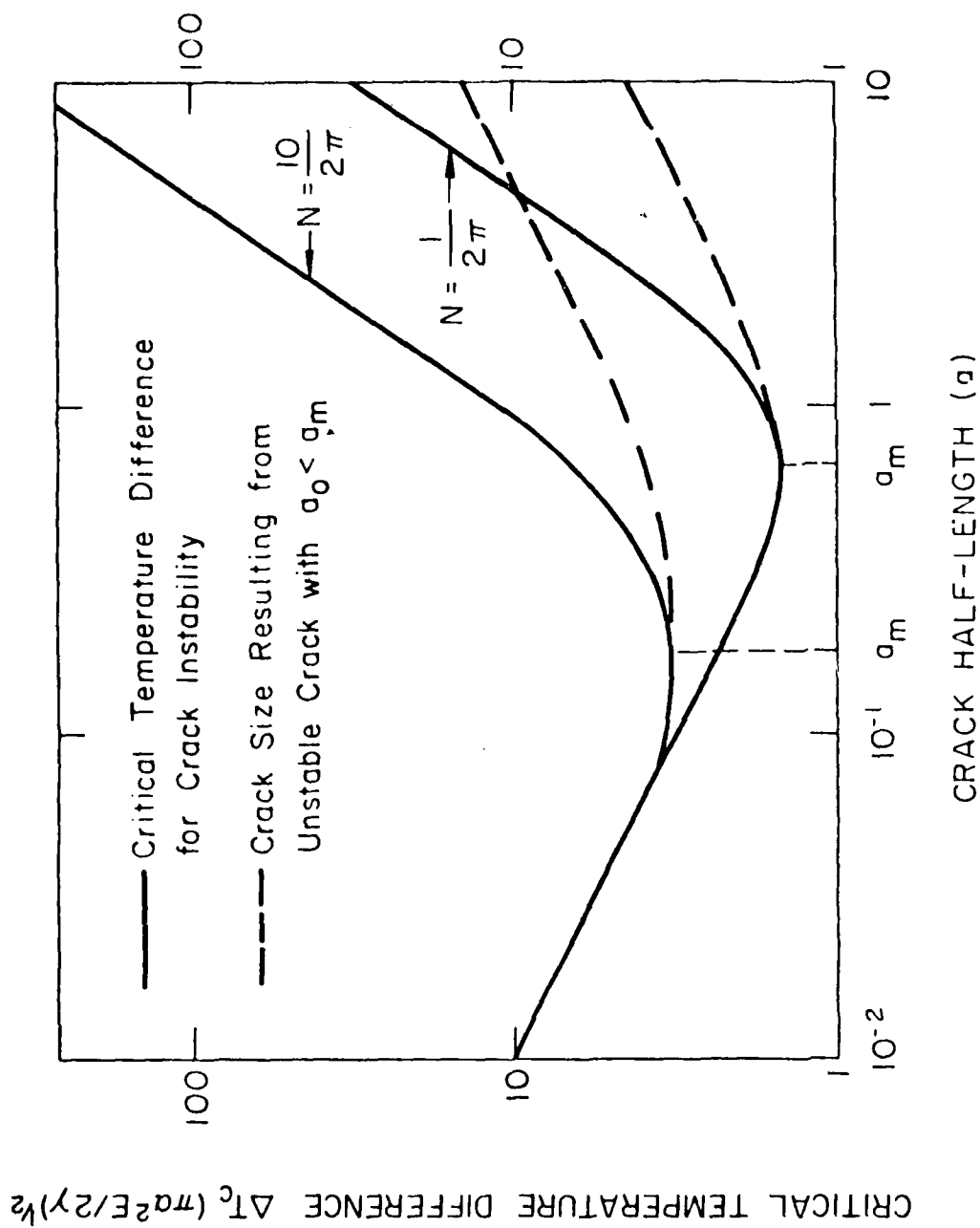


Fig. 1. Crack stability and propagation behavior for a rigidly held thermally stressed flat plate for two values of density of non-interacting crack (Hasselman, 1977).

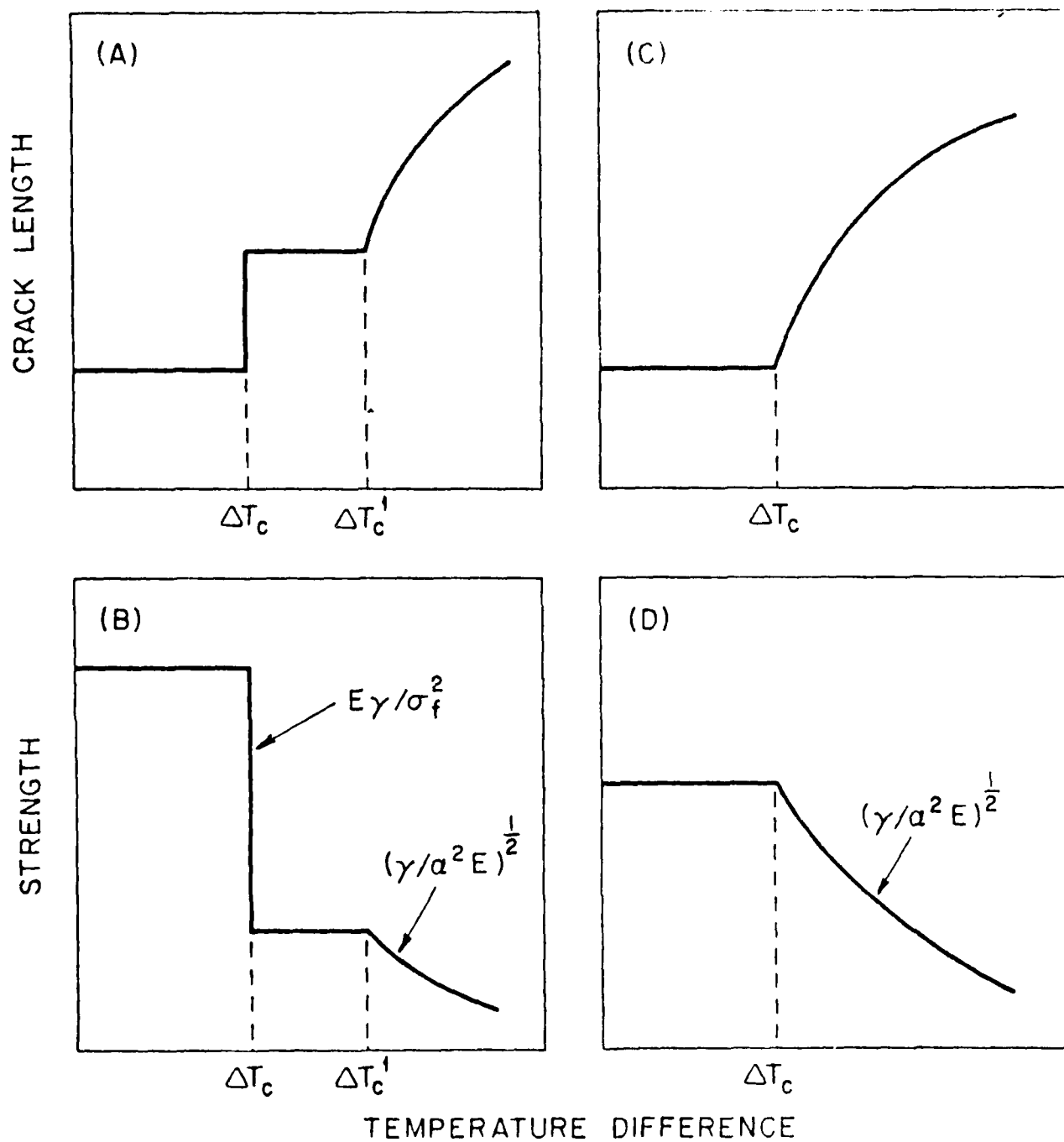


Fig. 2. Crack propagation and strength behavior for (A) and (B): unstable and (C) and (D): stable mode of propagation of non-interacting cracks under conditions of thermal shock (Larson et al., 1974)

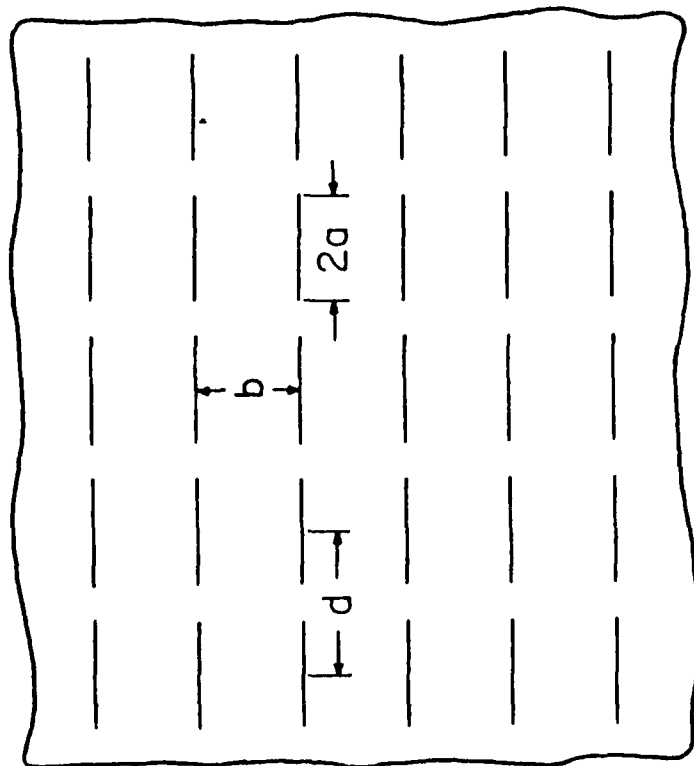


Fig. 3. Flat plate with rectangular array of cracks for the analysis of the effect of crack interaction on the thermal fracture of brittle ceramics

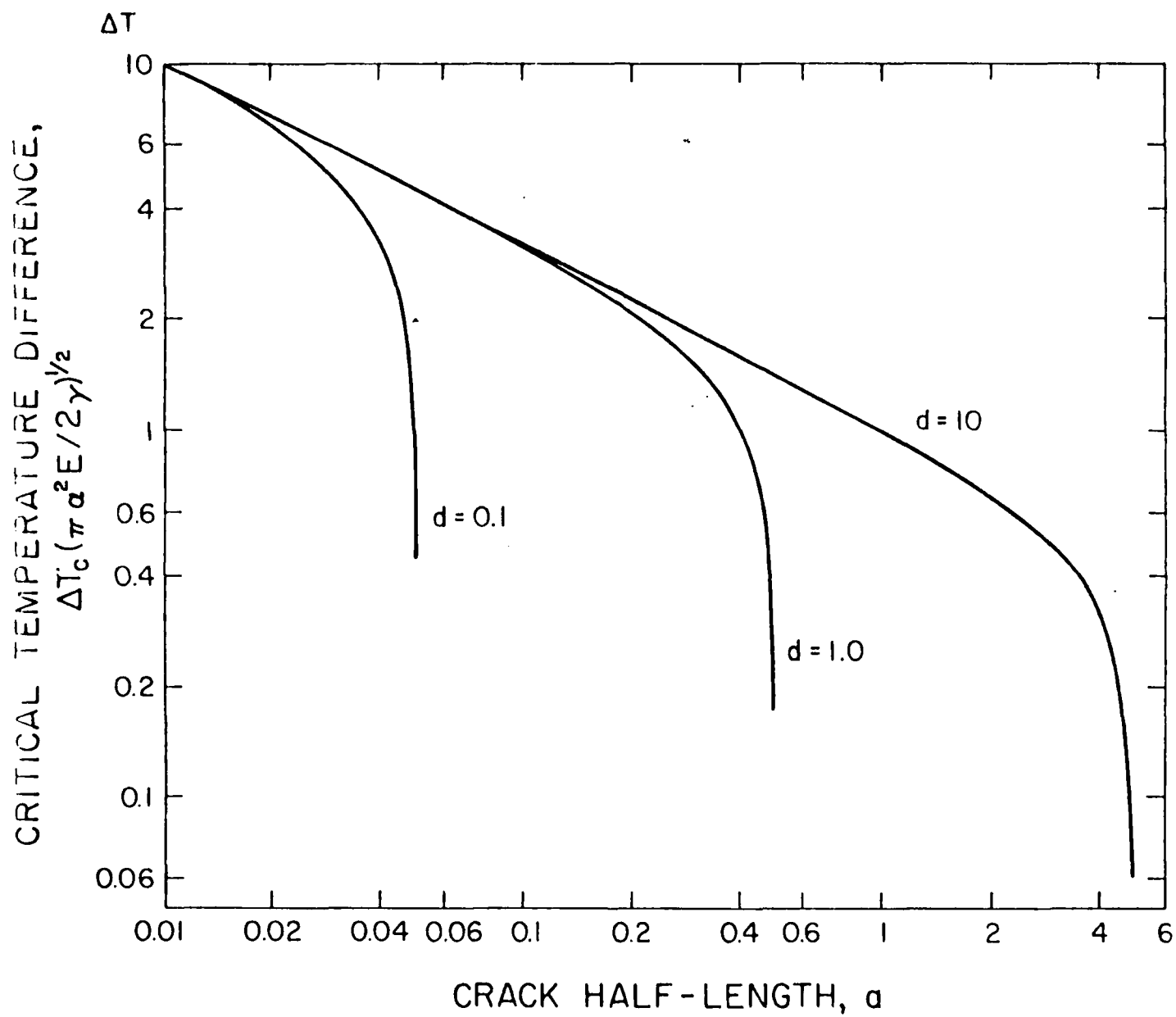


Fig. 4. Effect of co-linear crack-interaction on the critical temperature difference for crack instability

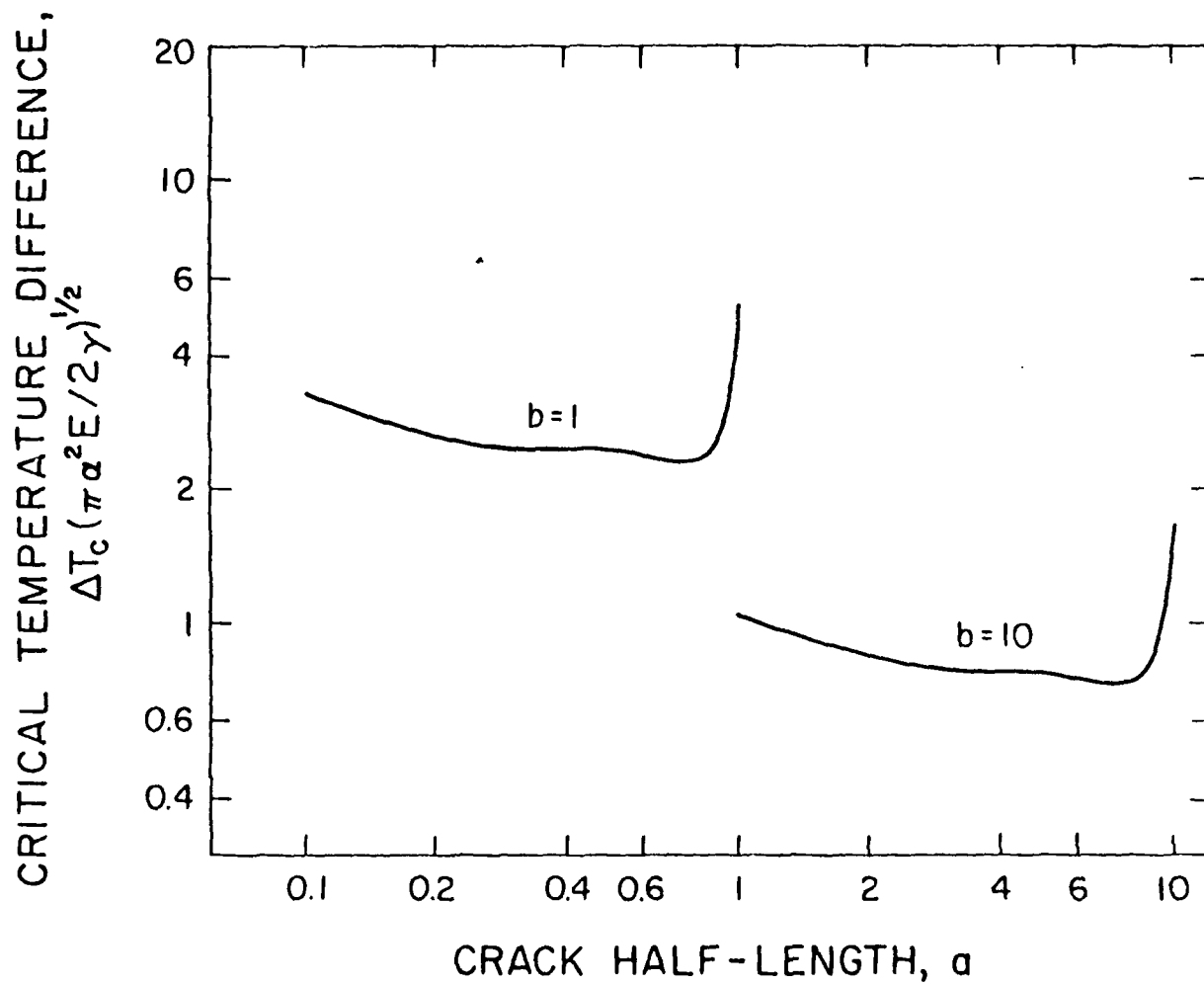


Fig. 5. Effect of columnar crack-interaction on the critical temperature difference for crack instability

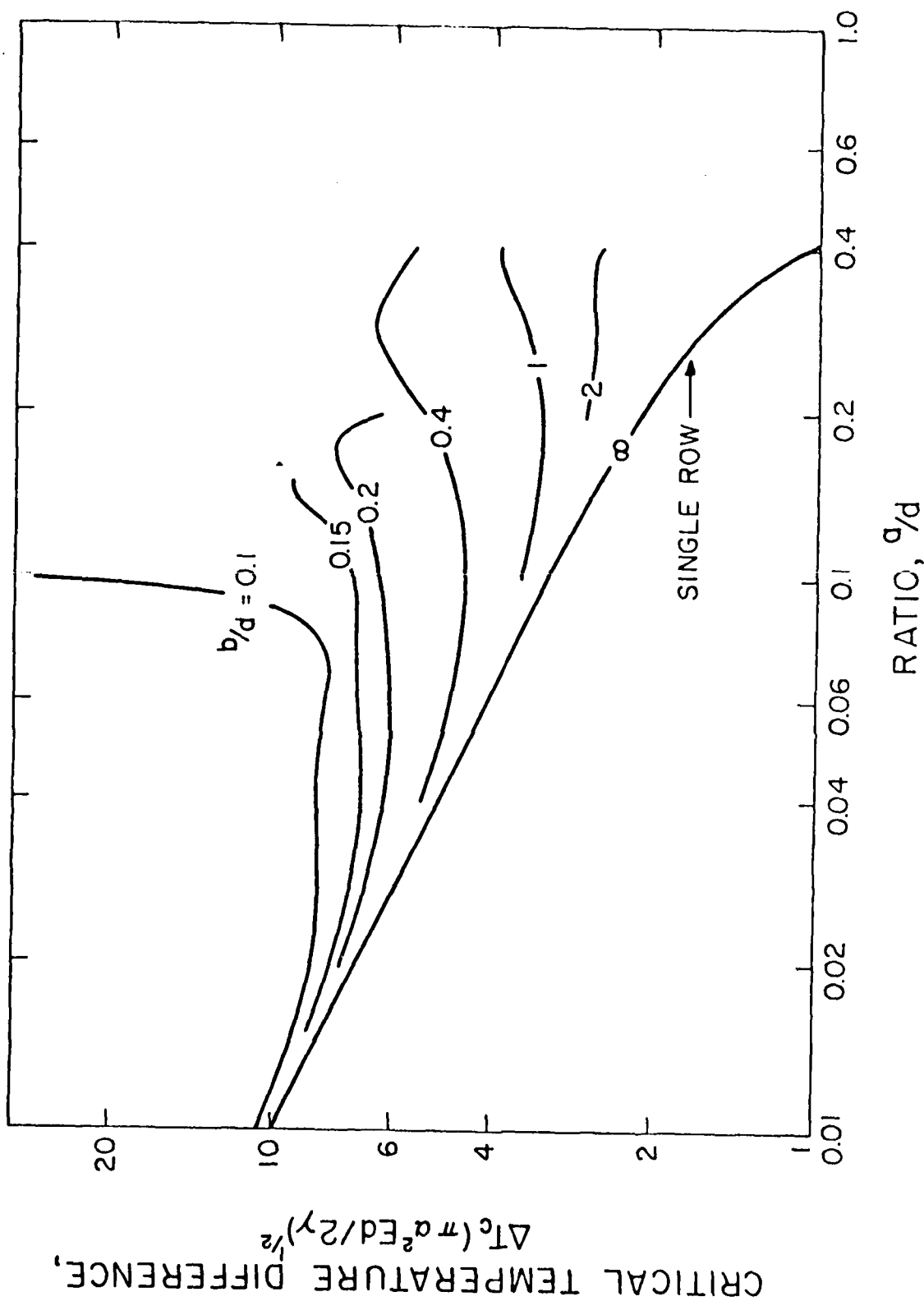


Fig. 6. Combined effect of colinear and columnar crack-interaction on the critical temperature difference for constant colinear crack spacing

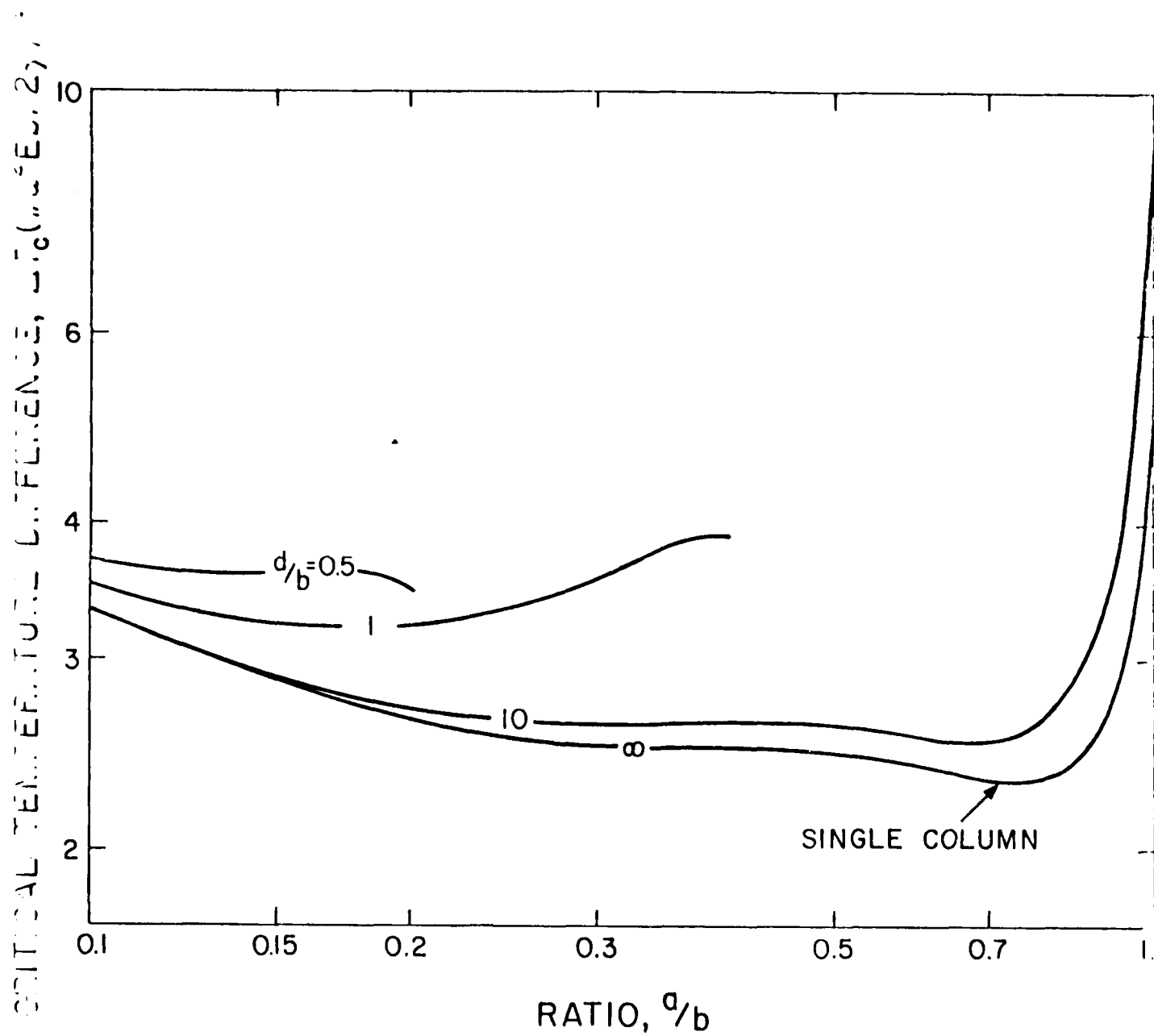


Fig. 7. Combined effect of colinear and columnar crack-interaction on the critical temperature difference for constant columnar crack spacing

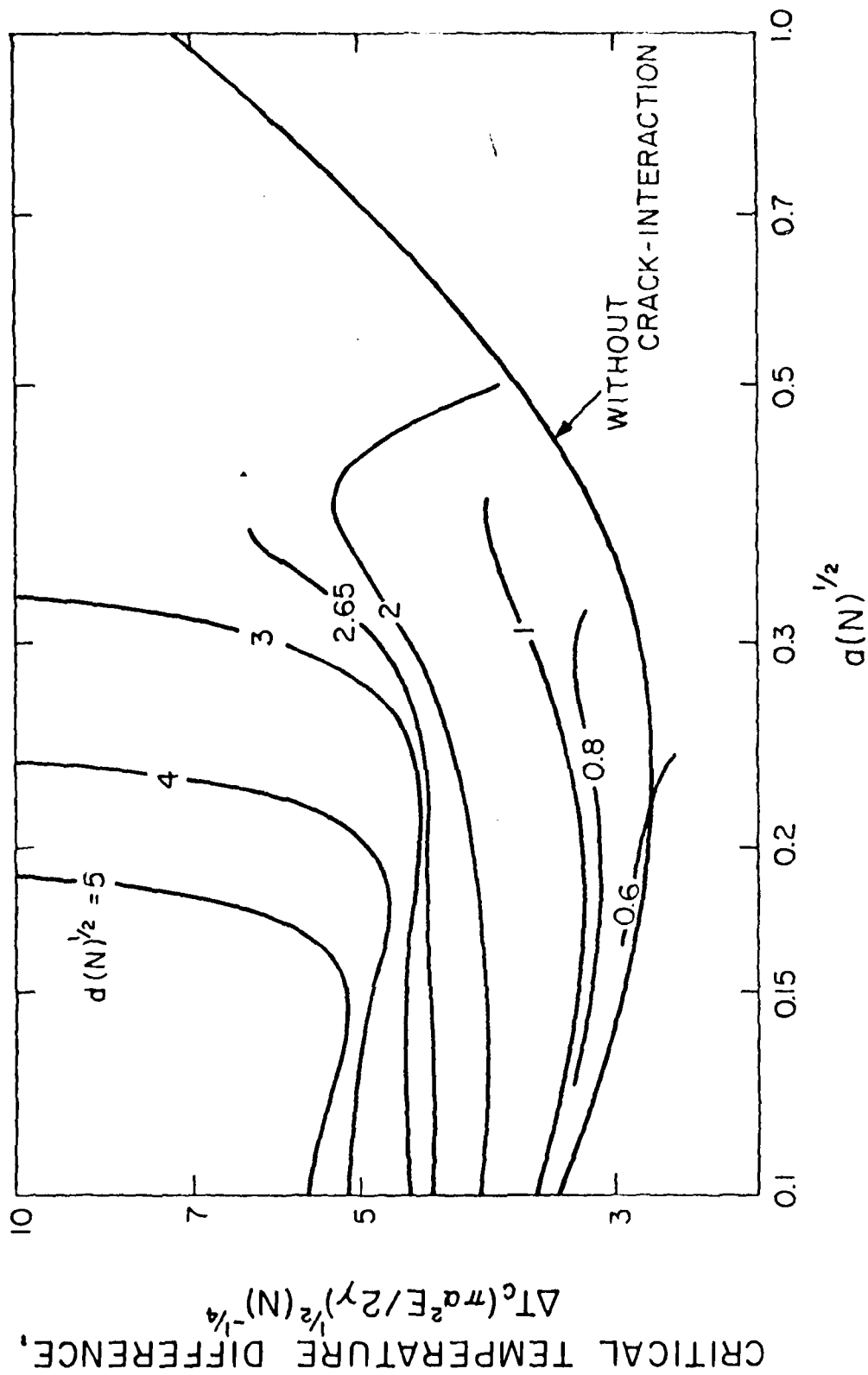


Fig. 8. Combined effect of colinear and columnar crack-interaction on the critical temperature difference for crack instability for a range of values of colinear and columnar crack spacing with a constant value of crack density, N

CRITICAL TEMPERATURE DIFFERENCE,
 $\Delta T_c (\pi \alpha^2 E / 2 \gamma)^{1/2} (N)^{-1/4}$

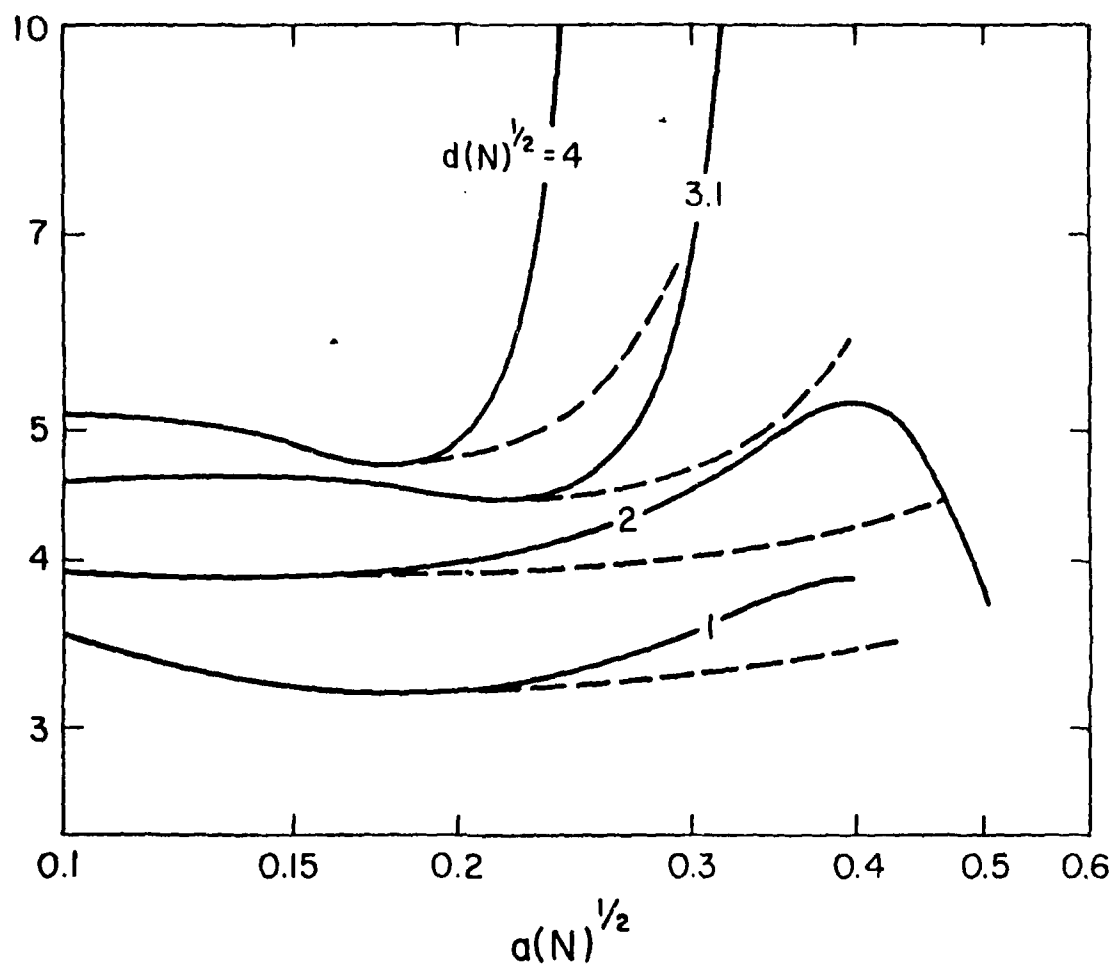


Fig. 9. Effect of crack interaction on the extent of crack propagation following unstable crack propagation

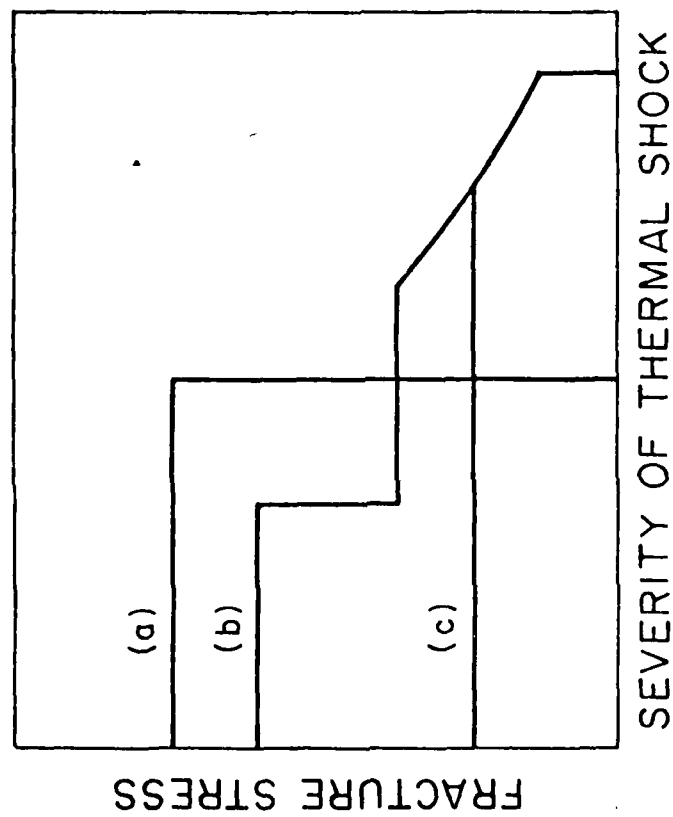


Fig. 10. Predicted strength behavior of brittle ceramics as a function of the severity of thermal shock for stable and unstable propagation of interacting cracks

CHAPTER X

STRESSES DUE TO THERMAL TRAPPING IN SEMI-ABSORBING MATERIALS SUBJECTED TO INTENSE RADIATION

J. P. Singh, J. R. Thomas, Jr., and D. P. H. Hasselman

Departments of Materials and Mechanical Engineering
Virginia Polytechnic Institute and State University
Blacksburg, Virginia 24061

ABSTRACT

Analytical results are presented for the thermal stresses resulting from "thermal trapping" in semi-absorbing materials subjected to symmetric and asymmetric radiation heating and convective cooling with finite heat transfer coefficient, h . The transient stresses during heat-up in both cases were found to be an inverse function of the heat transfer coefficient, h , and increase monotonically with the optical thickness, μa . In contrast, the steady state stresses were independent of h and exhibited a maximum at $\mu a \approx 1.3$ for symmetric heating and at $\mu a = 2$ for asymmetric heating with zero stresses at $\mu a = 0$ and ∞ . For the symmetrically heated plate, the transition from the transient to the steady-state condition involved a reversal in the sign of thermal stress at any position. For the asymmetrically heated plate the steady state maximum tensile thermal stresses occur at the position of the highest temperature, i.e. the front surface.

INTRODUCTION

Many engineering structures such as aerospace vehicles and concentrating solar collectors are subjected to high intensity radiant heat fluxes. In order to withstand the high temperature involved, such structures must be constructed of materials with high melting point and good mechanical properties. Unfortunately, such materials tend to be brittle and are susceptible to catastrophic failure under the influence of transient and steady state thermal stresses resulting from non-linear temperature distribution^{1,2}. Therefore, for the selection of the optimum material and reliable

engineering design, it is necessary to analyze the thermal stresses arising from radiation heating and understand the variables which control their magnitude.

The analysis of thermal stress failure of an opaque material subjected to black body radiation was performed by Hasselman³ some time ago. Subsequently, the effect of the spectral dependence of absorption coefficient was taken into account to include materials completely transparent below and opaque above a given wavelength⁴. For many materials, however, the incident radiation may be absorbed throughout the thickness and depending upon the absorption properties, it may result in so called "thermal trapping" effect in which the interior temperature of the body may exceed the ambient temperature. Thermal stresses in a flat plate due to this type of heat transfer were analyzed recently by Hasselman et. al.⁵ for symmetric radiation heating with convective cooling for two limiting values of heat transfer coefficient, h , equal to zero and infinity. Subsequently two follow-up studies by Thomas et. al.⁶ and Singh et. al.⁷ included the case of symmetric and asymmetric radiation heating and convective cooling with finite values of h .

The purpose of this paper is to review and report the main results for stresses in the latter two studies. For further details, the reader is referred to the original papers.^{6,7}

ANALYSIS

The analysis of thermal stresses in the flat plate first required obtaining the temperature distribution, which was subsequently utilized to calculate the thermal stresses. In this analysis the reflectivity of the material was assumed to be low and hence the effect of multiple internal reflections was neglected. It was also assumed that the maximum value of the stress in the plate will be reached before the temperature becomes sufficiently high that the effect of re-emission must be taken into account⁸. The validity of this latter assumption can easily be substantiated with numerical examples^{5,6}. Finally it was assumed that the emissivity and absorptivity of the plate are independent of wavelength. However, the spectral dependence of these properties can easily be incorporated in the analysis, if needed.

The general analytical approach along with the heating and cooling conditions are as follows:

A. Symmetric Radiative Heating and Convective Cooling

The rate of internal heat generation (g'') within the plate subjected to symmetric normally incident radiation q_0 is given by:

$$g''' = 2\mu\epsilon\sigma_0 e^{-\mu a} \cosh(\mu x) \quad (1)$$

where μ is the absorption coefficient, ϵ is the emissivity ($\epsilon=1-r$, where r is the reflectivity), a is the half thickness of the plate and x is the through-the-thickness coordinate with $x=0$ at the center of the plate.

The temperature solutions were obtained by solving the differential equation⁹:

$$\frac{\partial^2 T}{\partial x^2} + g'''(x)/k = (1/\kappa) \frac{\partial T}{\partial x} \quad (2)$$

where k is the thermal conductivity, t is the time and κ is the thermal diffusivity.

The initial and boundary conditions were:

$$T(x,0) = T_0; \quad \frac{\partial T}{\partial x}(0,t) = 0 \quad (3)$$

$$\frac{\partial T}{\partial x}(a,t) = -\frac{h}{k} \{T(a,t) - T_0\} \quad (4)$$

$$\frac{\partial T}{\partial x}(-a,t) = \frac{h}{k} \{T(-a,t) - T_0\} \quad (5)$$

where h is the convective heat transfer coefficient.

The solution of temperature T , thus obtained from differential equation (2), was utilized to obtain the expressions for thermal stress from¹⁰:

$$\sigma_{y,z} = \frac{\alpha E}{1-\nu} \left[-T + \frac{1}{2a} \int_{-a}^a T dx + \frac{3x}{2a^3} \int_{-a}^a T x dx \right] \quad (6)$$

which yields:

$$\sigma_{y,z} = \frac{-\alpha E}{1-\nu} \sum_{n=0}^{\infty} B_n(t) \cos(\lambda_n x) + \frac{\alpha E}{a(1-\nu)} \sum_{n=0}^{\infty} \frac{B_n(t)}{\lambda_n} \sin(\lambda_n a) \quad (7)$$

where λ_n are the roots of the transcendental equation

$$\lambda_n \tan(\lambda_n a) = h/k$$

and

$$B_n(t) = \frac{G_n}{\kappa \lambda_n^2} (1 - e^{-\kappa \lambda_n^2 t})$$

$$\text{with } G_n = \frac{2\kappa\mu\epsilon q_0 e^{-\mu a}}{N_n k} \left[\frac{\mu \cos(\lambda_n a) (e^{\mu a} - e^{-\mu a}) + \lambda_n \sin \lambda_n a (e^{\mu a} + e^{-\mu a})}{\mu^2 + \lambda_n^2} \right]$$

$$\text{and } N_n = a + \frac{h}{\lambda_n^2 k} \cos(\lambda_n a)$$

B. Assymmetric radiation Heating and Convective Cooling

In this case, the radiation q_0 is normally incident to only one face of the plate at $x = -a$ and the plate is cooled by convection at $x = a$. The intensity of internal heat generation (g''') within the plate can be shown to be:

$$g'''(x) = \mu\epsilon q_0 e^{-\mu(a+x)} \quad (8)$$

The initial and boundary conditions are:

$$T(x,0) = T_0; \quad \frac{\partial T}{\partial x}(-a,t) = 0 \quad (9)$$

$$-k \frac{\partial T}{\partial x}(a,t) = h[T(a,t) - T_0] \quad (10)$$

The temperature solutions were obtained by solving the differential equation (2) subjected to the conditions (9) and (10). Similar to case A, the temperature solution, thus obtained, was utilized to find out the expression for thermal stress. The thermal stress in this case is given by:

$$\begin{aligned} \sigma_{y,z} = & \frac{-\alpha E}{1-\nu} \sum_{n=0}^{\infty} B_n(t) \cos\{\lambda_n (x+a)\} \\ & + \frac{\alpha E}{2a(1-\nu)} \sum_{n=0}^{\infty} \frac{B_n(t)}{\lambda_n} \sin(2\lambda_n a) \\ & + \frac{3\alpha\epsilon E}{2a(1-\nu)} \sum_{n=0}^{\infty} B_n(t) \left[\frac{\sin(2\lambda_n a)}{a\lambda_n} + \frac{1}{a^2\lambda_n^2} \cos(2\lambda_n a) - \frac{1}{a^2\lambda_n^2} \right] \end{aligned} \quad (11)$$

where λ_n are the roots of the transcendental equation

$$\lambda_n \tan(2\lambda_n a) = h/k$$

$$\text{and } B_n(t) = G_n [1 - e^{-\kappa\lambda_n^2 t}] / \kappa\lambda_n^2$$

$$\text{with } G_n = \frac{\kappa q_0 \epsilon \mu}{N_n k} \left\{ \frac{\mu + e^{-2\mu a} [\lambda_n \sin(2\lambda_n a) - \mu \cos(2\lambda_n a)]}{\mu^2 + \lambda_n^2} \right\}$$

$$\text{and } N_n = \frac{1}{2\lambda_n} [\sin(2\lambda_n a) \cos(2\lambda_n a) + 2\lambda_n a]$$

NUMERICAL RESULTS AND DISCUSSION

For the convenience of data presentation, the results will be presented in non-dimensional form as follows:

The non-dimensional time:

$$t^* = \kappa t / a^2 \quad (12)$$

the non-dimensional temperature:

$$T^* = (T - T_0) k / \epsilon q_0 a \quad (13)$$

and the non-dimensional stress:

$$\sigma^* = \sigma(1-\nu)k / \alpha E \epsilon q_0 a \quad (14)$$

For simplicity, the quantities t^* , T^* and σ^* hereafter will be referred to as time, temperature and stress, respectively.

Figure 1 shows the thermal stresses in the surface and the center of a symmetrically heated plate as a function of time for a range of values for h/k with an arbitrarily chosen value of the optical thickness $\mu a = 3$. Stresses reach the steady state value after an initial transient. For a given optical thickness μa , the value of the steady state stress is independent of h . This is so because the steady state temperature profile within the plate is independent of the heat transfer coefficient h , even though the magnitude of the temperature for a given profile is an inverse function of the heat transfer coefficient. The values of the maximum transient stress, however, decrease with increasing h in contrast to many literature solutions for transient thermal stresses in convection heat transfer environment where the thermal stresses increase with increasing value of h .

Another noteworthy point in figure 1 is the change in the sign of the thermal stresses in the plate with time for finite values of h/k . At small values of time the surface stress is compressive whereas the stress in the center is tensile. However, at longer times the stresses reverse their sign and become tensile and compressive in the surface and the center, respectively. This

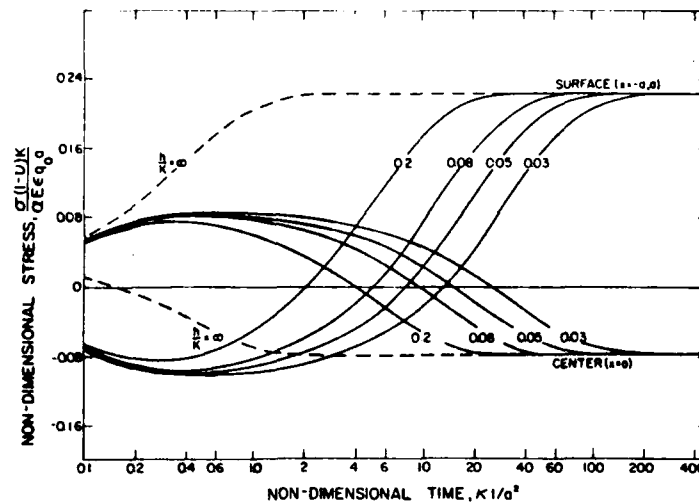


Fig. 1. Maximum thermal stress as a function of time in a partially absorbing flat plate symmetrically heated by thermal radiation and cooled by convection for various values of h/k (cm^{-1}) with optical thickness $\mu_a=3$ and $a=1$ cm.

phenomenon is a result of the non-uniform heat generation inside the plate and the associated "thermal trapping" effect. Due to a larger portion of the incident radiation being absorbed in the surface, initially the surface is at higher temperature than the interior. During this time period, the heat loss from the surface by convection is very small because of the low surface temperature in combination with finite value of h and the heat flows primarily from the surface to the interior. This results in a temperature distribution which causes a compressive stress in the surface and tensile stress in the center. However, after a long period of time ($t \rightarrow \infty$) the surface gets hot with an appreciable amount of heat loss by convection which eventually will be equal to the incident radiative heat flux at steady state. Under this condition, due to the internal heat generation, the interior of the plate will be at higher temperature than the surface resulting in a tensile stress in the surface and a compressive stress in the center of the plate. However, as $h/k \rightarrow \infty$, no stress reversal in the surface takes place because the surface temperature remains constant (equal to the ambient temperature) at all times resulting in tensile surface stress for $t > 0$.

For the symmetrically heated plate, figures 2 and 3 show the maximum values of transient and steady state stress as a function of optical thickness, μ_a . It is interesting to note that the maximum value of the transient stress increase with optical thickness whereas the steady state stress exhibits a maximum at $\mu_a=1.3$

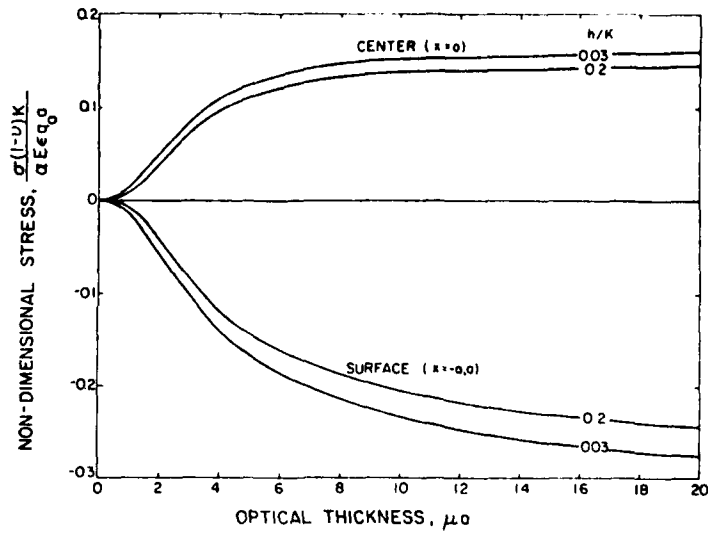


Fig. 2. Magnitude of maximum transient thermal stresses as a function of optical thickness μ_0 in partially absorbing flat plate symmetrically heated by thermal radiation and cooled by convection for various values of h/k (cm^{-1}) with $a=1$ cm.

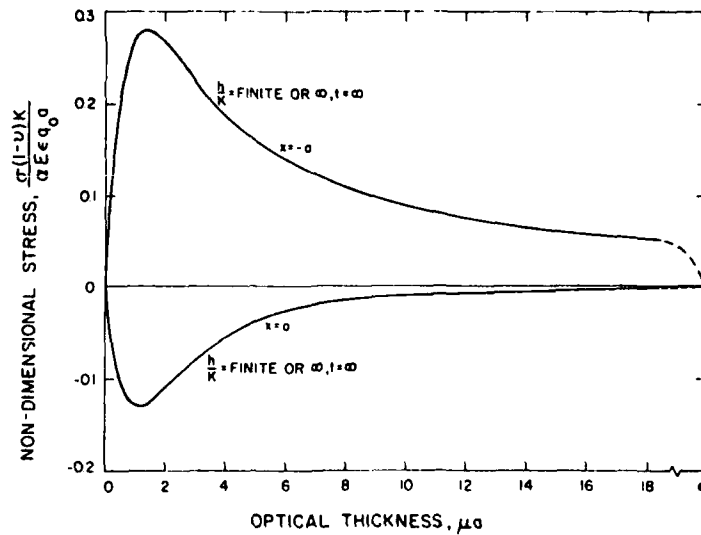


Fig. 3. Magnitude of maximum steady state thermal stresses as a function of optical thickness μ_0 in a partially absorbing flat plate symmetrically heated by thermal radiation and cooled by convection for various values of h/k (cm^{-1}) with $a=1$ cm.

and approaches zero at $\mu a = 0$ and ∞ . For $\mu a = 0$, no heat is absorbed, resulting in zero stress. However, for $\mu a \rightarrow \infty$, although the heat is transmitted through the plate, the steady state temperature profile is linear resulting in zero stress at $t = \infty$. At $\mu a = 1.3$, the non-uniformity in the internal heat generation and the associated thermal trapping effects are maximum resulting in the maximum stress.

For an assymmetrically heated plate, figure 4 shows the values of maximum tensile thermal stress as a function of time for various values of h/k with an arbitrarily chosen value of $\mu a = 3$. Similar to figure 1, the stress reaches a constant steady state value independent of h and the value of maximum transient stress is an inverse function of h .

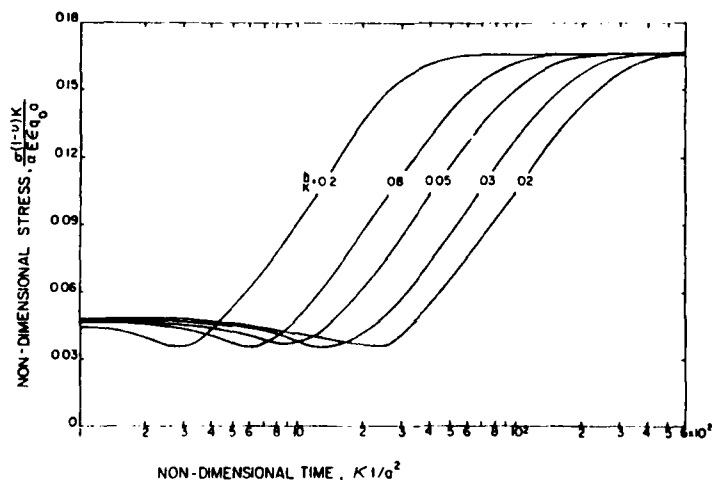


Fig. 4. Maximum tensile thermal stress as a function of time in a partially absorbing flat plate assymmetrically heated in front by thermal radiation and cooled at the rear surface by convection for various values of h/k (cm^{-1}) with $\mu a = 3$ and $a = 1$ cm.

Figure 5 shows the spatial distribution of the steady state tensile stress ($t \rightarrow \infty$) in the assymmetrically heated plate. It is important to note that the maximum tensile stress occurs in the front face ($x = -a$) of the plate which is obviously at the highest temperature. This initially unexpected result was shown to be due to a concave downward temperature distribution¹¹ as the direct result of an assymmetrically non-uniform internal heat generation. This temperature distribution contrasts with the usual concave upward temperature distribution found in many cases where the heat

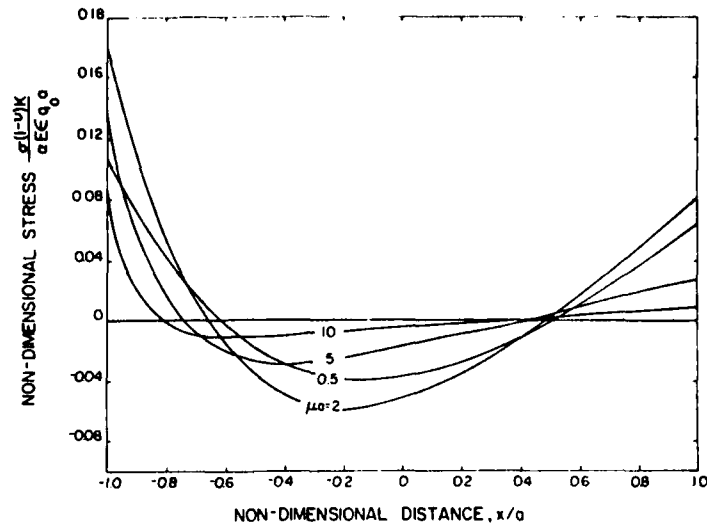


Fig. 5. Spatial distribution of steady state thermal stresses in a partially absorbing flat plate asymmetrically heated in front by thermal radiation and cooled at the rear surface by convection for various values of μa with $h/k(\text{cm.}^{-1})$ finite and $a = 1 \text{ cm.}$

is exchanged only at the outside boundaries of the structure. For this latter case, the maximum tensile stresses frequently occur at or near the position of the lowest temperature.

Figure 6 summarizes the values of maximum tensile transient and steady state thermal stress as a function of μa in the asymmetrically heated plate. Similar to the observation made for symmetric heating case (Figures 2 and 3) the steady state stress exhibits a maximum, which occurs at $\mu a = 2$ because of the maximum thermal trapping effect. However, the maximum transient stress for finite value of h is a monotonically increasing function of μa and will fall between the stress plots for $h=0$ and $h=\infty$ (Figure 6). From Figures (4) and (6), it is obvious that for $10.7 < \mu a < \infty$, the maximum transient stress is greater than the corresponding maximum steady state stress and for $0 < \mu a < 10.7$, the converse is true.

A comparison of the results for thermal stresses in the symmetrically and asymmetrically heated flat plates indicates that the nature of the stress profiles in both cases are qualitatively similar (Figures 1-6). However, the magnitude of the maximum stress in case of symmetric heating is higher than that in case of asymmetric heating. The lower value of stress in case of asymmetric heating is due to the fact that the non-uniform thermal expansion can be

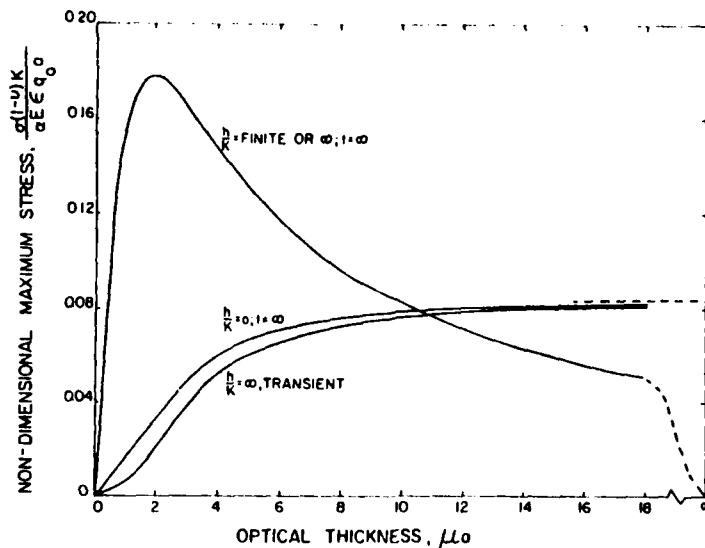


Fig. 6. Magnitude of maximum tensile thermal stresses as a function of μ_0 in a partially absorbing flat plate assymetrically heated in front by thermal radiation and cooled at the rear surface by convection with $h/k(\text{cm.}^{-1})$ finite and $a = 1 \text{ cm.}$

partly accommodated by bending which is not the case in symetric heating.

The above discussions have the following implications: First, it is important to note that although the steady state stress is zero at $\mu_0=0$ and ∞ , the magnitude of stress could be significant for the intermediate values of μ_0 . Therefore, it is preferable to have a transparent material to avoid thermal stress fialure. However, this criterion for material selection may not be compatible with other performance criteria. For example, for high efficiency of the solar collectors, it is desirable to have high values of the absorption coefficient and emissivity to keep the amount of transmitted and reflected radiation to a minimum. Clearly a compromise between high collector efficiency and high thermal stress resistance will have to be made.

Finally, the observation of the maximum tensile thermal stress in the hottest part (front face) of the assymmetrically heated plate could be very critical for failure by the stress corrosion mechanism. Stress corrosion, which could be promoted by environmental conditions, is generally a thermally activated process and is expected to increase with stress and temperature. Therefore, in addition to having low thermal stress, it is important to maintain low temperature levels in the plate to ensure high thermal stress resistance and long life. Thus, care must be taken in selection of

material and heat transfer conditions in order to keep the critical regimes at low temperature. It is quite obvious then, that the incidence of thermal stress failure in a plate subjected to radiation heating can be minimized by proper selection of material in combination with the optimum choice of the optical thickness and heat transfer conditions.

ACKNOWLEDGEMENTS

The present study was conducted as part of a larger research program on the thermo-mechanical and thermal behavior of high temperature structural materials supported by the Office of Naval Research under contract N00014-73-C-0431.

REFERENCES

1. W. D. Kingery, Factors Affecting Thermal Stress Resistance of Ceramic Materials, J. Amer. Ceram. Soc. 38:3 (1955).
2. D.P.H. Hasselman, Unified Theory of Thermal Shock Fracture Initiation and Crack Propagation in Brittle Ceramics, J. Amer. Ceram. Soc. 52:600 (1969).
3. D.P.H. Hasselman, Thermal Shock by Radiation Heating, J. Amer. Ceram. Soc. 46:229 (1963).
4. D.P.H. Hasselman, Theory of Thermal Shock Resistance of Semi-transparent Ceramics Under Radiation Heating, J. Amer. Ceram. Soc. 49:103 (1966).
5. D.P.H. Hasselman, J. R. Thomas, M. P. Kamat and K. Satyamurthy, Thermal Stress Analysis of Partially Absorbing Brittle Ceramics Subjected to Radiation Heating, J. Amer. Ceram. Soc. (in press).
6. J. R. Thomas, Jr., J. P. Singh and D.P.H. Hasselman, Analysis of Thermal Stress Resistance of Partially Absorbing Ceramic Plate Subjected to Assymmetric Radiation, I: Convective Cooling at Rear Surface, J. Amer. Ceram. Soc. (in review).
7. J. P. Singh, J. R. Thomas, Jr., and D.P.H. Hasselman, Thermal Stresses in Partially Absorbing Flat Plate Symmetrically Heated by Thermal Radiation and Cooled by Convection, J. Thermal Stress (in review).
8. R. Viskanta and E. E. Anderson, Heat Transfer in Semitransparent Solids, in: "Advances in Heat Transfer", F. Irvine, Jr., and James P. Hartnett, eds., Academic Press, NY, 11:317-441 (1975).
9. H. S. Carslaw and J. C. Jaeger, "Conduction of Heat in Solids", 2nd Ed., Oxford at Clarendon Press (1960).
10. B. A. Boley and J. H. Weiner, "Theory of Thermal Stresses", John Wiley and Sons, New York (1960).

REFERENCES (CONT'D)

11. K. Satyamurthy, D.P.H. Hasselman and J. P. Singh, Effect of Nature of Concavity of Temperature Distribution on Position and Sign of Maximum Thermal Stress, J. Appl. Mech. (in review).

CHAPTER XI

EFFECT OF SPATIAL VARIATION OF THERMAL CONDUCTIVITY ON MAGNITUDE OF TENSILE THERMAL STRESSES IN BRITTLE MATERIALS SUBJECTED TO CONVECTIVE HEATING

K. Satyamurthy, D. P. H. Hasselman, J. P. Singh and M. P. Kamat

Departments of Materials Engineering and Engineering
Science and Mechanics
Virginia Polytechnic Institute and State University
Blacksburg, Virginia 24061, USA

ABSTRACT

The results are presented for the effect of spatially varying thermal conductivity on the tensile thermal stress developed in a solid and a hollow circular cylinder subjected to different heating conditions. It is shown that the maximum tensile thermal stress in brittle ceramics can be reduced significantly by redistributing the temperature profile using (a) a spatial variation in thermal conductivity, (b) a spatial variation in pore content which in turn changes the density, thermal conductivity and modulus of elasticity and (c) by considering the effect of temperature on the thermal conductivity and specific heat. Possible methods for creating such variations in the material properties are discussed.

INTRODUCTION

The design of engineering structures or components operating under non-isothermal conditions must take into account the presence of thermal stresses which arise from, constrained non-uniform thermal expansion in addition to the normal operating stresses. For many structures or components operating at high-temperatures the transient thermal stresses during heat-up or cool-down can exceed the normal operating stresses by a considerable margin. Weakening of the structure (or complete failure) due to the thermal stresses should be avoided to assure long-term reliable operation. This is particularly critical for brittle ceramic materials in which because of the absence of non-linear stress-relieving mechanisms and low fracture toughness, thermal stress failure can be highly catastrophic with corresponding disastrous consequences for continued satisfac-

tory performance.

A number of options are available to the designer, working in conjunction with the materials technologist for reducing the probability of failure due to thermal stresses. First, for many heat transfer conditions, a redesign involving a change in the geometry or a reduction in the dimensions of the structure or component will reduce the magnitude of the thermal stresses. This approach, however, usually is incompatible with other performance criteria imposed on the structure or component. Secondly, the magnitude of the thermal stresses can be reduced by reducing the rate of heat transfer. Again, with few exceptions, this approach is impractical, as the rates of heat transfer are beyond the control of the designer. A third approach is to select the materials of construction of the structure or component on the basis of figures-of-merit for thermal stress resistance [1], which reflect the optimum combination of the relevant material properties such as the coefficient of thermal expansion, Young's modulus, thermal conductivity, etc. It should be noted, however, that thermal stress failure in even the optimum materials selected in this manner, is not necessarily avoided, as these figures-of-merit merely compare the relative thermal stress resistance of potential materials of construction. Furthermore, values of material properties which maximize thermal stress resistance may not be compatible with the property values required for optimum performance of the structure or component in its intended application.

A fourth approach to improving thermal stress resistance is based on the fact that the magnitude of the thermal stresses in a structure or component not only is a function of the magnitude of the temperature differences encountered within the structure or component, but also is a function of the temperature distribution. In principle, therefore, it should be possible to decrease the magnitude of thermal stress for a given heat transfer condition by modifications of the temperature distribution. Since the distribution of the temperature within a structure or component is a function of the thermal conductivity, modifications in those distributions can be achieved by incorporating a spatially varying thermal conductivity. A number of studies carried out by the present writers and co-workers [2,3,4,5] have shown that significant reductions in the magnitude of the tensile thermal stresses in brittle ceramic components can be achieved by decreasing the thermal conductivity in the hotter parts of the structure. These results were obtained for steady-state heat flow in a hollow-cylinder as well as in the transient heating of solid circular cylinders. The reductions in the tensile stresses were obtained not only by a direct spatial variation of the thermal conductivity but also indirectly by a spatial variation in density (which affects Young's modulus also), and by the negative temperature dependence of the thermal conductivity of dielectric materials in which the conduction of heat

occurs primarily by phonon transport. It is the purpose of this presentation to give an overview of these results.

CALCULATIONS, RESULTS AND DISCUSSION

A. Constant Heat Flow

Spatially Varying Thermal Conductivity. The geometry selected for the analysis of the effect of a spatially varying thermal conductivity under conditions of steady-state heat flow consisted of an infinitely long hollow concentric cylinder with inner and outer radius a and b , resp. The spatial variation of the thermal conductivity (K), for analytical convenience was selected as:

$$K = K_0 \{1 + f_0 (a/r)^n\}^{-1} \quad (1)$$

for radially outward heat flow and

$$K = K_0 \{1 + f_0 (r/b)^n\}^{-1} \quad (2)$$

for radially inward heat flow.

In eqs. 1 and 2, K_0 represents the spatially uniform thermal conductivity and f_0 and n are constants. The general form of eqs. 1 and 2 is such that the thermal conductivity is lowest in the regions of the cylinder which are at the highest temperature.

From eqs. 1 and 2 and the general condition for steady-state heat flow in a radial coordinate system [6], the temperature distribution within the cylinder was derived in terms of the temperature difference (ΔT) across the wall.

For brittle materials the maximum tensile stress is of primary interest. In a hollow cylinder undergoing steady-state heat flow, the radial and hoop stresses are exceeded by the longitudinal stress, which can be derived from [7]:

$$\sigma_z = \frac{\alpha E}{(1-\nu)} \left\{ \frac{2}{b^2 - a^2} \int_a^b r T dr - T(r) \right\} \quad (3)$$

where α is the coefficient of thermal expansion, E is Young's modulus, ν is Poisson's ratio and T is the temperature. For the purpose of this analysis, α , E and ν were assumed to be independent of position or temperature.

Figures 1 and 2 show the maximum value of the tensile longitudinal thermal stress at $r = b$ for radially outward heat flow and

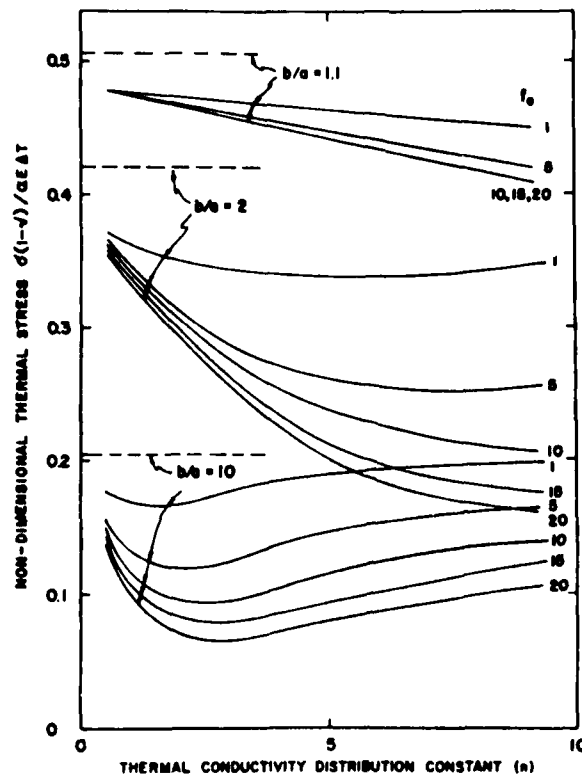


Fig. 1. Maximum tensile thermal stress in a hollow cylinder under steady-state outward radial heat flow and spatially varying thermal conductivity (equation 1). Dotted lines indicate values for uniform spatial distribution.

$r = a$ for the radially inward flow for three values of the ratio of outer to inner radius (b/a). Included in the figure are the values of stress for the spatially constant thermal conductivity. Comparison of these stress values shows that a spatially varying thermal conductivity can lead to a significant reduction in the magnitude of thermal stress. Since an order of magnitude variation in thermal conductivity of materials can be easily found, these results should be of practical significance.

Spatially Varying Density. The presence of a pore phase in solid materials has a pronounced effect on many material properties including the thermal conductivity. In principle, therefore a spatially varying thermal conductivity can be achieved by incorporating a spatially varying pore concentration in the material. A further advantage is achieved by the corresponding decrease in Young's modulus. Unfortunately, the tensile strength is also affected adversely by the pore phase which would lead to a decrease in the thermal stress resistance. However, this effect can be

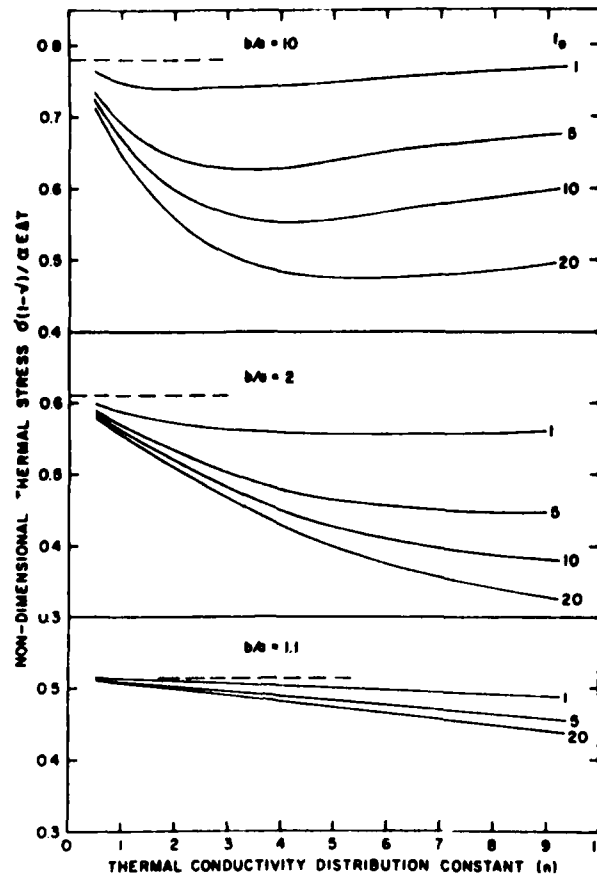


Fig. 2. Maximum tensile thermal stress in a hollow cylinder under steady-state inward radial heat flow and spatially varying thermal conductivity (equation 2). Dotted lines indicate values for uniform spatial distribution.

avoided by distributing the pore phase such that full density is maintained at the position of maximum tensile stress and having as high a porosity as practically possible in the region at higher temperature, which generally are in a state of compressive stress.

Accordingly, the porosity distribution for radially outward heat flow was arbitrarily taken as:

$$P = P_0 \{(b - r)/(b - a)\}^n \quad (4)$$

and for radially inward heat flow as:

$$P = P_0 \{(r - a)/(b - a)\}^n \quad (5)$$

where P_0 is the porosity at $r = a$ and $r = b$ for radially outward and inward heat flow, resp. and n the porosity distribution coefficient. Eqs. 4 and 5 indicate that $P = 0$ at the position of maximum tensile stress, i.e., $r = b$ and $r = a$ for the radially outward and inward heat flow, respectively.

The effect of the pore phase on the thermal conductivity, K and Young's modulus, E was chosen to be given by the well-known empirical equation [8,9]:

$$K, E = K_0, E_0 e^{-bp} \quad (6)$$

where K_0 and E_0 represent the values of the thermal conductivity and Young's modulus for the non-porous material, p is the fractional porosity and b is a constant taken as 3 and 4 for K and E , respectively. Poisson's ratio was assumed to remain unaffected by the pore phase. In view of the analytical complexity of the variation of E and K as expressed by eqs. 4, 5 and 6, the thermal stresses were obtained by a finite element computer program compiled for this purpose.

For radially inward heat flow, Fig. 3 shows the maximum value of longitudinal tensile stress as a function of the constant n in eqs. 4 and 5 for three values of the ratio of the outer to inner radius with $P_0 = 0.3$. Included in the figure is the value of stress corresponding to $P(r) = 0$. Similar results were obtained for radially outward heat flow. These results indicate that since the strength of the material remains unaffected in the critical regions, significant increase in thermal stress resistance is achieved. Additional calculations showed that the reduction in the magnitude of the maximum tensile stress to a good approximation was a linear function of the value of P_0 .

Of interest to note in Fig. 3 is that the value of stress is relatively independent of the value of n . This occurs because the maximum reduction in stress due to the individual effects of the spatially varying porosity on Young's modulus and thermal conductivity occur at different values of n . Minimizing the stresses by reducing Young's modulus requires a value of $n \rightarrow 0$. This implies a uniform pore phase, which results in a uniform thermal conductivity with no reduction in the thermal stresses. As far as a spatial variation in thermal conductivity is concerned, optimum reduction in the thermal stresses is achieved by values of $n \gg 1$ such that a reduction in thermal conductivity is achieved in the immediate regions of the tube surface at the higher temperature.

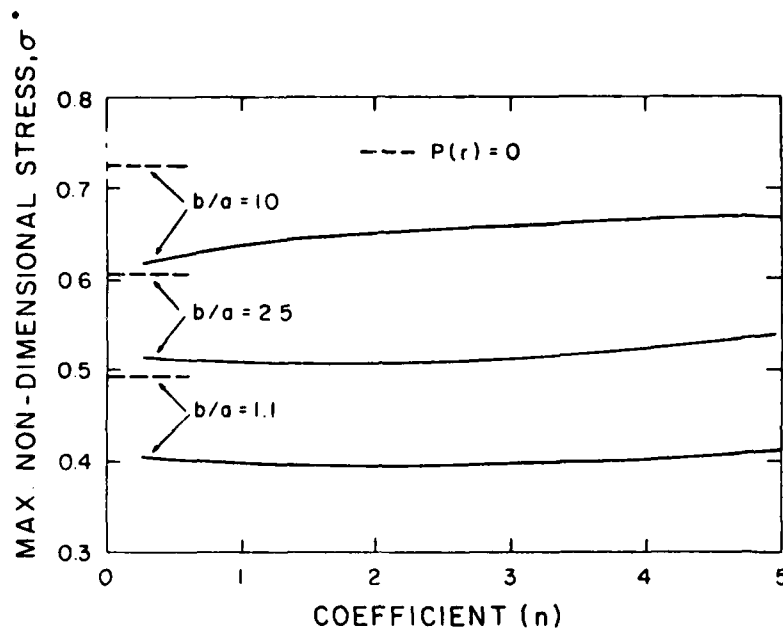


Fig. 3. Maximum tensile thermal stress as a function of the porosity distribution coefficient n in a hollow cylinder under steady-state radially inward heat flow with spatially varying pore content (equation 5) with $P_0(r = b) = 0.3$.

B. Transient Heating

An infinitely long solid circular cylinder of radius a was selected as an appropriate geometry for the analysis of the effect of a spatially varying thermal conductivity on the magnitude of thermal stress under conditions of transient heating. The specific heating conditions consisted of subjecting the cylinder initially at thermal equilibrium at a temperature T_0 , instantaneously to an ambient temperature of T_∞ . The transfer of heat was considered to be Newtonian according to:

$$K(a)(\partial T / \partial r(a)) + h(T(a) - T_\infty) = 0 \quad (7)$$

where h is the heat transfer coefficient and $T(a)$ is the instantaneous surface temperature.

Calculations of the thermal stresses were carried out with a finite element program which gave excellent agreement with stress values for spatially uniform thermal conductivity obtained analytically by Jaeger [10].

The maximum tensile stresses were of primary interest which for the present heating conditions are the hoop stresses at $r = 0$.

For convenience, the numerical results are reported in terms of the non-dimensional thermal stress, $\sigma^* = \sigma(1-\nu)/\alpha E \Delta T$, the non-dimensional time, $t^* = \kappa t/a^2$, the non-dimensional radial coordinate, r/a and the Biot number, $\beta_0 = ah/K_0$ in which $\Delta T = T_\infty - T_0$, κ is the thermal diffusivity and α is the coefficient of expansion. The Biot number is expressed in terms of the uniform thermal conductivity, prior to spatial modification.

Spatially Varying Thermal Conductivity. The radial dependence of the thermal conductivity was chosen to be of the form:

$$K(r) = K_0[1 - C(r/a)^n] \quad (8)$$

where n and $C(0 < C < 1)$ are constants. Equation 8 indicates that at $r = 0$, $K = K_0$ for any value of C and n . The lowest value of thermal conductivity occurs at $r = a$.

Fig. 4 shows typical results for the time dependence of the maximum tensile hoop stress at $r = 0$ for $\beta_0 = 5$ and a range of values of C and n . The peak values of the stress for a spatially varying thermal conductivity are considerably less than the corresponding values for the constant thermal conductivity, included in Fig. 4 for comparison.

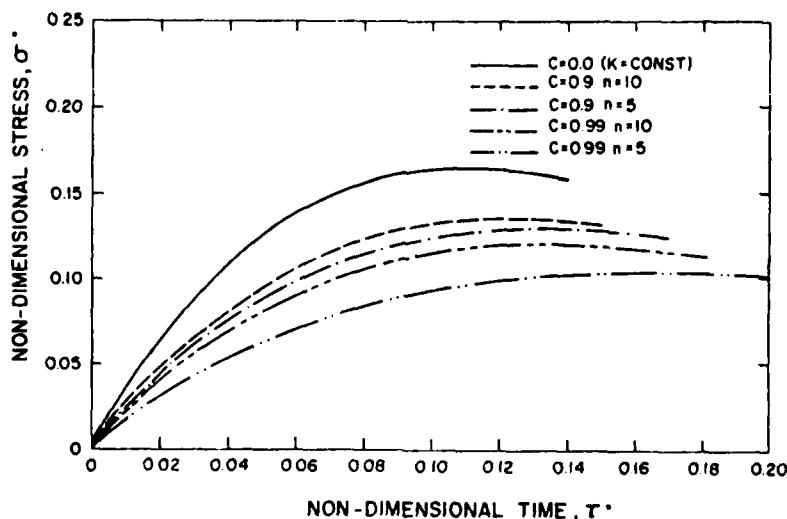


Fig. 4. Maximum tensile thermal stress as a function of time at the center of a solid circular cylinder subjected to sudden convective heating for various spatial distributions of the thermal conductivity (equation 8).

AD-A096 010

VIRGINIA POLYTECHNIC INST AND STATE UNIV BLACKSBURG --ETC F/G 11/2
THERMO-MECHANICAL AND THERMAL BEHAVIOR OF HIGH-TEMPERATURE STRU--ETC(U)
DEC 80 D P HASSELMAN N00014-78-C-0431

NL

UNCLASSIFIED

3 of 3
AD-A096 010



END
DATE
FILMED
4-81
DTIC

Figures 5a and 5b show the spatial variation of the temperatures and stresses, resp., at the time of maximum tensile stress for the same values of C and n as shown in Fig. 4. These results indicate that the decrease in tensile stress at $r = 0$ is accompanied by a corresponding increase in the temperatures and compressive stresses in the surface ($r = a$).

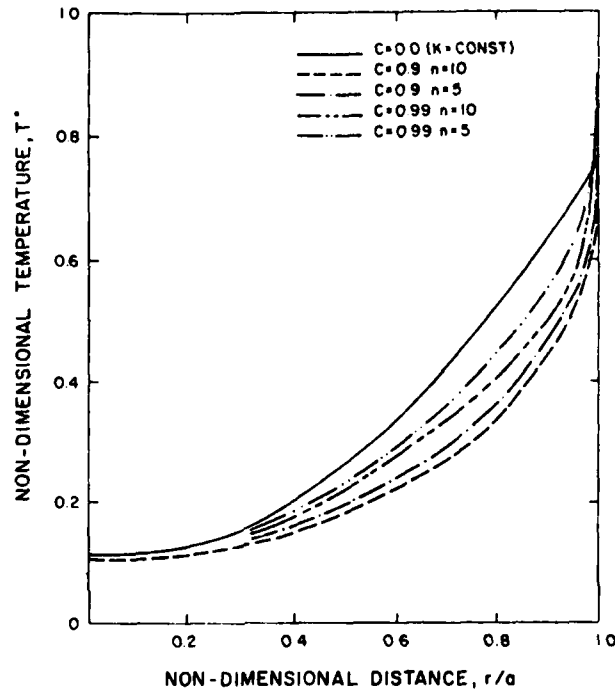


Fig. 5a. Spatial distribution of the transient temperature at the time of maximum tensile stress, in a solid circular cylinder subjected to sudden convective heating for various spatial distributions of the thermal conductivity (equation 8).

Figure 6 shows the maximum values of tensile hoop stress at $r = 0$ as a function of n for a range of values of C . Significant reductions in the magnitude of stress can be achieved, especially at the higher values of C .

Figure 7 compares the maximum values of tensile hoop stress for constant thermal conductivity and spatially varying thermal conductivity ($C = 0.9$, $n = 3$) as a function of Biot number. The reduction in stress for varying thermal conductivity is significant, especially at the higher values of the Biot number, at which materials are most susceptible to thermal stress failure.

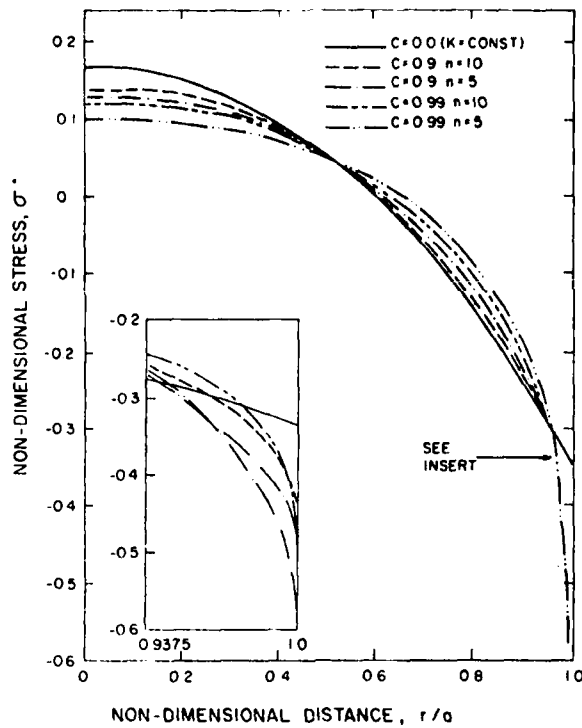


Fig. 5b. Spatial distribution of the transient thermal stress at the time of maximum tensile stress, in solid circular cylinder subjected to sudden convective heating for various spatial distributions of the thermal conductivity (equation 8).

Spatially Varying Porosity. The distribution of the pore phase was chosen to be:

$$P = P_0 (r/a)^n \quad (9)$$

The distribution for the thermal conductivity and Young's modulus was assumed to be identical to the one chosen for the steady-state heat flow given by eq. 6. Again, Poisson's ratio was assumed to be independent of the pore phase. The thermal stresses were calculated by the finite element program referred to earlier.

Figures 8a and 8b show the spatial variation in the transient temperatures and stresses for $\beta_0 = 1, 5$ and 20 , $n = 1$ and $P_0 = 0.3$ at the instant of time the tensile hoop stresses at the center of the cylinder reach their maximum value. A value of $P_0 = 0.3$ was chosen as it corresponds to a value realizable in practice. For purpose of comparison, the temperatures and stresses for the fully

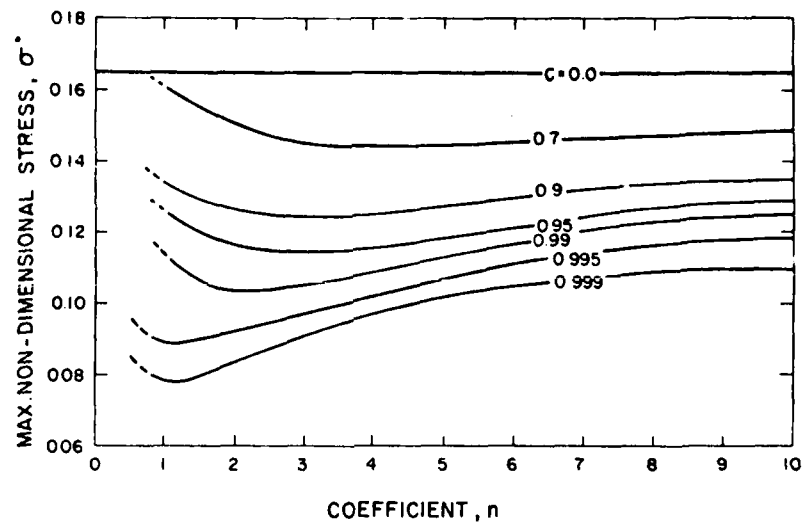


Fig. 6. Maximum tensile thermal stress as a function of coefficient, n in a solid circular cylinder subjected to convective heating for various spatial distributions of the thermal conductivity (equation 8).

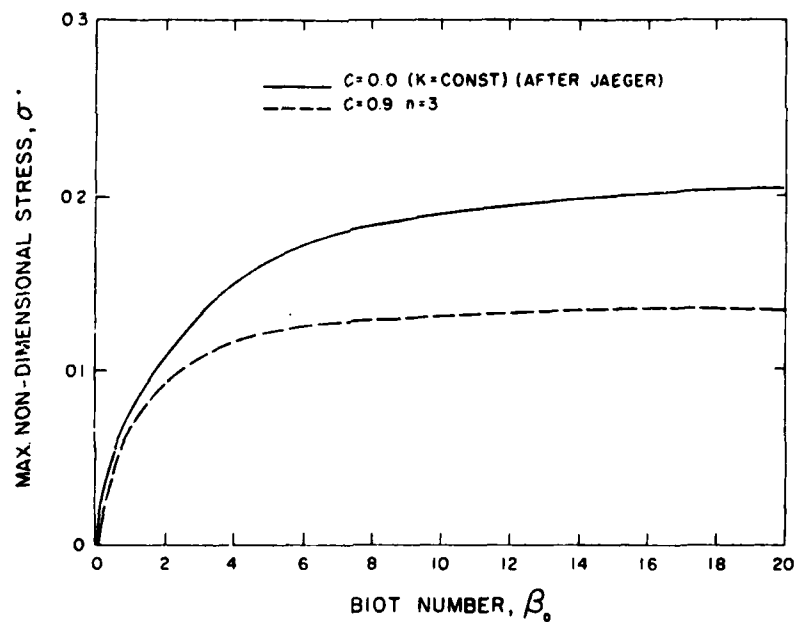


Fig. 7. Maximum tensile thermal stress as a function of Biot number in a solid circular cylinder with constant and spatially varying thermal conductivity ($n=3$, $C=0.9$) subjected to sudden convective heating.

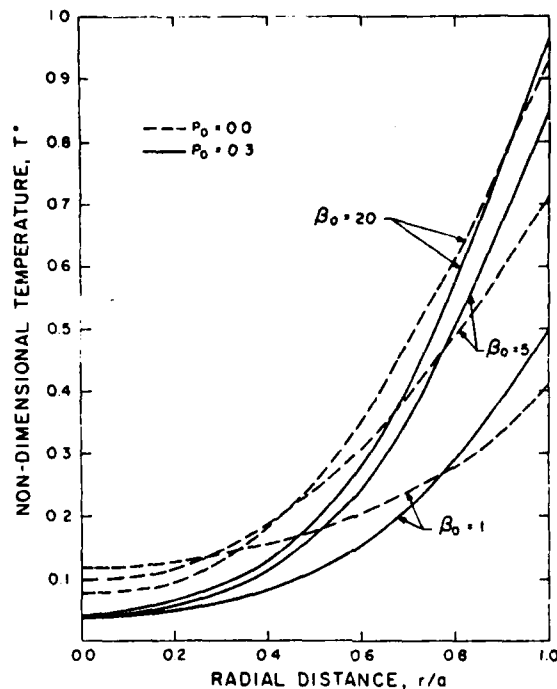


Fig. 8a. Spatial distribution of transient temperature at the time of maximum tensile stress in a solid circular cylinder subjected to sudden convective heating for spatially varying porosity described by equation 9 with $n=1$ and $P_0=0.3$.

dense material ($P_0=0$) are included in Figs. 8a and 8b. The numerical results indicate that the spatially varying pore phase results in a decrease in both the tensile and compressive thermal stresses in the cylinder, accompanied by a simultaneous increase in the surface temperature.

Figure 9 gives the maximum tensile hoop stress as a function of n for $\beta_0 = 1, 5$ and 20 . The stress levels for the fully dense material are included for comparison. A major reduction in the magnitude of the stresses as the result of the spatially varying pore phase is evident. Again, this reduction is greatest at the higher values of the Biot number, for which thermal stress fracture is most likely to occur. The trend of the curves in Fig. 9 suggests that it may be advantageous to have a porosity distribution corresponding to values of n as low as possible. It should be noted, however, that porosity also has a strong adverse effect on tensile strength. This implies that for low values of n , a considerable decrease in strength occurs very close to the center of the rod. In this case it is conceivable that failure can occur at position in the rod away from the center, so that the advantage of the spatial variation of the porosity can

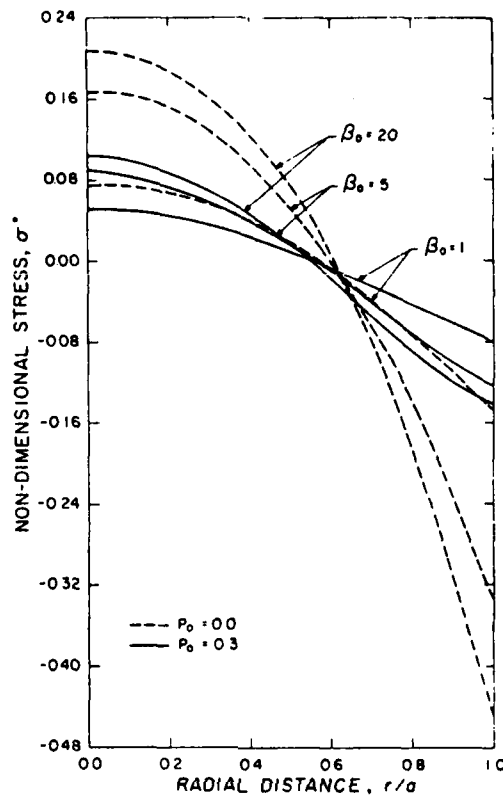


Fig. 8b. Spatial distribution of transient thermal stress at the time of maximum tensile stress in a solid circular cylinder subjected to sudden convective heating for spatially varying porosity described by equation 9 with $n=1$ and $P_0 = 0.3$.

be lost. Describing strength by eq. 6 with $b = 6$, values of n should be less than unity, if failure at positions other than $r = 0$ is to be avoided.

Temperature Dependent Thermal Conductivity and Specific Heat.

The discussion so far has concentrated on a spatial variation in thermal conductivity, either introduced directly or indirectly by incorporating a spatially varying pore phase.

A spatial variation of thermal conductivity can be caused by another mechanism, namely the temperature dependence of the thermal conductivity. It is well known, that for many dielectric materials in which the conduction of heat occurs primarily by phonon transport, the thermal conductivity exhibits a strongly negative temperature dependence. For this reason, during transient heating, the sections

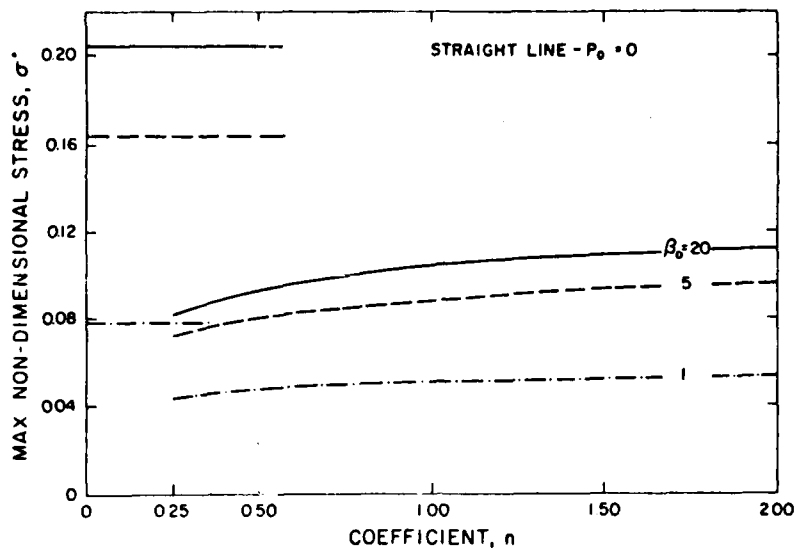


Fig. 9. Maximum tensile thermal stress as a function of n in a solid circular cylinder subjected to sudden convective heating for spatially varying porosity described by equation 9 with $P_0 = 0.3$ for various values of Biot number.

in a structure or component at the higher temperature will have a lower thermal conductivity than those regions still at a lower temperature. For a solid circular cylinder this should result in a type of a transient spatially varying thermal conductivity, with a distribution such that in analogy to the previous results, a major reduction in the magnitude of the tensile thermal stresses should be achieved.

The validity of this hypothesis was verified by calculating the maximum tensile thermal stresses in a solid circular cylinder of radius $a = 1$ cm of high density aluminum oxide at an initial uniform temperature of 300°K , subjected to convective thermal shock by an instantaneous change in ambient temperature to 1000°C . The transfer of heat was considered to be Newtonian. The temperature dependence of the thermal conductivity of dense aluminum oxide to a good approximation is described by [11]

$$K = 28/T - 0.01 \text{ cal.}^\circ\text{K}^{-1} \cdot \text{cm.}^{-1} \text{ sec}^{-1}.$$

where T is the absolute temperature in $^\circ\text{K}$. The temperature dependence of the specific heat was also taken into account [12]. All other material properties were assumed to be independent of temperature.

The thermal stresses were calculated with the finite element

program referred to earlier, with the required modifications to include the necessary iterative procedure to take the temperature dependence of the thermal conductivity and specific heat into account.

Figures 10a and 10b compare the time dependence of the thermal stresses for temperature dependent and independent thermal conductivity and specific heat, resp., for a range of values of the Biot number. The temperature dependence of the thermal conductivity and specific heat causes a significant decrease in the magnitude of the maximum tensile thermal stresses.

Figure 11 shows the peak value of the transient tensile thermal stress as a function of the Biot number. The relative reduction in the magnitude of these stresses is significant, especially at the higher values of the Biot number.

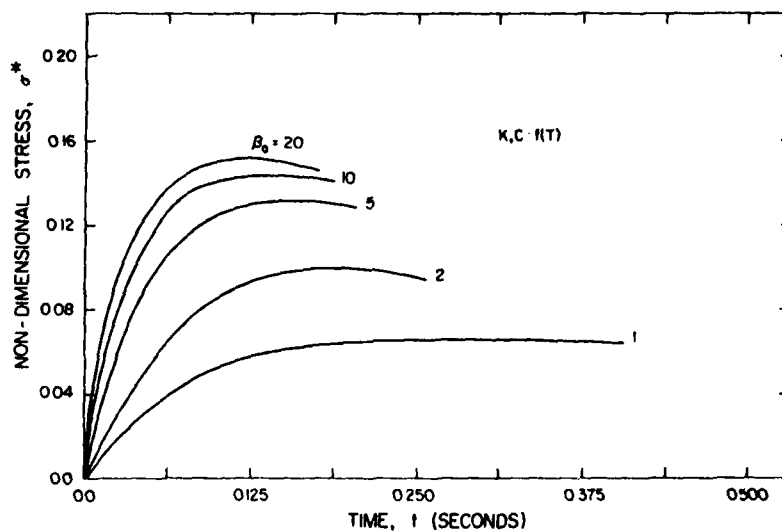


Fig. 11a. Maximum tensile thermal stress as a function of time at the center of solid circular cylinder subjected to sudden convective heating for a range of Biot numbers with temperature dependent thermal conductivity and specific heat.

C. Discussion

The results of the present study suggest that at least for the heat flow conditions considered, a spatially varying thermal conductivity can lead to significant reductions in the tensile thermal stresses. For all cases considered, this was achieved by decreasing the thermal conductivity in the sections of the geometries

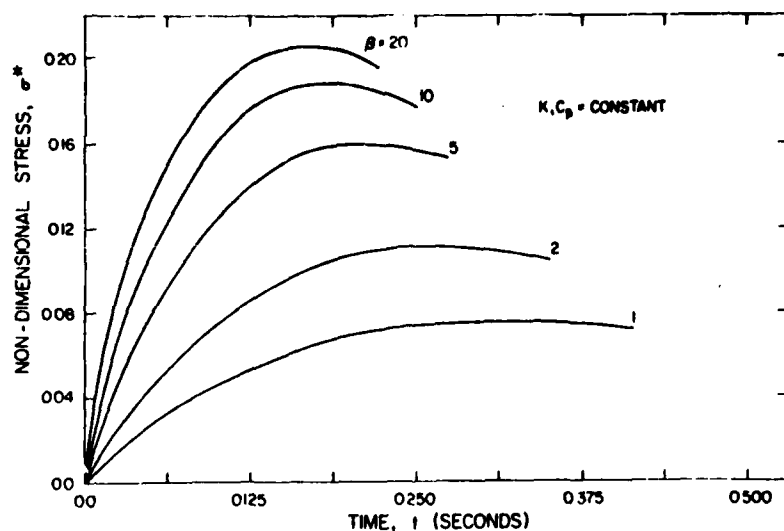


Fig. 10b. Maximum tensile thermal stress as a function of time at the center of solid circular cylinder subjected to sudden convective heating for a range of Biot numbers with constant thermal conductivity and specific heat.

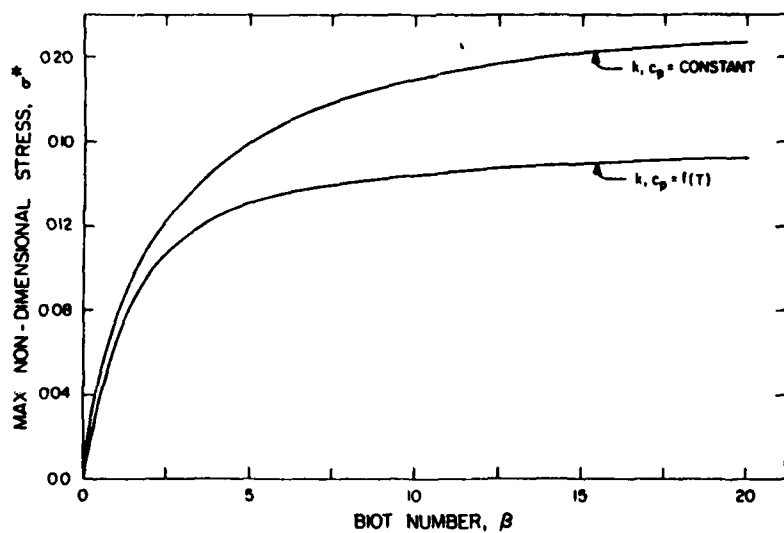


Fig. 11. Dependence of the maximum tensile thermal stress on Biot number in a solid circular cylinder with temperature dependent K , C_p and constant K , C_p subjected to sudden convective heating.

studied which are at the higher temperature. At first sight, this latter fact contradicts the results of thermal stress theory, based on spatially uniform properties, that thermal stresses can be decreased by increasing the thermal conductivity. The results of the present study substantiates the significant effect of the nature of the temperature distribution on the magnitude of thermal stress. For the steady-state heat flow reported in the earlier part of this paper, based on a constant ΔT across the cylinder wall, the magnitude of the stresses is governed only by the temperature distribution which is controlled by the relative distribution of the thermal conductivity and not by its absolute magnitude.

For the transient heat transfer, a decrease in thermal stress is achieved by the spatial variation in thermal conductivity, in spite of the fact that decreasing the thermal conductivity in the surface, in effect, raises the Biot number, which should result in an increase in thermal stress. Again, the strong influence of the temperature distribution on the magnitude of thermal stress is indicated. In this respect, it should be noted that comparing the numerical data for the thermal stresses in terms of the Biot number, Bo , based on the original unmodified value of thermal conductivity, K_0 , in fact, is conservative.

These general results of this study possibly can be of practical interest. Improvements in thermal stress resistance by a spatially varying pore phase already is common practice in the ceramic and refractory industry. Low thermal conductivity coatings can also be used, in which spatial variations in other properties should also be taken into account. Spatial variation in alloy content can be used very effectively to introduce a spatially varying thermal conductivity. Spatial variations in the degree of crystallinity for glass-ceramics can be used effectively for the same purpose, as well as other techniques appropriate for specific materials required for specific purposes.

ACKNOWLEDGMENT

This study was conducted as part of a research program on the thermo-mechanical and thermal properties of brittle structural materials supported by the Office of Naval Research under contract N00014-78-C-0431.

REFERENCES

1. D. P. H. Hasselman, Figures-of-Merit For the Thermal Stress Resistance of High-Temperature Brittle Materials: A Review, Ceramurgia, 4:147 (1978).

2. D. P. H. Hasselman and G. E. Youngblood, Enhanced Thermal Stress Resistance of Structural Ceramics with Thermal Conductivity Gradient, J. Amer. Ceram. Soc., 61:49 (1978).
3. K. Satyamurthy, M. P. Kamat and D. P. H. Hasselman, Effect of Spatially Varying Thermal Conductivity on Magnitude of Thermal Stress in Brittle Ceramics Subjected to Convective Heating, J. Amer. Ceram. Soc., (in review)
4. K. Satyamurthy, J. P. Singh, M. P. Kamat and D. P. H. Hasselman, Effect of Spatially Varying Porosity on Magnitude of Thermal Stress During Steady-State Heat Flow, J. Amer. Ceram. Soc., 62:431 (1979).
5. K. Satyamurthy, J. P. Singh, M. P. Kamat and D. P. H. Hasselman, Thermal Stress Analysis of Brittle Ceramics With Density Gradients under Conditions of Transient Convective Heat Transfer, Trans. Brit. Ceram. Soc., (in review).
6. H. S. Carslaw and J. C. Jaeger, "Conduction of Heat in Solids," 2nd Ed., Oxford University Press, London (1959).
7. B. A. Boley and J. H. Weiner, "Theory of Thermal Stresses," J. Wiley, New York (1960).
8. R. M. Spriggs, Expression of Effect of Porosity on Elastic Modulus of Polycrystalline Refractory Materials, Particularly Aluminum Oxide, J. Amer. Ceram. Soc., 44:628 (1961).
9. F. P. Knudsen, Dependence of Mechanical Strength of Brittle Polycrystalline Specimens on Porosity and Grain Size, J. Amer. Ceram. Soc., 42:376 (1959).
10. J. C. Jaeger, On Thermal Stresses in Circular Cylinders, Phil. Mag. 36:418 (1945).
11. Y. S. Touloukian, R. W. Powell, C. Y. Ho and P. G. Klemens, Thermal Conductivity: Non-Metallic Solids (Thermophysical Properties of Matter, Vol. 2, p. 119, IFI) Plenum, New York (1970).
12. Y. S. Touloukian and E. H. Buyco, Specific Heat: Non-Metallic Solids (Thermophysical Properties of Matter, Vol. 5, pp. 27-29, IFI) Plenum, New York (1970).

December 1980

BASIC DISTRIBUTION LIST

Technical and Summary Reports

<u>Organization</u>	<u>No. of Copies</u>	<u>Organization</u>	<u>No. of Copies</u>
Defense Documentation Center Cameron Station Alexandria, Virginia 22314	(12)	Naval Construction Battalion Civil Engineering Laboratory Port Hueneme, California 93043 Attn: Materials Division	(1)
Office of Naval Research Department of the Navy Attn: Code 471 Code 102 Code 470	(1) (1) (1)	Naval Electronics Laboratory Center San Diego, California 92152 Attn: Electron Materials Science Division	(1)
Commanding Officer Office of Naval Research Branch Office 495 Summer Street Boston, Massachusetts 02210	(1)	Naval Missile Center Materials Consultant Code 3312-1 Point Mugu, California 93041	(1)
Commanding Officer Office of Naval Research Branch Office 536 South Clark Street Chicago, Illinois 60605	(1)	Commanding Officer Naval Surface Weapons Center White Oak Laboratory Silver Spring, Maryland 20910 Attn: Library	(1)
Office of Naval Research San Francisco Area Office One Hallidie Plaza, Suite 601 San Francisco, California 94102	(1)	David W. Taylor Naval Ship R&D Center Materials Department Annapolis, Maryland 21402	(1)
Naval Research Laboratory Washington, D.C. 20390 Attn: Code 6000 Code 6100 Code 6300 Code 6400 Code 2627	(1) (1) (1) (1) (1)	Naval Undersea Center San Diego, California 92132 Attn: Library	(1)
Naval Air Development Center Code 302 Warminster, Pennsylvania 18974 Attn: Mr. F. S. Williams	(1)	Naval Underwater System Center Newport, Rhode Island 02840 Attn: Library	(1)
Naval Air Propulsion Test Center Trenton, New Jersey 08628 Attn: Library	(1)	Naval Weapons Center China Lake, California 93555 Attn: Library	(1)
		Naval Postgraduate School Monterey, California 93940 Attn: Mechanical Engineering Dept.	(1)
		Naval Air Systems Command Washington, D.C. 20360 Attn: Code 52031 Code 52032	(1) (1)

BASIC DISTRIBUTION LIST (Cont'd)

<u>Organization</u>	<u>No. of Copies</u>	<u>Organization</u>	<u>No. of Copies</u>
Naval Sea System Command Washington, D. C. 20362 Attn: Code 035	(1)	NASA Headquarters Washington, D. C. 20546 Attn: Code RRM	(1)
Naval Facilities Engineering Command Alexandria, Virginia 22331	(1)	NASA Lewis Research Center 21000 Brookpark Road Cleveland, Ohio 44135 Attn: Library	(1)
Scientific Advisor Commandant of the Marine Corps Washington, D.C. 20380 Attn: Code AX	(1)	National Bureau of Standards Washington, D.C. 20234 Attn: Metallurgy Division Inorganic Materials Division	(1) (1)
Naval Ship Engineering Center Department of the Navy Washington, D.C. 20360 Attn: Code 6101	(1)	Defense Metals and Ceramics Information Center Battelle Memorial Institute 505 King Avenue Columbus, Ohio 43201	(1)
Army Research Office P.O. Box 12211 Triangle Park, N.C. 27709 Attn: Metallurgy & Ceramics Program	(1)	Office of Naval Research, Branch Office 1030 East Green Street Pasadena, CA. 91106	(1)
Army Materials and Mechanics Research Center Watertown, Massachusetts 02172 Attn: Research Programs Office	(1)	Metals and Ceramics Division Oak Ridge National Laboratory P.O. Box X Oak Ridge, Tennessee 37380	(1)
Air Force Office of Scientific Research Bldg. 410 Bolling Air Force Base Washington, D.C. 20332 Attn: Chemical Science Director rate Electronics and Solid State Science Director- rate	(1) (1)	Los Alamos Scientific Laboratory P.O. Box 1663 Los Alamos, New Mexico 87544 Attn. Report Librarian Argonne National Laboratory Metallurgy Division P.O. Box 229 Lemont, Illinois 60439	(1) (1)
Air Force Materials Lab (LA) Wright-Patterson AFB Dayton, Ohio 45433	(1)	Brookhaven National Laboratory Technical Information Division Upton, Long Island New York 11973 Attn: Research Library	(1)
Library, Bldg 50, Rm 134 Lawrence Radiation Laboratory Berkeley, CA 94720	(1)		

BASIC DISTRIBUTION LIST (Cont'd)

<u>Organization</u>	<u>No. of Copies</u>	<u>Organization</u>	<u>No. of Copies</u>
Director Applied Physics Laboratory (1) University of Washington 1013 Northeast Fortieth Street Seattle, Washington 98105			

SUPPLEMENTARY DISTRIBUTION LIST

Technical and Summary Reports

Advanced Research Project Agency
Materials Science Director
1400 Wilson Boulevard
Arlington, VA 22209

Mr. George Boyer
Sensor Systems Program
Office of Naval Research
Code 222
Arlington, VA 22217

Professor R. Bradt
Ceramics Section
Materials Sciences Department
The Pennsylvania State University
University Park, PA 16802

Professor L. E. Cross
The Pennsylvania State University
Materials Research Laboratory
University Park, PA 16802

Dr. A. G. Evans
Department Materials Science
and Engineering
Hearst Mining Building
University of California
Berkeley, CA 94720

Dr. Gene Haertling
Motorola Corporation
3434 Vassar, NE
Albuquerque, NM 87107

Dr. L. L. Hench
Department of Metallurgy
University of Florida
Gainesville, FL 32603

Dr. A. A. Heuer
Professor of Ceramics
Case Western Reserve University
University Circle
Cleveland, OH 44106

Dr. Paul Jorgensen
Stanford Research Institute
333 Ravenswood Avenue
Menlo Park, CA 94025

Dr. R. N. Katz
Army Materials and Mechanics
Research Center
Watertown, MA 02172

Dr. H. Kirchner
Ceramic Finishing Company
P.O. Box 498
State College, PA 16801

Dr. B. G. Koepke
Honeywell, Inc.
Corporate Research Center
10701 Lyndale Avenue South
Bloomington, MN 55420

Mr. Frank Koubek
Naval Surface Weapons Center
White Oak Laboratory
Silver Spring, MD 20910

Dr. J. Lankford
Southwest Research Institute
8500 Culebra Road
San Antonio, TX 78284

Professor P. B. Macedo
The Catholic University of America
Washington, DC 20017

Dr. N. Perrone
Code 474
Office of Naval Research
800 N. Quincy Street
Arlington, VA 22217

Dr. R. Rice
Naval Research Laboratory
Code 6360
Washington, DC 20375

SUPPLEMENTARY DISTRIBUTION LIST (Cont'd)

Dr. A. M. Alper
GTE Sylvania Inc.
Towanda, PA 18848

Dr. W. H. Rhodes
GTE Laboratories Inc.
40 Sylvan Rd.
Waltham, MA 02154

Dr. D. C. Larson
IIT Research Inst.
10 W. 35th Street
Chicago, IL 60616

Dr. B. Butler, Chief
Materials Branch
Solar Energy Research Institute
1536 Cole Blvd
Golden, CO 80401

Dr. M. Berg
AC Spark Plug Division
General Motors Corp.
1601 N. Averill Avenue
Flint, MI 48556

Dr. I. K. Naik
Airesearch Casting Corp.
Garrett Corp.
2525 W. 190th Street
Torrance, CA 90509

Dr. R. J. Bratton
R&D Center
Westinghouse Electric Corp.
Pittsburgh, PA 15235

Dr. W. Reilly, Director
PPG Industries
P.O. Box 31
Barberton, OH 44203

Dr. D. J. Godfrey
Admiralty Materials Laboratory
Ministry of Defense
(Procurement Executive)
Holton Heath
Poole, Dorset
BH16 6 JU
UNITED KINGDOM

Dr. Wm. Kessler
AFML
Wright-Patterson Air Force Base
OH 45433

Dr. S. F. Galasso
United Aircraft Research Laboratories
East Hartford, CN 06108

Dr. J. A. Coppola
The Carborundum Comp.
P.O. Box 1054
Niagara Falls, NY 14302

Dr. W. D. Tuohig
Bendix Research Laboratories
Southfield, MI 48076

Dr. Robert Ruh
AFML/LLM
Wright-Patterson AFB
OH 45433

Dr. R. A. Penty
Hague International
3 Adams Street
South Portland, Maine 04106

Dr. S. Musikant
General Electric Company
3198 Chestnut Street
Philadelphia, PA 19101

Dr. D. W. Richerson
Airesearch Man. Comp. Code 503-44
Garrett Corp.
111 S. 34th Str., Box 5217
Phoenix, AZ 85034

Dr. Frank Recny
General Electric Company
Court Street
Plant Building C
Box 1122
Syracuse, NY 13201

Globe-Union, Inc.
5757 North Green Bay Avenue
Milwaukee, WI 53201
Attn: G. Goodman

SUPPLEMENTARY DISTRIBUTION LIST (Cont'd)

Dr. J. H. Rosolowski
General Electric Company
Research and Development Center
P.O. Box 8
Schenectady, NY 02301

Dr. J. H. Simmons
Catholic University of America
Washington, DC 20064

Dr. P. L. Smith
Naval Research Laboratory
Code 6361
Washington, DC 20375

Dr. R. W. Timme
Naval Research Laboratory
Code 8275
Underwater Sound Reference Division
P.O. Box 8337
Orlando, FL 32806

Dr. Charles C. Walker
Naval Sea Systems Command
National Center #3
2531 Jefferson Davis Highway
Arlington, VA 20390

Dr. Paul D. Wilcox
Sandia Laboratories
Division 2521
Albuquerque, NM 87115

Dr. Murray Gillen
Australian Embassy
Washington, DC 33801

Dr. C. O. Hulse
United Aircraft Research Labs
United Aircraft Corporation
East Hartford, CT 06108

Dr. S. M. Wiederhorn
Physical Properties Section
Bldg. 223, Rm. A355
National Bureau of Standards
Washington, DC 20234

Dr. P. F. Becher
Metals and Ceramics Division
Oak Ridge National Laboratory
Oak Ridge, TN 37830

Dr. R. Jaffee
Electric Power Research Institute
3412 Hillview Avenue
P.O. Box 10412
Palo Alto, CA 94303

Dr. B. A. Wilcox
Ceramics Programs, Room 336
Metallurgy and Materials Research
National Science Foundation
Washington, DC 20550

Dr. H. E. Bennett
Naval Surface Weapons Center
Research Department Code 601
China Lake, CA 93555

Dr. R. J. Charles
General Electric Company
Research and Development Center
Schenectady, NY 12301

Dr. A. R. C. Westwood
Martin-Marietta Laboratories
1450 South Rolling Road
Baltimore, MD 21227

Dr. N. S. Corney
Ministry of Defense
(Procurement Executive)
The Adelphi
John Adam Street
London WC2N 6BB
UNITED KINGDOM

Dr. D. E. Niesz
Battelle Memorial Institute
505 King Avenue
Columbus, OH 43201

Dr. R. E. Engdahl
Deposits and Composites, Inc.
318 Victory Dr.
Herndon, VA 22070

Professor W. D. Kingery
Ceramics Div. Rm. 13-4090
MIT
77 Mass. Avenue
Cambridge, MA 02139

SUPPLEMENTARY DISTRIBUTION LIST (Cont'd)

Mr. J. F. McDowell
Sullivan Park
Corning Glass Works
Corning, NY 14830

Dr. E. K. Beauchamp, Div. 5846
Sandia Laboratories
Albuquerque, NM 87185

Dr. J. A. Rubin
Kyocera International, Inc.
8611 Balboa Avenue
San Diego, CA 92123

Dr. W. V. Kotlensky
Materials Technology Department
TRW, Inc.
One Space Park
Redondo Beach, CA 90278

Dr. N. N. Ault
NORTON Comp.
One New Bond Street
Worcester, MA 01606

Dr. Hayne Palmour III
Engineering Research Division
N.C. State University
P.O. Box 5995
Raleigh, NC 27650

Dr. D. Ulrich
AFOSR, Code NC
Chemical Sciences Div.
1400 Wilson Blvd.
Arlington, VA 22209

Dr. V. J. Tennery
Oak Ridge Nat. Lab.
Oak Ridge, TN 38730

Dr. E. D. Lynch
Lynchburg Research Center
Babcock and Wilcox Co.
Box 1260
Lynchburg, VA 24505

Dr. S. C. Dixon
SDD-Thermal Structure Branch
Mail Stop 395
NASA Langley Research Center
Hampton, VA 23665

Dr. F. W. Clinard, Jr.
Los Alamos Scientific Lab.
MS 546
P.O. Box 1663
Los Alamos, NM 87544

Dr. D. DeCoursin
Fluidyne Eng.
5900 Olson Memorial Hwy.
Minneapolis, MN 55422

Dr. F. F. Lange
Rockwell International
P.O. Box 1085
1049 Camino Dos Rios
Thousand Oaks, CA 91360

Dr. T. Vasilos
AVCO Corporation
Research and Advanced Development
Division
201 Lowell Str.
Wilmington, MA 01887

Dr. W. R. Prindle
National Materials Adv. Brd.
2101 Const. Avenue
Washington, DC 20418

Dr. S. Dutta
NASA-Lewis Research Center
Mail Stop 49-3
21000 Brookpark Rd.
Cleveland, OH 44135

Mr. B. Probst
NASA-Lewis Research Center
21000 Brookpark Rd.
Cleveland, OH 44135

Dr. S. W. Freiman
Deformation and Fracture Group
Physical Properties Section, Bldg 223
National Bureau of Standards
Washington, DC 20234

Mr. W. Trombley
Garrett Corporation
1625 Eye Str. NY
Suite 515
Washington, DC 20006

SUPPLEMENTARY DISTRIBUTION LIST (Cont'd)

Mr. R. T. Swann
MD-Materials Research Branch
Mail Stop 396
NASA Langley Research Center
Hampton, VA 23665

Dr. K. H. Holko, Manager
Materials Applications
General Atomic Company
P.O. Box 81608
San Diego, CA 92138

Dr. W. Bakker
EPRI
3412 Hillview Avenue
P.O. Box 10412
Palo Alto, CA 94303

Dr. P. A. Miles, Research
Raytheon Company
28 Seyon Str.
Waltham, MA 02154

Dr. J. Ritter
University of Massachusetts
Dept. of Mech. Engr.
Amherst, MA 01002

Dr. M. E. Gulden
International Harvester Company
Solar Division
2200 Pacific Highway
San Diego, CA 92138

Dr. G. E. Youngblood
MERDI
Butte, MT 59701

Mr. C. E. Bersch
Code 52032
Naval Air Systems Command
Washington, DC 20361

Dr. M. A. Adams
Jet Propulsion Laboratory
California Institute of Technology
4800 Oak Grove Drive
Pasadena, CA 91103

Dr. Clifford Astill
Solid Mechanics Program
National Science Foundation
Washington, DC 20550

Dr. R. J. Gottschall
U.S. Dept. of Energy
Div. of Materials Science
Mail Stop J309
Washington, DC 20545

Prof. R. Roy
Pennsylvania State Univ.
Materials Research Lab.
University Park, PA 16802

Dr. R. Ruh
AFML - WPAFB
Dayton, OH 45433

Mr. J. Schuldies
Airesearch
Phoenix, AZ

Mr. J. D. Walton
Engineering Exp. Station
Georgia Inst. of Technology
Atlanta, GA 30332

Dr. W. F. Adler
Effects Technology, Inc.
5383 Hollister Avenue
P.O. Box 30400
Santa Barbara, CA 92105

Mr. D. Richarson
Airesearch Manufacturing Company
4023 36th Street
P.O. Box 5217
Phoenix, AZ 85010

Dr. N. MacMillan
Materials Research Laboratory
Pennsylvania State University
College Park, PA 16802

Mr. W. B. Harrison
Honeywell Ceramics Center
1885 Douglas Drive
Golden Valley, MN 55422

SUPPLEMENTARY DISTRIBUTION LIST (Cont'd)

Dr. Donald M. Curry, ES32
Thermal Technology Br.
National Aeronautics and
Space Administration
Lyndon B. Johnson Space Center
Houston, Texas 77058

Dr. R. E. Rondeau
AFML-LDJ
Wright Patterson-Air Force Base
OH 45433

Dr. E. G. Kobetich
Experimental Station, Bldg. 302
E. I. DuPont Company
Wilmington, DE 19898

Dr. Fred Schmidt
E. I. DuPont
Engineering Dept, E-304
Experimental Station
Wilmington, DE 19898

